Increasing the efficiency of organic solar cells by photonic and electrostatic-field enhancements

by

Kanwar Singh Nalwa

A dissertation submitted to the graduate faculty

in partial fulfillment of the requirements for the degree of

DOCTOR OF PHILOSOPHY

Major: Electrical Engineering

Program of Study Committee:
Sumit Chaudhary, Major Professor
Vikram Dalal
Joseph Shinar
Mani Mina
Kristen Constant

Iowa State University

Ames, Iowa

2011

TABLE OF CONTENTS

LIST OF FIGURES

LIST OF TABLES

ACKNOWLEDGEMENTS

I would like to express my sincere gratitude to my major professor, Dr. Sumit Chaudhary, for his invaluable guidance and support throughout this research. I am his first student and that enabled the direct transfer of knowledge/skills from him to me. I still remember the first discussion that we had on Solar cells, and he flooded my brain with so many ideas and it ignited in me the fire to indulge myself in research. I was nurtured, guided and molded to do well in research and all the credit goes to him. He taught me how to deal with failures, learn from them and strive towards greater goals, imbibing in me the key to achieve success as a graduate researcher. He always encouraged me and supported my ideas, corrected me if I was wrong, motivated me when I failed, and helped me when I needed the most. He always managed to take out time for me, for discussions or even to sort out my personal issues,for which I will be always grateful. There are numerous things apart from research, which I had the pleasure of learning from him, and those things matured me as a person. Initially I was unsatisfied and discontent with the limited resources at hand, but he taught me to utilize the available resources efficiently to achieve goals and wiped out completely any feeling of regret that I had.

I am also honored to have Dr. Vikram Dalal on my program of study committee. I cannot thank Dr. Dalal enough for being a continuous source of inspiration for me and helping me build a strong foundation of semiconductor physics. I did not have any background of solid state physics to begin with, but his lectures opened my mind to this extraordinary field. It was a sheer pleasure and wonderful opportunity to learn the concepts of photovoltaic devices from one of the pioneers of this field and it will go a long way in helping me throughout my career. I am also grateful to Dr. Dalal for trusting me with the

equipments belonging to his group and making them available to me whenever I needed, thus enabling me to pursue my research smoothly.

Special gratitude goes to Dr. Joseph Shinar, Dr. Kristen Constant and Dr. Mani Mina for serving on my dissertation committee and more than that, for great discussions, support and advice during the course of my PhD. I would also like to thank Dr. Jayeoun Kim and Dr. Kai-Ming Ho for their helpful discussions and advices during the course of my research.I am also grateful to Max Noack for all his technical help and healthy discussions.

I am thankful to my labmates: Rakesh Mahadevapuram, John Carr, Yuqing Chen, Dan Putnam and Aaron Theoming, for helping me survive the gruesome period of research and decorating the black and white life of Microelectronics Research Center with their rich colors.

I would like to thank Dr. Baskar Ganapathysubramanian, Dr. Joong-Mok Park, Ping Kuang, Yuankun Cai, Hari K. Kodali, Sayantan Bose, Jared F. Mike, Kyle Miller and Wai Leung for making all the collaborative projects a success. I also appreciate their patience and understanding with me during the tenure.

PhD life takes a toll on you, but that was not the case with me, since I was surrounded by great friends (Neerav, Nayan, Ashutosh, Elle, Siva, Navneet, Gaurav Mohanty, Amit, Aditya, Prateek, Santosh, Dinesh and the list goes on and on) and roommates (Gaurav, Navjot, Devender), who made my stay at ISU enjoyable and made my apartment a home away from home.

The key element without which all of this would not have been possible, is the support of my family. My mother and father trusted me with my decisions and always encouraged me in my endeavors. I feel blessed to have a loving and understanding wife

who always stood by me in my trails. This all has been made possible because of the numerous sacrifices she made for me. I think the saying is appropriate in my case “Behind every successful man there is a woman”. Whatever success I have, I owe it to her and my family. I can only hope that I will be able to give back even an infinitesimal fraction of what my family has done for me.

ABSTRACT

Organic photovoltaic (OPV) technology is an attractive solar-electric conversion paradigm due to the promise of low cost roll-to-roll production and amenability to flexible substrates. Power conversion efficiency (PCE) exceeding 7% has recently been achieved. OPV cells suffer from low charge carrier mobilities of polymers, leading to recombination losses, higher series resistances and lower fill-factors. Thus, it is imperative to develop fabrication methodologies that can enable efficient optical absorption in films thinner than optical absorption length. Active layers conformally deposited on light-trapping, microscale textured, grating-type surfaces is one possible approach to achieve this objective. In this study, 40% theoretical increase in photonic absorption over flat OPVs is shown for devices with textured geometry by the simulation results. For verifying this theoretical result and improving the efficiency of OPVs by light trapping, OPVs were fabricated on grating-type textured substrates possessing the theoretically claimed best optical design (2 μm pitch and 1.5 μm height). Attempts to spin-coat PV active-layer on these textured substrates led to over filling of the valleys and shunts at the crest, which severely affected the performance of the resultant PV devices. Thus, it is established that although the optical design is important for OPV performance but the potential of light trapping can only be effectively tapped if the textures are amenable for realizing a conformal active layer. It is discovered that if the height of the underlying topographical features is reduced to sub-micron regime (e.g. 300 nm) and the pitch is increased to more than a micron (e.g. 2 μm), the textured surface becomes amenable to coating a conformal PV active-layer. The resultant PV cells showed 100% increase in average light absorption near the band edge due to trapping of

higher wavelength photons, and 20% improvement in power conversion efficiency as compared with the flat PV cell.

Another factor that severely limits the performance of OPVs is recombination of charge carriers. Thus it becomes imperative to understand the effect of processing conditions such as spin coating speed and drying rate on defect density and hence induced carrier recombination mechanism. In this study, It is shown that slow growth (longer drying time) of the active-layer leads to reduction of sub-bandgap traps by an order of magnitude as compared to fast grown active-layer. By coupling the experimental results with simulations, it is demonstrated that at one sun condition, slow grown device has bimolecular recombination as the major loss mechanism while in the fast grown device with high trap density, the trap assisted recombination dominates.

It has been estimated that non-radiative recombination accounts nearly 50% of efficiency loss in modern OPVs. Generally, an external bias (electric field) is required to collect all the photogenerated charges and thus prevent their recombination. The motivation is to induce additional electric field in otherwise low mobility conjugated polymer based active layer by incorporating ferroelectric dipoles. This is expected to facilitate singlet exciton dissociation in polymer matrix and impede charge transfer exciton (CTE) recombination at polymer:fullerene interface. For the first time, it is shown that the addition of ferroelectric dipoles to modern bulk heterojunction (BHJ) can significantly improve exciton dissociation, resulting in a ~50% enhancement of overall solar cell efficiency. The devices also exhibit the unique ferroelectric-photovoltaic effect with polarization-controlled power conversion efficiency.

CHAPTER 1. Introduction

1.1 Background

Organic photovoltaics (OPVs) have gained much attention in the past decade because they offer realization of low-cost solar energy conversion devices, with advantages including mechanical flexibility, light weight, ease of processing and large area roll-to-roll production. The field has made impressive progress in the last five years. Most of the developments that have improved performance of OPVs are based on electron donor-acceptor heterojunctions, which deal with the photoinduced electron transfer from a donor conjugated polymer to an acceptor molecule [1]. A revolutionary development in organic photovoltaics came in the mid-1990s with the introduction of a dispersed/bulk heterojunction (BHJ), where an electron accepting and an electron donating material are blended together at the length scale similar to the exciton diffusion length [2-4]. The dissociation of excitons at the donor-acceptor interface leads to free electrons and holes which travel to the contacts, if continuous pathways exist in each material from the interface to the respective electrodes. The electron acceptors are often the fullerenes or the derivative [6,6]-phenyl-C61-butyric acid methyl ester (PCBM) having better miscibility in organic solvents. For OPVs with poly(3-hexylthiophene) as electron donor, highest efficiencies reaching up to 5% have been reported [5-7]; however further improvement in efficiency is required for large scale commercialization and practical applications.

The candidates for photovoltaic applications which come under the division of organic electronic materials include small molecules (molecules of molecular weight of a few 100) processed by vacuum deposition, polymers (long chain with repeating monomer

units) processed from solution and their combination with any other organic solids or inorganic materials.

The primary differences between inorganic and organic photovoltaic materials are following:

- Photogenerated excitations (‘excitons’) are strongly bound and do not spontaneously dissociate into separate charges. Dissociation requires an input of energy of ~100 meV compared to a few meV for a crystalline semiconductor. This means that carrier generation does not necessarily result from the absorption of light.
- Charge transport proceeds by hopping between localized states, rather than transport within a band, which results in low mobilities.
- The spectral range of optical absorption is relatively narrow compared to the solar spectrum.
- Absorption coefficients are high ($\sim 10^7 cm^{-1}$) so that high optical densities can be achieved, at peak wavelength, with films less than 100 nm thick.
- Many materials are unstable in the presence of oxygen or water.
- As one-dimensional semiconductors, their electronic and optical properties can be highly anisotropic. This is potentially useful for device design.

It becomes imperative to discuss the general principle of working of organic photovoltaic device in order to do justice to this survey. The performance of organic solar cell can be divided in to seven processes. These are:

1. *Incoupling of the photon*: The devices are fabricated such that the substrate glass or quartz or polymer is the first material encountered by light. The criterion is to have

the material as transparent as possible to light. The reflection at air-substrate interface should be minimized. At normal incidence the higher the difference between optical refractive index of substrate and ambient, the higher the reflection loses. Manipulating the surfaces by having 1D diffraction grating etc can minimize the reflection losses. Antireflection properties can also be minimized by suitable choices of the thickness and dielectric function of the layers. For this it becomes essential to perform the optical simulation of the multilayered structure.

2. *Photon absorption*: The active layer is the layer where photon absorption leads to charge generation, so it is important to focus as much energy as possible to this active layer. Using optical simulation optical electric field can be found in all the layers and absorption is closely related to $|E|^2$, where E is the electric field. For materials prospective, it is important to have an absorption coefficient of active material that matches the solar spectrum.
3. *Exciton Formation*: After absorption, the photon energy leads to excitation in organic solid referred as exciton. The exciton consists of a pair of Coulomb-attracted electrons and holes, and is electrically neutral. Only a fraction of incoming photons turn into excitons.
4. *Exciton Migration*: Exciton diffuses through the material with its diffusion length of the order of 5-10 nm. Excitons also have a finite lifetime and they decay via several beneficial or loss processes. The loss process comprise of re-emission of photon, thermal and vibronic decay. The desired path is transformation of exciton into free electrons and holes at dissociation sites where there is sufficient electric field to

overcome the binding energy of excitons. The interface of two materials having different electron affinities also acts as an exciton dissociation site.

5. *Exciton Dissociation*: The exciton leads to free charge generation at dissociation sites. The recombination of these separated charges can also occur when the electric field is very small.
6. *Charge Transport*: The free charges must be allowed to reach the electrodes where they constitute the photocurrent from the device. Electrons and holes have different mobilities in the material. Charge trapping may occur which can reduce the photocurrent. So it is better to constraint the charge transport in a thinner layer to reduce risk of trapping. But optical absorption which is proportional to thickness is reduced in this attempt of enhancing charge transport.
7. *Charge collection:* If an electron or a hole is present close to an electrode, whether they will pass into the outer circuit depends on the geometry, interface formation and the band structure.

Over the past 20 years the structure of organic photovoltaic device has evolved a lot, as a result of the effort to enhance its efficiency. The first organic solar cell that was introduced comprised of single organic layer sandwiched between two metals having different work functions which provides for an electric field which drives separated charges towards the respective contacts. This setup is called homojunction [Figure 1.1(a)]. The electric field is not sufficient to break up the excitons. Also the exciton diffusion length which is only limited to 10 nm limits charge generation in such a device.

Most of the developments that have improved performance of organic photovoltaic devices are based on donor-acceptor heterojunctions. At the interface between two different

materials, electrostatic forces result from the differences in electron affinity and ionization potential. If both electron affinity and ionization potential are greater in one material (the

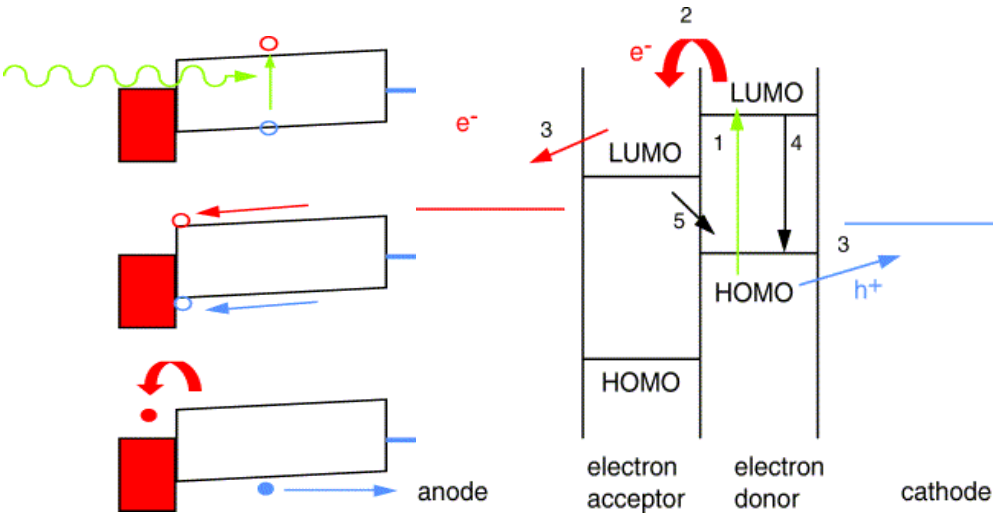

(a) (b)

Figure 1.1: (a) Schematic energy-band diagram of a simple device consisting of a single organic layer between two metal contacts. (b) Schematic energy-band diagram of a donor-acceptor heterojunction.

electron acceptor) than the other (the electron donor), then the interfacial electric field drives charge separation [Figure 1.1(b)]. These local electric fields are strong and may break up photogenerated excitons. In a planar heterojunction, or 'bilayer' device, the organic donor-acceptor interface separates excitons much more efficiently than the organic-metal interfaces in a single layer device and with very high purity materials efficient photovoltaic devices may be made. A revolutionary development in organic photovoltaics (and photodetectors) came in the mid-1990s with the introduction of a dispersed heterojunction, where an electron accepting and an electron donating material are blended together. If the length scale of the blend is similar to the exciton diffusion length, then wherever an exciton is photogenerated in either material, it is likely to diffuse to an interface and break up. If continuous paths exist in each material from the interface to the

respective electrodes, then the separated charge carriers may travel to the contacts and deliver current to the external circuit (Figure 1.2).

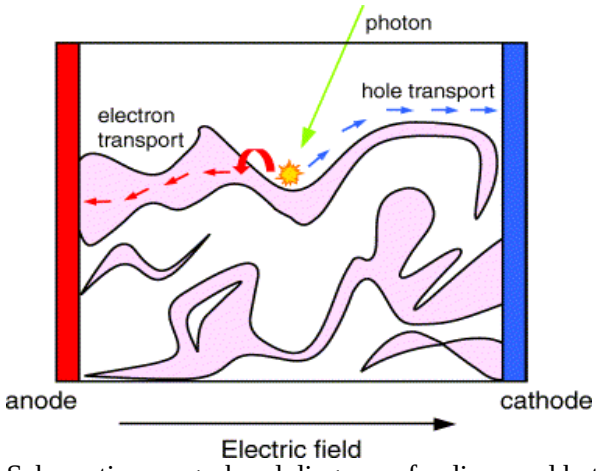

Figure 1.2: Schematic energy-band diagram of a dispersed hetrojunction.

1.2 Research Motivation

Among many factors, the crucial parameters that are restricting the efficiency of organic solar cells are: Poor light absorption and recombination losses.

a) Poor absorption: The high energy band gap of the polymer materials and weak absorbance poses a serious limitation on the capability to harvest sunlight. Moreover the charge carrier mobility of the materials is also moderate [8], which makes it necessary to keep the thickness of the active layer low to minimize recombination losses. Typical thicknesses of active layer in optimized BHJ devices is ~100 nm due to the performance-limiting trade-off between optical absorption and electrical transport, which are adequate for visible light absorption owing to strong extinction coefficient in this wavelength range [1-7]. A significant portion of the solar flux lies beyond λ = 600 nm, which is near the band edge of many BHJ materials. Recently many low-band gap polymers have been produced with broader absorption range to better harvest the solar spectrum, exhibiting

efficiencies of over 5% [9-12]. A few reports on these low-band gap polymers demonstrated internal quantum efficiency, IQE (fraction of collected carriers per absorbed photon) approaching 100% [11,12]. However, these low-band gap polymers suffer from poor absorbance (fractional number of absorbed photons from the solar spectrum) in their absorption range, for thicknesses optimized for electrical performance [9-11]. Hence absorbance of these low-band gap polymer based OPVs has to be improved, since optical losses may account for up to ~38% of the power conversion efficiency reduction. The constraints on active layer thickness of these OPVs make it imperative to develop light trapping schemes to enhance absorption in a specific spectral range with weak absorption without increasing photoactive layer thickness.

b) Recombination losses: (i) Singlet exciton (SE) recombination: when a film is excited from the absorption of a photon, the Coulombic binding between the HOMO residing electron and the LUMO residing hole gives rise to a quasi-particle called an exciton (typically these quasi-particles reside in the singlet quantum state) [13]. Due the relatively low permittivity of organic materials, the thermal energy available at room temperature is not sufficient to break the exictonic binding. Therefore, the SE must typically reach a donor/acceptor quenching interface within its ~10 nm diffusion length in order to separate. SE recombination during this diffusion process accounts for nearly 12% of efficiency loss in OPVs [14]. (ii) Deficient charge transfer exciton (CTE) quenching: if the said SE reaches a quenching interface, it decays to form a geminate electron-hole pair (the CTE) directly after the photoinduced electron transfer. This CTE must then be dissociated to form free carriers which can then (and only then) contribute to photocurrent. Geminate recombination of CTEs aggravates this process when the dissociation-driving

electric field is small, leading to a fundamental efficiency loss. Further, the loss of free carriers induced by non-geminate recombination further reduces the photocurrent and open-circuit voltage (V_{oc}); resulting in lower output power of the OPVs. It has been estimated that an efficiency reduction exceeding 32% can be attributed to non-radiative recombination (including both geminate and non-geminate) [14]. Hence there is a need to investigate the effect of processing conditions such as spin coating speed and drying rate on the recombination losses.

Generally, an external bias is required to collect all the photogenerated charges and thus prevent their recombination. The motivation is to induce additional electric field in otherwise low mobility conjugated polymer based active layer by incorporating ferroelectric dipoles. This is expected to facilitate exciton dissociation in polymer matrix and impede recombination at polymer:fullerene interface.

1.3 Literature Review

a) Light trapping techniques for increased absorption

(i) *Ray Optics Regime*: Light management techniques in ray optics regime, have been implemented for enhancement in optical absorption, e.g. collector mirrors [15], microprism substrates [16] and V-folded configurations [17]. *M. Niggemann et al.* [16] implemented microprism structure, for light trapping and hence enhancing absorption in the active layer. The setup has two advantages in comparison to the regular solar cell. ITO was substituted with a highly conducting metal grid located at the valley of the structure reducing the series resistance of the cell. Also the corrugated substrate ledto increased absorption by two fold reflection of the incident light. The thickness of the active layer and PEDOT was kept 100

nm for the sake of simulation and experimental results. The pitch size of grating structure was kept to be 100 μm. RCWA was used for optical simulation for TE, TM and unpolarized modes of light. The simulation results suggested higher absorption of light by microprism structure for both TE and TM modes as compared to planar solar cell. In order to confirm the simulation results by experimentation, the corrugated substrate was made by precision micro machining. Thin layer of gold was evaporated on the substrate and patterned using self-assembled photo lithography. The active layer and PEDOT were spin coated on the substrate. But the coating of polymer layers was not uniform as it was thicker in the valley and thin at the top of the pyramid. This led to more recombination of charges where the layer was thick as well as creation of shunt resistance at places where the layer was thin. Hence, the fill factor achieved in these devices was very low even though the short circuit current was higher as compared to planar cell having similar structure. This reduced over all power conversion efficiency to 1% as compared to flat cells having 4% efficiency.

Also at macroscale, where ray optics operates, an important study was performed by *Rim et al*. [17] on V-shaped light trapping configuration that substantially increases the photocurrent generation for all angle of incidence. A simple light trapping scheme was analyzed that structures thin-film solar cells on a length scale much larger than the active layer thickness and requires no modification of the device structure, keeping the low cost fabrication possible. The active layer and reflective metal electrode were deposited on a V-shaped transparent substrate coated with a transparent electrode such as indium tin oxide (ITO). Incident optical rays bounces off the solar cell structure multiple times contributing to increased optical absorption. This structure was modeled using a thin film organic solar

cell by transfer matrix method. Photocurrent generation was simulated by solving the exciton diffusion equation for planar organic solar cell and using the drift-diffusion model. The structure of the modeled cell was 1500 Å ITO/400 Å PEDOT: PSS/1000 Å poly-(3-hexylthiophene (P3HT):[6, 6]-phenyl C60 butyric acid methylester (PCBM) (1:1 blend by weight)/ 1000 Å Al. The model predicted 30% increase in the short circuit current and broadening of the external quantum efficiency for the polymer based cell. The modeling results were verified by experiment. However the economy of the scheme depends on the added cost of the material and shaped substrate. If the increase in efficiency is significant, only then it is rational to implement this scheme of light trapping.

(ii) *Submicrometer texturing using corrugated substrates (wave optics)*: Light trapping by means of a periodic patterning, has been achieved by using a corrugated substrate: Burried nanoelectrodes [18] and azo polymer based submicrometer periodic surface structure [19,20]. Moderate success has been achieved for patterned substrates targeting enhanced light absorption, with small molecules which can be thermally evaporated and conformal coating is achieved, irrespective of the underlying texture [19,21]. Small molecule solar cell on azo polymer based grating (period = 510 nm) [19], showed enhanced EQE and suppressed reflection as compared to Flat cell with same layer sequence and thicknesses. Niggemann et al. [21] also fabricated small molecule OPVs on microprism substrates and achieved conformal coating by thermal evaporation, but no enhancement in photocurrent with respect to planar OPV was realized.

However challenges in obtaining a conformal coverage of solution processed polymers on these textured substrates [16,18,20], with coating technologies such as spin-

coating, spray coating, inkjet printing, doctor blading, gravure and flexo graphic printing, remains serious limitation of these periodic structures. Attempts of spin coating BHJ layer on textured substrates lead to over filling of the valleys and shunts at the crest, which severely restrained the electrical performance of these OPVs, owing to high charge carrier recombination and leakage current [16,18].

(iii) *Submicrometer pattering of active layer (wave optics):* Light trapping by means of a periodic patterning, has been achieved by texturing active layer into photonic crystal structure [22] or surface relief gratings [23,24] at the optical length scale, using soft lithographic techniques such as soft-embossing [23,24] and PRINT [21]. Surface relief gratings (SRGs) on photoactive layer by soft lithography, have shown greater promise. The increase in cell efficiency of SRG OPVs by pattering of active layer is mostly due to increase in short circuit current induced by more photogenerated charge carriers by stronger absorption of an active layer, resulting from the increase of optical path length and light trapping. But, in this scheme absorption enhancement was not tailored to a desired spectral range.

Furthermore, these techniques require additional processing step of active layer which increases the risk of contamination and oxidation of active layer surface, leading to schottky barrier formation at metal/polymer interface [25].

(b) Recombination mechanisms: In OPVs with both trap-free electron and hole transport in the acceptor and donor, respectively, the main recombination mechanism for the free charge carriers is bimolecular recombination. The bimolecular recombination rate is given in this case by

$$R_{Bimolecular} = \gamma\left(np - n_i p_i\right) \tag{1}$$

Where *n(p)* is the free electron (hole) density, $n_i(p_i)$ is the intrinsic electron (hole) density, and γ is the Langevin recombination constant [26]. A wide range of publications have reported that the dominant recombination mechanism in organic solar cells is bimolecular. These studies were based on different techniques in the time and frequency regime [27,28]. The authors of these studies share the opinion that non-geminate bimolecular recombination is a strongly limiting factor in organic solar cells.

However, there exists a contradictory school of thought that suggests recombination at interface states (defects) rather than at charge transfer excitons, is the governing mechanism that determines the shape of the solar cell characteristics for the BHJ solar cell [29]. When defect states are present in the electron donor, the dissociation of bound pairs at the interface leads to free carriers, but now part of the holes can be trapped. For the holes trapped close to the interface, there is a probability of recombination with the free electrons in the acceptor, leading to loss of both carriers. The trap-assisted recombination rate is given by the Shockley-Read-Hall (SRH) equation

$$R_{Trap-assisted} = \frac{C_n C_p N_t \left(pn - p_1 n_1\right)}{\left[C_n\left(n + n_1\right) + Cp\left(p + p_1\right)\right]} \tag{2}$$

Where C_n and C_p are the capture coefficients of electrons and holes, respectively, N_t is the density of hole traps, n and p are the electron density in the conduction band and the hole density in valence band, and $p_1 n_1 = N_c N_v \exp[-(E_c - E_v)/kT] = n_i^2$, with n_i the intrinsic carrier concentration in the sample [30,31]. This trap-assisted recombination process adds to the Langevin (bimolecular) recombination, contributing to loss mechanisms in a BHJ OPV.

1.4 Thesis Organization

All of the remaining chapters are modified from published journal papers, which have me as first/primary author. The rest of the dissertation is organized as follows.

Chapter 2 is modified from the journal paper “Design of light-trapping microscale-textured surfaces for efficient organic solar cells", published in *Optics Express*, vol. 8(5), pp. 5168-5178, 2010. This chapter investigates the design of grating-type OPV cells using finite element method of simulations. The energy dissipation of electromagnetic field in the active layer is studied as a function of active layer thickness, and pitch and height of the underlying textures. Simulations are performed to demonstrate the superiority of textured geometry in terms of light trapping.

Chapter 3 presents the results of the journal paper titled “On realizing higher efficiency polymer solar cells using a textured substrate platform” published in *Advanced Materials*, vol. 23, pp. 112-116, 2011. In this chapter, performance dependence of grating based solar cells on underlying topography is discussed. Importance of realizing conformal coatings of active layer on textured substrates is demonstrated. An optimal dimension of textured geometry is discovered, that is amenable to coating a conformal active layer and exhibits photovoltaic efficiency improvement.

Chapter 4 discusses first report on lifetime based all-organic bio-chemical sensor titled “Polythiophene-fullerene based photodetectors: Tuning of spectral response and application in photoluminescence based (bio)chemical sensors” published in *Advanced Materials*, vol. 22, pp. 4157-4161, 2010. Demonstrated in this chapter is a photoluminescence (PL) based oxygen sensor utilizing inorganic or organic light emitting diode as the light source, and a poly(3-hexylthiophene):fullerene bulk-heterojunction type

devices as the photodetectors, for both intensity and decay-time based detection of the sensing element's photoluminescence. Processing of the photodetector's active layer was tailored to improve the photoresponse in the red, which otherwise peaks in the green and is weak in the red. This was required since photoluminescence of the sensing film is in the red region (~640 nm).

Chapter 5 studies the effect of processing conditions such as spin-coating speed and drying rate on the density of defects in poly(3-hexylthiophene) (P3HT):fullerene-derivative (PCBM) solar cells, as reported in journal paper titled "Growth rate dependent trap density in polythiophene-fullerene solar cells and its implications" published in *Applied Physics Letters*, vol. 98, 093306, 2011. Density of defects in organic solar cells is measured using capacitance techniques and correlated with photovoltaic performance. The light-intensity dependence of open-circuit voltage is used as a characterization tool to quantify the strength of interfacial recombination in organic solar cells.

In chapter 6, a paper submitted to *Advanced Functional Materials* titled "Dominant recombination mechanism in polymer solar cells is bimolecular or interfacial: depends on processing conditions of active layer" is discussed. This chapter investigates the effect of growth rates on recombination dynamics in P3HT:PCBM based organic solar cells, and their influence on the device performance. Two major recombination losses, bimolecular and interfacial, are discussed in detail in this chapter and their rates are calculated for devices with different growth conditions. In this study, experimental results and device parameters are coupled with a drift-diffusion based device model, to determine the dominant recombination mechanism.

A novel approach of improving the performance of OPVs by incorporating ferroelectric polymer is detailed in chapter 7 (modified from paper submitted to *Nature Materials*). Two kinds of OPV structures are studied to understand the effect of ferroelectric addition, namely: bulk heterojunction and bilayer. All possible mechanisms responsible for inducing performance enhancement in ferroelectric doped-OPVs are evaluated individually and in-depth characterization is performed to recognize the most likely contributing mechanism. Conclusions and future work are discussed in Chapter 8 and 9 respectively.

1.5 References

[1] N. S. Sariciftci, L. Smilowitz, A. J. Heeger, andF. Wudl, Science **258**,1474 (1992).

[2] G. Yu andA. J. Heeger, J. Appl. Phys.**78**, 4510(1995).

[3] J. J. M.Halls, C. A. Walsh, N. C. Greenham, E. A. Marseglia, R. H. Friend, S. C. Moratti, and A. B. Holmes, Nature**376**, 498 (1995).

[4] G. Yu, J. Gao, J. C. Hummelen, F. Wudl, and A. J. Heeger, Science**270**, 1789(1995).

[5] W. L. Ma, C. Y. Yang, X. Gong, K. Lee, and A. J. Heeger, Adv. Funct. Mater. **15**, 1617 (2005)

[6] G. Li, V. Shrotriya, J. Huang, Y. Yao, T. Moriarty, K. Emery, and Y. Yang, Nat. Mater. **4**, 864 (2005).

[7] S. Chaudhary,H. Lu,A. M. Müller,C. J. Bardeen, andM. Ozkan,Nano Lett.**7**, 1973 **(**2007).

[8] R. J. Kline, M. D. McGehee, E. N. Kadnikova, J. Liu, and J. M. J. Fréchet,Adv. Mater. (Weinheim, Ger.) **15**, 1519 (2003).

[9] Y. Liang,Y. Wu, D. Feng, S. Tsai, H. Son, G. Li, and L. Yu., J. Am. Chem. Soc. **131**, 56 (2009).

[10] J. Peet, J. Y. Kim, N. E. Coates, W. L. Ma, D. Moses, A. J. Heeger, and G. C. Bazan, Nature Mater. **6**, 497 (2007).

[11] H. Chen, J. Hou, S. Zhang, Y. Liang, G. Yang, Y. Yang, L. Yu, Y. Wu, and G. Li, Nature Phot. **3**, 649 (2009).

[12] S. Park, A. Roy, S. Beaupré, S. Cho, N. Coates, J. Moon, D. Moses, M. Leclerc, K. Lee, and A.J. Heeger, Nature Phot. **3**, 297 (2009).

[13] X. Y. Zhu, Q. Yang, andM. Muntwiler, Accounts of Chemical Research**42**, 1779, (2009).

[14] T. Kirchartz, K. Taretto, andU. Rau, J. Phys. Chem.C**113**, 17958 (2009).

[15] P.Peumans, V. Bulovic´, andS. R. Forrest, Appl. Phys. Lett.**76**, 2650 (2000).

[16] M. Niggemann, M. Glatthaar, P. Lewer, C. Muller, J. Wagner,and A. Gombert, Thin Solid Films **511,**628 (2006).

[17] S. Rim, S. Zhao, S. R. Scully, M. D. McGehee, and P. Peumans, Appl. Phys. Lett.**91**, 243501 (2007).

[18] M. Niggemann, M. Glatthaar, A. Gombert, A. Hinsch,and V. Wittwer, Thin Solid Films **451**,619 (2004).

[19] C. Cocoyer, L. Rocha, L. Sicot, B. Geffroy, R. de Bettignies, C. Sentein, C. Fiorini-Debuisschert, and P. Raimond**,** Appl. Phys. Lett. **88**, 133108 (2006).

[20] C. Cocoyer, L. Rocha , C. Fiorini-Debuisschert, L. Sicot, D. Vaufrey, C. Sentein, B. Geffroy, and P. Raimond,Thin Solid Films**511-512**, 517 (2006).

[21] M. Niggemann, M. Riede, A. Gombert, and K. Leo, Phys. Stat. Sol. (a) **205**, 2862 (2008).

[22] D. Ko, J.R. Tumbleston, L. Zhang, S. Williams, J.M. DeSimone, R. Lopez, and E.T. Samulski, Nano Lett.**9**, 7 (2009).

[23] S. Na, S. Kim, J. Jo, S. Oh, J. Kim, and D. Kim, Adv. Funct. Mater. **18**, 3956 (2008).

[24] L. S. Roman, O. Inganäs, T. Granlund, T. Nyberg, M. Svensson, M. R. Andersson, and J. C. Hummelen, Adv. Mater. (Weinheim, Ger.) **12**, 189 (2000).

[25] G. Belmonte, A. Munar, E.M. Barea, J. Bisquert, I. Ugarte, and R. Pacios, Org. Electron.**9,** 847(2008).

[26] P. Langevin, Annales De Chimie Et De Physique**28**, 433 (1903).

[27] A. Foertig, A. Baumann, D. Rauh, V. Dyakonov, and C. Deibel, Appl. Phys. Lett.**95**,052104(2009).

[28] A. Pivrikas, G. Juska, A. J. Mozer, M. Scharber, K. Arlauskas, N. S. Sariciftci, H. Stubb, and R. Osterbacka, Phys. Rev. Lett. **94**, 176806 (2005).

[29] R. A. Street, M. Schoendorf, A. Roy, and J. H. Lee, Phys. Rev. B**81,**205307 (2010).

[30] M. M. Mandoc, F. B. Kooistra, J. C. Hummelen, B. d. Boer, and P. W. M. Blom, Appl. Phys. Lett.**91**,263505(2007).

[31] M. M. Mandoc, W. Veurman, L. J. A. Koster, B. de Boer, P. W. M. Blom, Adv. Funct. Mater. **17**, 2167(2007).

CHAPTER 2. Design of light-trapping microscale-textured surfaces for efficient organic solar cells[1]

Modified from a paper published in *Optics Express*

Kanwar S. Nalwa[2,3], and Sumit Chaudhary[2,4]

2.1 Abstract

Organic photovoltaic (OPV) cells suffer from low charge carrier mobilities of polymers, which renders it important to achieve complete optical absorption in active layers thinner than optical absorption length. Active layers conformally deposited on light-trapping, microscale textured, grating-type surfaces is one possible approach to achieve this objective. In this report, we analyze the design of such grating-type OPV cells using finite element method simulations. The energy dissipation of electromagnetic field in the active layer is studied as a function of active layer thickness, and pitch and height of the underlying textures. The superiority of textured geometry in terms of light trapping is clearly demonstrated by the simulation results. We observe 40% increase in photonic absorption in 150 nm thick active layer, for textures with 2 μm pitch and 1.5 μm height.

2.2 Introduction

Polymer and small-molecule based OPVs have gained a lot of attention in the last decade due to their potential low cost and roll-to-roll manufacturing capability, and amenability to flexible substrates. Most of the developments that have improved

[1] K. S. Nalwa, and S. Chaudhary,"Design of light-trapping microscale-textured surfaces for efficient organic solar cells", *Optics Express*, **8**, 5168-5178, 2010. Reprinted with permission from OSA.
[2] Graduate student and Assistant Professor, respectively, Department of Electrical and Computer Engineering, Iowa State University.
[3] Primary researcher and author.
[4] Author for correspondence

performance of OPVs are based on electron donor-acceptor (D-A) heterojunctions. In a planar heterojunction, or 'bilayer' device, excitons are dissociated into charge-carriers at the D-A interface. The efficiency of PV conversion is however low because only the excitons created within the exciton-diffusion length from the D-A interface are utilized [1-3]. A revolutionary development in OPVs came in the mid-1990s with the introduction of bulk-heterojunction OPVs, in which the D-A materials are blended together [4-6]. If the length scale of the phase-separation in D-A blend is similar to the exciton-diffusion length, then all excitons photogenerated in either material are likely to diffuse to an interface and dissociate into free charge carriers. These charge carriers are then drifted to the respective electrodes if continuous pathways exist in each material. The electron acceptors are often the fullerenes or their derivative [6,6]-phenyl-C61-butyric acid methyl ester (PCBM) having better miscibility in organic solvents. For OPVs with poly(3-hexylthiophene) as electron donor, highest efficiencies reaching up to 5% have been reported [7-8].

The performance of these bulk heterojunction devices is still limited by several factors. The high energy band gap of the most polymer materials poses a serious limitation on the capability to harvest lower energy photons from sunlight. Moreover, the charge carrier mobility of these materials is low [9], making it necessary to keep the thickness of the active layer low. A thinner film between the electrodes can lower the probability for charge recombination, and increase the carrier drift velocity due to higher electric field. However, the optical absorption will be low in such thin films. Thus, there is a conflict between the optical and the electronic length-scales. A unified concept of anti-reflection coatings and distributed Bragg reflectors is one method recently suggested to increase the absorption in thin OPV films [10]. Another way to resolve this conflict can be a textured,

grating-shaped OPV cell geometry. Submicron or micron structures can modify the incident wave momentum in such a way that the incident light remains trapped in the solar cell active layer due to total internal reflection at the interfaces [11,12]. This results in increased absorption in the active layer, and facilitates the use of layers with optimum thickness with regard to the electrical properties. The perceived optoelectronic benefits of using these light trapping structures have led to the recent development of embossing being successfully applied to the patterning of polymer OPVs, leading to a significant increase in generated photocurrent [13]. A more recent work focused on enhancing absorption in the active layer by implementing light trapping structures like diffraction-gratings and buried nano-electrodes [14]. However, in these reports, study was carried out for a single pitch and active layer thickness. What should be the optimum dimensions of a micron or submicron-scale grating in OPVs – is an open question. In the present study, we therefore investigate in detail, the effect of pitch, height and active layer thickness on the performance of grating-based textured OPVs. It should be noted that similar studies for silicon-based solar cells [11,12] are not directly relevant for OPVs due to difference in active layer thicknesses between these two technologies. For thin-film silicon solar cells, grating structures serve more of a back reflector role for a thicker active layer. However, in OPVs, active layer will be much thinner and conformal with the textured surfaces.

For planar solar cells, optimization has been performed using optical models based on transfer matrix formalism for normal light incidence [15]. This approach however is not suitable for the optical modeling of textured grating-based OPV cells, since the grating pitch is of the order of wavelength of light leading to complex diffraction and interference effects that have to be included in the model. Finite element model inbuilt in COMSOL

MULTIPHYSICS has been used to perform the simulations, accounting for the three-dimensional geometry and wavelength dependence of dielectric functions for materials. Optical modeling was performed to calculate an optimum grating geometry and to gain a better understanding of the light absorption in the textured solar cells. The energy dissipation of electromagnetic field in the active layer was studied as a function of active layer thickness, grating pitch and height.

The evaluated cells consist of four layers: ITO (100 nm), poly(3,4 ethylene dioxythiophene):poly(styrene sulfonate) (PEDOT:PSS)~ 50 nm, P3HT:PCBM blend(1:1) as the active layer and titanium (250 nm). The active layer thickness was varied keeping the thickness of other layers constant. The cells have inverted geometry, with ITO on the top and Ti as bottom electrode, allowing light incidence from the top. In practice, ITO layer can be sputtered on the top of a protective buffer layer such as MoO_3 to prevent degradation of PEDOT layer from plasma exposure [16]. ITO is required for top illumination and direct comparison of textured OPVs with bottom illuminated planar cells on ITO substrate. Ti is used instead of Al as bottom electrode since oxidation of Al leads to degradation of electrical contact and inverted solar cell structures employing Ti as bottom contact have been demonstrated earlier [17].

2.3 Simulation setup

The simulations were performed on the tapered structures depicted in Figure 2.1, with a series of stacked layers with different optical properties. For use in our model, the complex refractive indices ($n + ik$) as a function of wavelength were obtained from the literature [18-21]. In the simulations, light enters from air, and is incident on the OPV cell

at air-ITO interface. In the case of textured solar cells, the incident wave was generated at a boundary, with a condition allowing the generated wave to enter the structure, and the wave reflected from the structure to be transmitted through this boundary, into a perfectly matched layer. This perfectly matched layer is simulating the semi-infinite surrounding by absorbing all the outgoing waves.

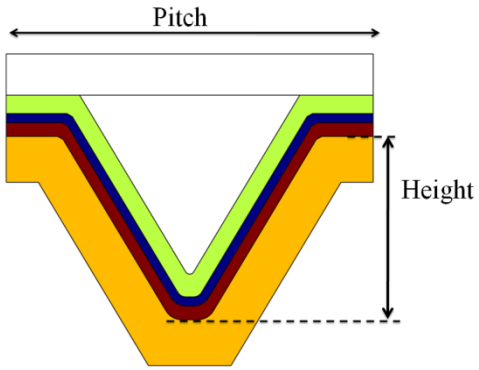

Figure 2.1: Structure of the modeled grating-based OPV cell. At the bottom is a Ti layer, on which the P3HT:PCBM active layer, the PEDOT:PSS layer, and the ITO layer are sequentially located.

In order to avoid complexity, the anisotropy of dielectric function found in some materials is not represented in this model. The electromagnetic wave equations were solved on the entire defined geometry taking into account the interference, refraction and reflection effects. In order to fix the geometry of the textured devices used for simulations, irrespective of the pitch, slope of the grating was kept constant for structures having same aspect ratio (pitch:height). Moreover, opening ($7/10^{th}$of pitch) and bottom width ($1/10^{th}$ of pitch) of the grating was kept same for a given pitch size and varied proportional to the pitch size. The range of wavelengths chosen for the simulations is 300-700 nm with incident power being defined by AM 1.5 sun light spectra. Since different pitch structures had different area sizes exposed to the incoming solar flux, the incident power was normalized with respect to 1 μm pitch size, giving it the unit of W/m^2. The electromagnetic

power dissipation per volume, Q, in the active layer is studied as a criterion to optimize the height and pitch of the structures as well as the active layer. The total power absorbed (W/m^2) in a layer was calculated by integrating Q over the active layer space, summing over all the wavelengths and then normalizing with respect to the 1 μm pitch.

2.4 Experimental details

The modeled data for the planar configuration was compared with experimental results to verify the accuracy of refractive indices used in the simulations. Planar structures were fabricated with similar layer sequence as their modeled counterparts. A titanium layer was evaporated on cleaned glass slide. The P3HT:PCBM blend with 1:1 weight ratio was used. P3HT concentration was 17 mg/ml in dichlorobenzene solution. The blend solution was spin coated on top of the titanium layer. A conducting film of PEDOT:PSS was spin coated on the photoactive layer to act as anode. Reflectance of this structure was measured using Varian Cary 5000 UV-Vis-NIR spectrophotometer and used as a criteria for authenticity of optical constants employed in simulations.

2.5 Results and discussion

In order to confirm and validate the simulation results of FEM model, simulations of planar stacked layers were performed with the use of transfer matrix method (TMM) and compared with the FEM results on the same. The results of FEM and TMM simulations on planar OPV cell showed good agreement. Simulations on fabricated planar structure were performed with the layer thicknesses obtained from surface profiler measurements to

predict the reflectance. A good fit between the measured and simulated reflectance is obtained as shown in Figure 2.2. A small deviation is exhibited which can be due to non-homogenous spin coated layers.

Figure 2.3 shows the variation of energy dissipation in the active layer for different pitches and heights of the grating structure. The results reveal that absorption is least for 500 nm pitch, which can be attributed to the increased reflection of higher order diffracted light when grating period is less than the wavelength of light. With 1 μm pitch, the grating period is more than the relevant wavelengths, hence reflection of light due to higher order diffraction will be low, leading to light trapping effects in the active layer. It is also observed that 1 μm pitch structure with 750 nm height (aspect ratio 4:3) leads to highest absorption in the active layer. For 2 μm pitch also, the same aspect ratio (4:3) leads to highest absorption. As the height of the structure increases, the effective volume of active layer available for absorption increases too. However, the grating becomes narrower and the coupling of light decreases. These two trends have a push and pull effect on the optimum height for highest absorption.

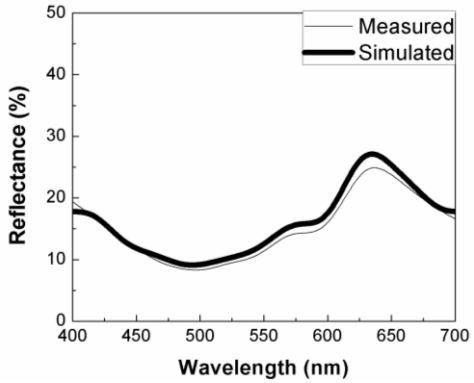

Figure 2.2: Measured and simulated reflectance from planar cell. Layer thicknesses used in the simulations are PEDOT:PSS: 50 nm and active layer: 70 nm.

For pitch size of 4 μm, bulk effects start dominating and diffraction effects become small. Hence, the only parameter that affects the absorption in 4 μm pitch structures is the volume of the active layer which increases with the height of grating. Overall, the structure with 2 μm pitch and 1.5 μm height showed highest absorption of incident power in the active layer and hence appears to be most promising among all the micro-regime dimensions. This structure is accompanied with 36% increment in energy dissipation inside the 75 nm thick active layer with respect to the planar cell. The energy dissipation relative to corresponding planar cell is greater than unity for all the textured geometries irrespective of their pitch and height, which can be explained by contributions from increased light concentration and effective area.

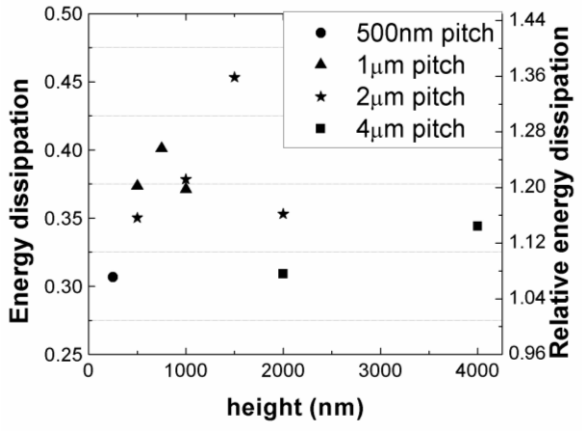

Figure 2.3: (left) Energy dissipation (as fraction of incident power) in the active layer, as a function of height and pitch of the grating. Active layer thickness is 75 nm. Thickness of PEDOT:PSS and ITO is 50 and 100 nm, respectively.Right hand side axis has energy dissipation in active layer relative to corresponding planar cell.

The energy dissipation inside textured devices at 500 nm wavelength (important for photocurrent generation in P3HT-based OPVs) for 2 μm pitch - 1.5 μm height, and 1 μm pitch - 750 nm height structures is plotted in Figure 2.4(a) and (b). The excitation beam is transverse electric (TE) polarized, i.e., with a polarization along the grating stripes. The

bright spots in the active layer show the maximum energy dissipation regions. In case of TE polarized light, power flow gets channeled in these regions as shown by arrows and results in the focusing of electromagnetic energy inside the active layer [Figure 2.4(a) and (b)]. This feature originates directly from the diffraction of a part of the incident light on to tapered structure, according to the following formula:

$$k_d \sin\theta_d = \pm k_i \sin\theta_i \pm \frac{2\pi m}{\Lambda} \tag{1}$$

where Λ is the width of the tapered structure at some height, k_i (k_d) is the incident (diffracted) light wave vector, θ_i (θ_d) is the light incident (diffracted) angle, and m is an integer corresponding to the diffraction order.

The region where the incident light is diffracted with an angle θ_d, greater than the angle that slope of grating makes with normal i.e. θ_c as shown in Figure 2.4(a), standing wave will be formed. This wave is confined by total internal reflection at the polymer/air interface and the metal grating reflection. A part of the light will then propagate and get dissipated in the active layer, leading to an enhancement in the absorption around that region. In the present case of normal incidence (sin θ_i= 0), Eq. (1) can be simplified to following form:

$$\sin\theta_d = \pm \frac{m\lambda}{\Lambda n} \tag{2}$$

Where λ is the wavelength of light and n is the refractive index. From Eq. (2) it can be deduced that the diffraction angle will be small where width is large and hence the diffracted light will escape the structure without getting coupled into the polymer layer. For effective coupling to take place, the diffracted light has to be guided parallel to the slope of the tapered structure which happens when width becomes sufficiently small. This is the

reason why maximum energy dissipation takes place approximately at the same opening width for the two structures of Figure 2.4(a) and (b), having same aspect ratio or slope (4:3) at 500 nm wavelength. Similar results were obtained for other aspect ratios dealt in this study (not shown here). Figure 2.4(c) clearly evidences that in case of TM polarized light, the power flow is along the incident wave propagation direction and almost unaffected by the grating. This is similar to the case of planar cell [Figure 2.4(d)] and therefore doesn't lead to significant enhancement in absorption.

From Figure 2.5 (a), the ratio of maximum absorption height level and the total height of grating is found to decrease on increasing the pitch. This is because the width at which light diffraction suitable for trapping takes place, lies closer to the bottom of the grating for bigger pitches. On decreasing the aspect ratio, the grating structure becomes narrower and hence the energy concentration region shifts farther from the bottom of the grating. This explains the reason for lower aspect ratio having larger ratio of maximum absorption height and height of grating for a fixed pitch, as shown in Figure 2.5(a). For 2 μm pitch-1.5 μm height grating structure, the maximum absorption height increases with increasing wavelength of incident TE polarized light as seen in Figure 2.5(b). This result can be explained by using Eq. (2), according to which, wavelength of the light diffracted parallel to the slope of grating i.e. $\theta_d = \theta_c$, is proportional to the grating's width for standing wave formation.

Higher photonic absorption in the textured structures arises mostly from the guiding of diffracted TE polarized part of incident light in the polymer layer with little enhancement from TM polarization, as seen in Figure 2.6. In the case of TM polarized excitation beam, a

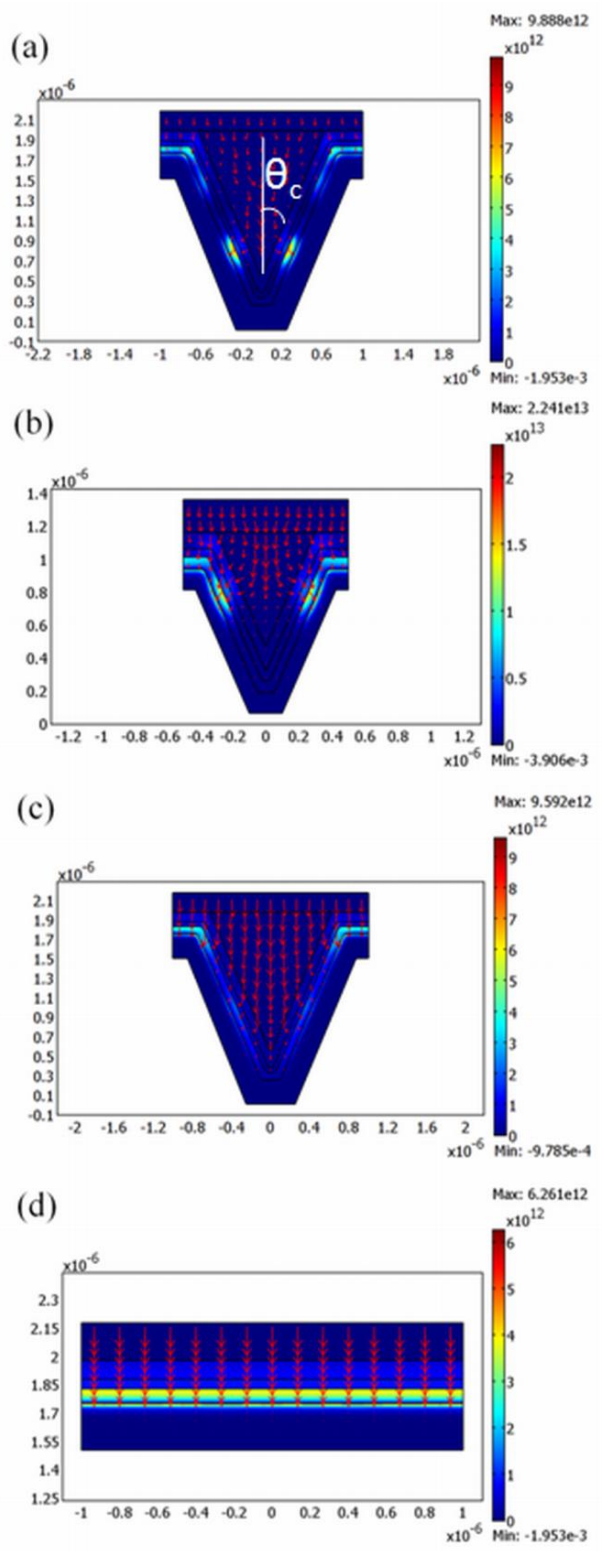

Figure 2.4: Energy dissipation (W/m^3) colored map at 500 nm wavelength of light for (a) TE polarization in 2 μm pitch - 1.5 μm height (b) TE polarization in 1 μm pitch – 750 nm height and (c) TM polarization in 2 μm pitch - 1.5 μm height (d) Flat structure, with arrows showing power flow

(time averaged). The thicknesses of ITO, PEDOT:PSS and active layer are 100, 50 and 75 nm respectively. Unit is meters for geometry.

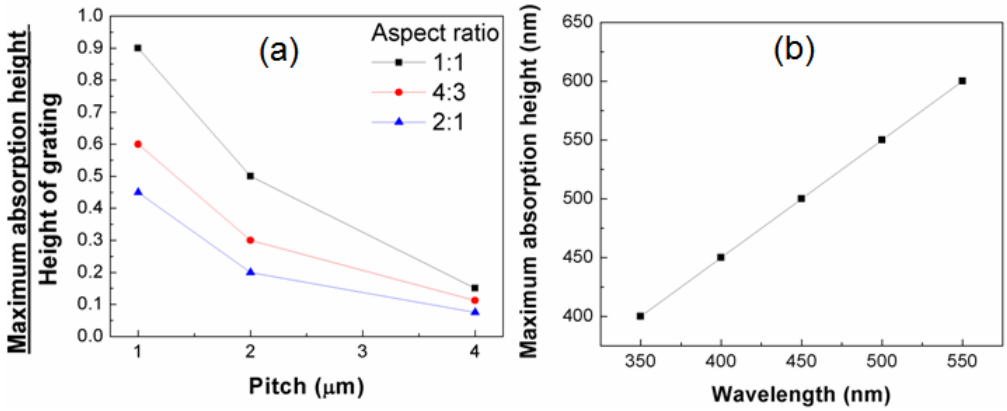

Figure 2.5: (a) Dependence of the ratio of maximum absorption height and height of grating on pitch size for 1:1, 4:3 and 2:1 aspect ratios for TE polarized light of 500 nm wavelength. (b) Variation of maximum absorption height with wavelength of TE polarized excitation light in 2μm pitch-1.5μm height grating structure. The thicknesses of ITO, PEDOT:PSS and active layer are 100, 50 and 75 nm respectively.

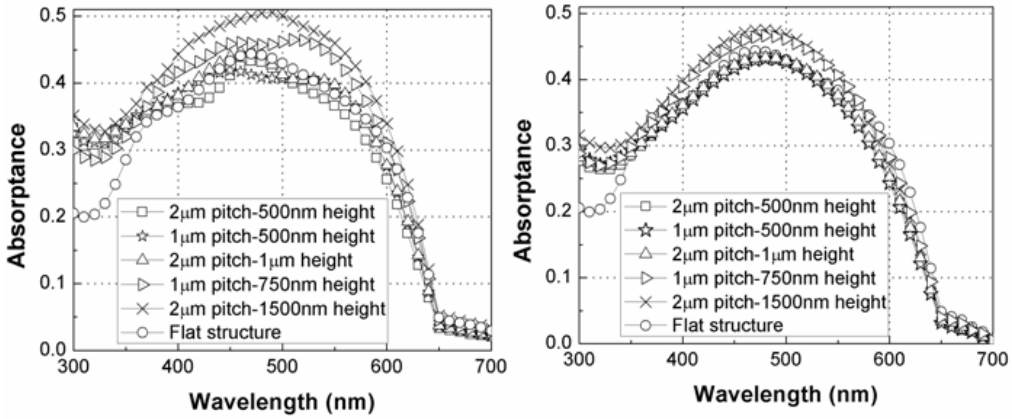

Figure 2.6: Absorptance in 75 nm thick active layer for various textured structures and flat cell with PEDOT:PSS and ITO layer thickness of 50 and 100 nm, respectively in the case of TE (left) and TM (right) polarizations of incident light.

small increment in the absorption for all grating structures relative to the planar cell can be a consequence of increased area available for absorption in grating structures. The dip in the absorption below 350 nm in the planar cell is accordingly filled up and almost removed by making use of textured structures, as displayed in Figure 2.6. The thickness of the active

layer studied (75 nm) is less than the absorption length at short wavelengths too. Therefore, some of the absorption enhancement for short wavelength (300-500 nm) comes from coupling of incident light into the modes that are guided in the active layer, hence enhancing the light travelling path and providing a light trapping mechanism. Remaining enhancement can be attributed to better effective refractive index matching with air (antireflection effect) that suppresses light reflection significantly. The wave guiding effect is particularly important for long wavelength regime where the active layer is less absorptive and a single path cannot absorb all incident light. This can be elucidated by appreciable absorptance enhancement ratio at wavelengths longer than 550 nm, as shown in Figure 2.7.

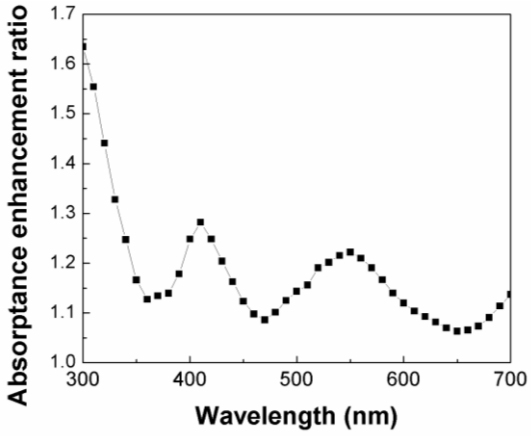

Figure 2.7: Absorptance enhancement ratio (Absorptance ratio of 2 μm pitch-1.5 μm height grating and flat cell) as a function of wavelength for 75 nm thick active layer. The thicknesses of PEDOT:PSS and ITO layers are 50 and 100 nm respectively.

Figure 2.8 shows energy dissipation profiles perpendicular to the layers and at different heights from the bottom of our most promising 2 μm pitch - 1.5 μm height textured cell. The intensified energy dissipation caused by the confinement of

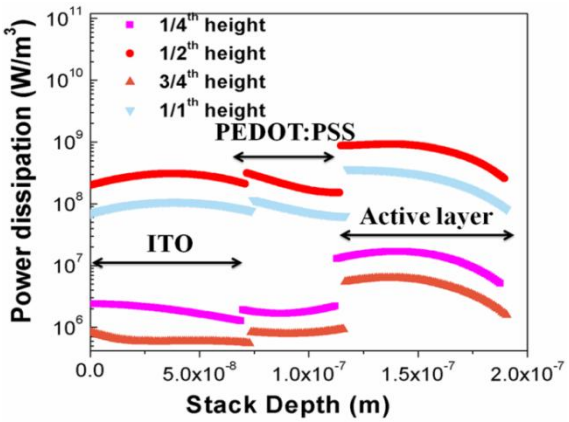

Figure 2.8: Energy dissipation at 1/4, 1/2, 3/4 and 1 of the height, measured from the bottom of the 2 μm pitch - 1.5 μm height grating. Thicknesses of ITO, PEDOT:PSS and active layer are 75, 40 and 75 nm respectively.

electromagnetic wave in the structure can be seen, with largest absorption occurring at 1/2 height. This light trapping is also evident from Figure 2.9 which shows the effect of active layer thickness on the absorption for textured (2 μm pitch - 1.5 μm height) and planar OPVs with 100 nm, and 50 nm thick ITO and PEDOT:PSS layers, respectively. Although the absorption increases with the increasing thickness of the active layer for both geometries - planar as well as textured - it is observed that the absorption relative to the corresponding planar cell is maximum for 150 nm thick active layer (1.5 and 1.3 times for TE and TM modes, respectively) as displayed in the insets of Figure 2.9. The observation that absorption enhancement as a result of texturing has a maxima and is not a monotonically decreasing function of active layer thickness is attributed to interference effects, making some layer thicknesses more beneficial for energy trapping. The absorption at higher active layer thicknesses (200-250 nm) saturates, indicating that there is very little light that is reflected or absorbed in the metal and is left to be absorbed in the photoactive layer. This has an important implication for textured geometries - that the 150 nm active layer

thickness is not only competitive with the 250 nm thickness in terms of absorption, but it will also significantly improve the carrier transport [22].

Energy dissipation maps are plotted for 2 μm pitch-1.5 μm height grating with 75 and 250 nm thick active layer [Figure 2.10(a) and (b)] and compared with a flat cell with 75 nm active layer thickness [Figure 2.10(c)]. For the same thickness of active layer, textured cell shows a significantly smaller reflectance than planar cell, due to the increased absorption in the active layer as well as in ITO. On increasing the thickness of active layer from 75 nm to 250 nm for the 2 μm pitch-1.5 μm height structure, the enhanced absorption in the polymer layer is mostly induced by reduction of energy dissipation inside the metal.

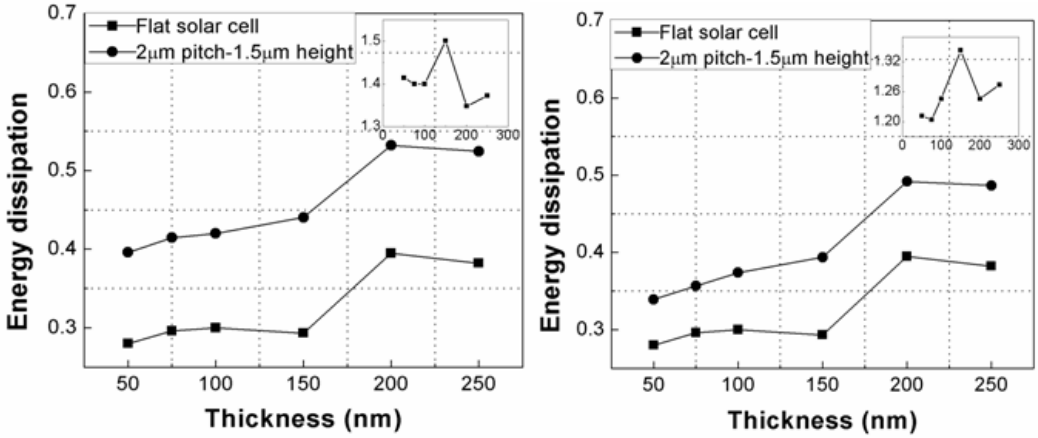

Figure 2.9: Variation of energy dissipation (as fraction of incident power) in the active layer for different active layer thickness for textured (2 μm pitch - 1.5 μm height) and planar OPV cell in case of TE (left) and TM (right) polarizations of incident light. Inset graph in the top right corner displays energy absorbed in textured relative to planar cell as a function of active layer thickness.

For solar cells in a practical environment where sunlight can be quite diffused, it is important to evaluate the absorptance over a wide range of incident angles. Figure 2.11(a) suggests that 2 μm pitch-1.5 μm height grating structure has a distinguished advantage over flat device for all incident angles and thus in the real environment. The absorption

efficiency of flat surface drops more abruptly as the incident angle increases when compared to grating structure, as shown in Figure 2.11(b).

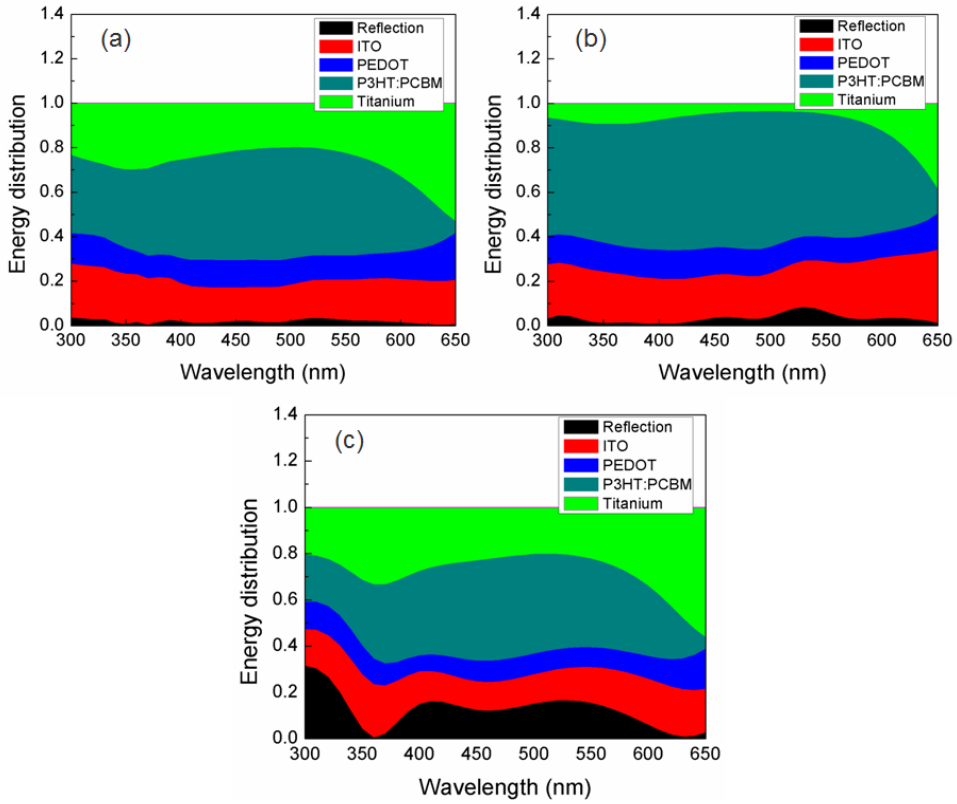

Figure 2.10: Energy dissipation maps in (a) 2 μm pitch-1.5 μm height grating with 75 nm thick active layer (b) 2 μm pitch-1.5 μm height grating with 250 nm active layer thickness (c) flat cell with 75 nm active layer thickness. Thickness of PEDOT:PSS and ITO is 50 and 100 nm respectively.

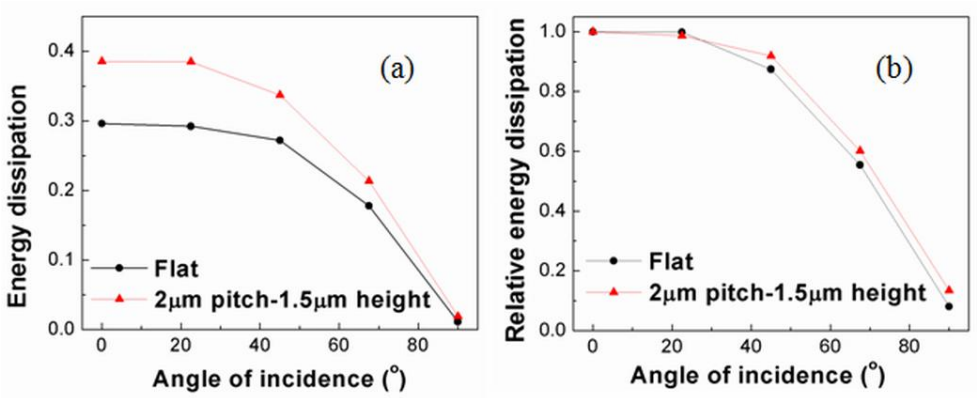

Figure 2.11: (a) Energy dissipation (as a fraction of incident power) and (b) Relative Energy dissipation (as fraction of energy dissipated at 0^{o} or normal incidence) (right) in 75 nm thick active layer (P3HT /PCBM) as a function of incident angle, for flat and 2 μm pitch-1.5 μm height grating. Layer thicknesses used in the simulations are PEDOT:PSS: 50 nm and ITO: 100 nm.

Higher relative energy dissipation [Figure 2.11(b)] in grating structure is attributable to the suppression of reflection loss.

2.6 Conclusions

Using the finite element method, we have modeled the optical behavior of microscale textured OPVs in comparison with the conventional planar geometry. A maximum of 40% increase in photonic absorption is observed in active layer (150 nm) for grating-type bottom electrode with 2 μm pitch and 1.5 μm height texture. Our results show that if an OPV active layer is conformally deposited on a textured electrode, it is possible to achieve optimal photonic absorption in thinner active layers, which will lead to improved charge transport and higher efficiencies in OPVs. The proposed approach, thus, offers a potential solution towards the classic conflict between optical and electronic scales in OPVs. We do realize that it will not be straightforward to conformally deposit active layers on proposed textured surfaces, if processed from solution using techniques like spin-coating, which are more amenable to flat surfaces. Some tailoring and innovation would thus be required on the processing front for polymer based OPVs. However, our results are immediately applicable to small-molecule based OPVs that utilize thermal-evaporation for deposition for active layers. In addition, our approach can also have potential implications on the fields of photodetectors, photoelectrochemical systems, and the like.

2.7 Acknowledgements

We thank Iowa State University for start-up funds, Iowa Power Fund from the state of Iowa's Office of Energy Independence, and USDOE Ames Laboratory for seed funding. We also thank Dr. Jayeoun Kim and Dr. Kai-Ming Ho for helpful discussions.

2.8 References

[1] C. W. Tang, "Two-layer organic photovoltaic cell," Appl. Phys. Lett.**48**, 183-185 (1986).

[2] P. Peumans, A. Yakimov, S. Forrest, "Small molecular weight organic thin-film photodetectors and solar cells," J. Appl. Phys.**93**, 3693-3723 (2003).

[3] N. S. Sariciftci, D. Braun, C. Zhang, V. I. Srdanov, A. J. Heeger, G. Stucky, F. Wudl, "Semiconducting polymer-buckminsterfullerene heterojunctions: diodes, photodiodes, and photovoltaic cells," Appl. Phys. Lett.**62**, 585-587 (1993).

[4] G. Yu and A. J. Heeger, "Charge separation and photovoltaic conversion in polymer composites with internal donor/acceptor heterojunctions," J. Appl. Phys.**78**, 4510-4515 (1995).

[5] J. J. M. Halls, C. A. Walsh, N. C. Greenham, E. A. Marseglia, R. H. Friend, S. C. Moratti, A. B. Holmes, "Efficient photodiodes from interpenetrating polymer networks," Nature**376**, 498-500 (1995).

[6] G. Yu, J. Gao, J. C. Hummelen, F. Wudl, A. J. Heeger, "Polymer photovoltaic cells: enhanced efficiencies via a network of internal donor-acceptor heterojunctions," Science**270**, 1789-1791 (1995).

[7] W. L. Ma, C. Y. Yang, X. Gong, K. Lee, A. J. Heeger, "Thermally stable, efficient polymer solar cells with nanoscale control of the interpenetrating network morphology," Adv. Funct. Mater. **15**, 1617-1622 (2005).

[8] G. Li, V. Shrotriya, J. Huang, Y. Yao, T. Moriarty, K. Emery, Y. Yang, "High-efficiency solution processable polymer photovoltaic cells by self-organization of polymer blends," Nat. Mater. **4**, 864-868 (2005).

[9] R. J. Kline, M. D. McGehee, E. N. Kadnikova, J. Liu, J. M. J. Fréchet, "Controlling the field-effect mobility of regioregular polythiophene by changing the molecular weight," Adv. Mater. **15**, 1519-1522 (2003).

[10] M. Agrawal, P. Peumans, "Broadband optical absorption enhancement through coherent light trapping in thin-film photovoltaic cells," Opt. Express **16**, 5385-5396.

[11] P. Campbell and M. A. Green, "Light trapping properties of pyramidally textured surfaces," J. Appl. Phys. **62**, 243-249 (1987).

[12] C. Heine and R. H. Morf, "Submicrometer gratings for solar energy applications," Appl. Opt. **34**, 2476-2482 (1995).

[13] L. S. Roman, O. Inganäs, T. Granlund, T. Nyberg, M. Svensson, M. R. Andersson, J. C. Hummelen, "Trapping light in polymer photodiodes with soft embossed gratings," Adv. Mater. **12**, 189-195 (2000).

[14] M. Niggemann, M. Glatthaar, A. Gombert, A. Hinsch, V. Wittwer, "Diffraction gratings and buried nano-electrodes - architectures for organic solar cells," Thin Solid Films **451–452**, 619-623 (2004).

[15] L. A. A. Pettersson, L. S. Roman, O. Inganäs, "Modeling photocurrent action spectra of photovoltaic devices based on organic thin films," J. Appl. Phys. **86**, 487-496 (1999).

[16] F. C. Chen, J. L. Wu, C. L. Lee, W. C. Huang, H. M. P. Chen, W. C. Chen, "Flexible Polymer Photovoltaic Devices Prepared With Inverted Structures on Metal Foils," IEEE Electron Device Lett. **30 (7)**, 727-729 (2009).

[17] M. Glatthaar, M. Niggemann, B. Zimmermann, P. Lewer, M. Riede, A. Hinsch, J. Luther, "Organic solar cells using inverted layer sequence," Thin Solid Films **491**, 298-300 (2005).

[18] E. Lioudakis, A. Othonos, I. Alexandrou, Y. Hayashi, "Optical properties of conjugated poly(3-hexylthiophene)/[6,6]-phenylC_{61}-butyric acid methyl ester composites," J. Appl. Phys. **102**, 083104-1-5 (2007).

[19] L. A. A. Pettersson, F.Carlsson, O. Inganäs, H. Arwin, "Spectroscopic ellipsometry studies of the optical properties of doped poly(3,4-ethylenedioxythiophene): an anisotropic metal," Thin Solid Films **313-314**, 356-361 (1998).

[20] J. Bartella, J. Schroeder, K. Witting, "Characterization of ITO- and TiO_xN_y films by spectroscopic ellipsometry, spectraphotometry and XPS," Appl. Surf. Sci. **179**, 181-190 (2001).

[21] P. B. Johnson and R. W. Christy, "Optical constants of transition metals: Ti, V, Cr, Mn, Fe, Co, Ni, and Pd," Phys. Rev. B **9**, 5056-5070 (1974).

[22] D. W. Sievers, V. Shrotriya, Y. Yang, "Modeling optical effects and thickness dependent current in polymer bulk-heterojunction solar cells," J. Appl. Phys. **100**, 114509-1-7 (2006).

CHAPTER 3. On realizing higher efficiency polymer solar cells using a textured substrate platform[1]

Modified from a paper published in *Advanced Materials*

Kanwar S. Nalwa[2,3], Joong-Mok Park[4], Kai-Ming Ho[5], and Sumit Chaudhary[2,6]

3.1 Abstract

Textured substrate based light-trapping schemes are a commonplace in traditional inorganic photovoltaic (PV) cells. However, they have not been successfully applied to polymer based PVs due to an obvious problem of solution-processing nanoscale thick and conformal PV layers on (sub) microscale topographies. In this report, we show that realization of such conformal coatings is indeed possible, if the underlying topography has suitable dimensions. We fabricated poly(3-hexylthiophene): [6,6]-phenyl-C61-butyric acid methyl ester (P3HT:PCBM) based bulk-heterojunction PV cells on grating-type textured substrates possessing several submicron and micron scale topographical dimensions. We discovered that if the height of the underlying topographical features is reduced to sub-micron regime (e.g. 300 nm) and the pitch is increased to more than a micron (e.g. 2 μm), the textured surface becomes amenable to coating a conformal PV active-layer. The resultant PV cells showed 100% increase in average light absorption near the band edge due to trapping of higher wavelength photons, and 20% improvement in power conversion

[1] K. S. Nalwa, J. M. Park, K. M. Ho, and S. Chaudhary, \On realizing higher efficiencypolymer solar cells on a textured substrate platform",*Advanced Materials*, **23**, 112-116, 2011. Copyright Wiley-VCH Verlag GmbH & Co. KGaA. Reproduced with permission.
[2] Graduate student and Assistant Professor, respectively, Department of Electrical and Computer Engineering, Iowa State University.
[3] Primary researcher and author.
[4] Post-doctoral researcher, Ames Laboratory-USDOE & Department of Physics and Astronomy
[5] Professor, Ames Laboratory-USDOE & Department of Physics and Astronomy
[6] Author for correspondence

efficiency as compared with the flat PV cell. We also discuss the fate of processing the active-layer on textured substrates with unsuitable topographical dimensions.

3.2 Introduction

Organic photovoltaic (OPV) technology is an attractive solar-electric conversion paradigm due to the promise of low cost roll-to-roll production and amenability to flexible substrates. Substantial progress has been made over the last 5 years, by virtue of optimization of materials processing parameters [1-3] and emergence of new conjugated polymers with tailored energy levels [4-6]. Power conversion efficiency (PCE) exceeding 7% has recently been achieved [4]. The state-of-the-art devices are so called bulk-heterojunction (BHJ) type in which the PV active-layer is coated from a blend of donor and acceptor species. The nanoscale nature of phase separation between the donors and acceptors in a BHJ active-layer alleviates the mismatch between exciton diffusion length (~10 nm) and optical absorption length (> 100 nm). However, there still exists a mismatch between optical absorption length and charge transport scale. BHJ active-layers tend to suffer from cul-de-sacs in the charge transport pathways, and hole mobilities in conjugated polymers remain low. Both of these factors lead to recombination losses, higher series resistances and lower fill-factors [7]. Thus, it is imperative to develop fabrication methodologies that can enable efficient optical absorption in films thinner than optical absorption length. The most desirable methodology would be one which can also substantially improve absorption at the band edge of conjugated polymers, which usually lies in the red/near-infra-red region, and where significant amount of solar flux is also located. It is more so important because the charge carriers photoexcited at the band edge

were found to have a higher dissociation efficiency than the ones excited at higher energies [8]. Textured substrate based light-trapping schemes are a commonplace in traditional inorganic photovoltaic (PV) cells. However, they have not been successfully applied to polymer based PVs due to an obvious problem of solution-processing nanoscale thick and conformal PV layers on topographical surfaces. In this communication, we show that realization of such conformal layers is indeed possible, if the underlying topography has suitable dimensions. We fabricated poly(3-hexylthiophene): [6,6]-phenyl-C61-butyric acid methyl ester (P3HT:PCBM) based BHJ PV cells on grating-type textured substrates possessing several submicron and micron scale topographical dimensions. We discovered that if the height of the underlying topographical features is reduced to sub-micron regime (e.g. 300 nm) and the pitch is increased to more than a micron (e.g. 2 μm), the textured surface becomes amenable to coating a conformal PV active-layer. The resultant PV cells showed 100% increase in average light absorption near the band edge due to trapping of higher wavelength photons, and 20% improvement in PCE as compared with the flat PV cell.

Till date, a few light management techniques in ray optics regime have been investigated for enhancement of optical absorption in OPVs, namely, collector mirrors [9], and a macroscale configuration in which two OPV cells were mounted together in V-shape [10]. Light-trapping schemes based on periodic patterning were also reported using buried nanoelectrodes [11], microprism substrates [12], and azopolymer based submicron topography substrate [13]. Although enhancement in optical absorption was demonstrated in these patterning schemes, efficient OPV cells could not be realized due to processing bottlenecks. Another type of light management approach reported was embossing of active-

layer to induce a sub-micron scale texture on an otherwise flat film [14-16]. Although the embossing approach did lead to improvement in PCE of OPV cells, the approach suffers from some drawbacks. Firstly, embossing is done at an elevated temperature. Such an annealing step is not universally desirable for all BHJ materials and can lead to degradation [6]. Secondly, the embossing step poses contamination concerns, which can lead to Schottky barrier formation at the organic/metal interface [17]. Lastly and most importantly, embossing produces alternating thick and thin regions within the PV active-layer, which is not the most optimal configuration from the point of view of charge transport,as the thicker regions are still bound to suffer from recombination losses. In this respect, we believe that a nanoscale thick active-layer uniformly or conformally coated on an underlying textured substrate (electrode) is a more promising light management paradigm than embossing. Besides light management, a textured PV cell can also enable an additional functionality of self-cleaning, which requires nanoscale roughness for super-hydrophobicity [18]. Such a textured substrate paradigm, however, has not been successful in polymer based PVs due to an obvious challenge of processing such conformal films from solution. Attempts to spin-coat PV active-layer on textured substrates led to over filling of the valleys and shunts at the crests [11,12], which severely affected the device performance. Thus, the issue of design of textured substrates for light-trapping in polymer PVs, should not solely be approached from the point of view of discovering the best optical design. Instead, we argue that an equally critical question to ask is: Which design is most amenable for realizing a conformal active-layer film from solution processing?

3.3 Experimental Details

Photoresist gratings were made by laser interference holography with Lloyd's mirror setup on ITO coated glass slides. AZ-hir 1075 PR was spin coated on pre-cleaned ITO substrates (5-15 Ω/□. Delta Technologies), prebaked in oven at 60^{o}C for 30 minutes, exposed by sinusoidal interference patterns made with Ar laser (λ =364 nm), and then post baked at 110^{o}C for 1 minute. It was then developed in MIF 300 developer for 1 minute followed by a rinse in distilled water. The period of pattern was changed by changing the angle of incidence, and height was changed by changing spin coating parameters. Although these PR gratings were made on ITO substrates, but to have better electrical connectivity of the photo active-layer with bottom ITO electrode, 120 nm ITO was sputtered on these PR gratings at 20 W RF power in Argon at room temperature (see appendix for the reason behind choosing 120 nm thickness of sputtered ITO). Same thickness of ITO (120 nm) was sputtered on the commercial ITO coated glass slides to fabricate flat PV cells, for the sake of controlled comparisonwith the grating PV cells. The following procedure was kept same for the fabrication of flat and grating PV cells. A hole conducting film of PEDOT:PSS (CLEVIOS P VP AI 4083) was spin coated at 3000 rpm after treating the sputtered ITO layer with air plasma. The films were annealed at 120˚C for 10 minutes. The samples were then transferred inside the Ar atmosphere glove box. The P3HT:PCBM blend with 1:1 weight ratio was used. P3HT concentration was 17 mg/ml in dichlorobenzene. The blend active-layer was spin coated at 600 rpm for 60 s. After spin coating, the samples were allowed to dry slowly under a petri dish. Finally, Al (100 nm) electrode was deposited in a vacuum evaporator. I-V characterization was done using ELH Quartzline halogen lamp, the intensity of which was calibrated using a crystalline Si cell with a KG-5 filter. EQE

measurements were also done using this lamp anda monochromator with a lock-in amplifier to eliminate background noise. The reference was a calibrated Si photodiode with known EQE spectra. Reflection measurements were performed using ocean optics setup with an integrating sphere.

3.4 Results and discussion

In this communication, we demonstrate that it is indeed possible to realize a uniformly thick and conformal polymer film on textured substrates if the topographical dimensions are suitable (sub-micron height and greater than micron pitch). Efficient P3HT:PCBM based BHJ PVs were realized on these substrates. Optical absorption was enhanced almost throughout the absorption band. Especially at the band edge which we define as the region between 600 nm – 700 nm wavelength for P3HT, average optical absorption increased by 100%. Overall power conversion efficiency of the PV cells increased by 20% as compared with the control flat cell. In this study, spin-coating was used for depositing the active-layer. However, the so called suitable topographical dimensions discovered should be equally relevant for realizing conformal coatings using other roll-to-roll techniques like gravure coating.

Figure 3.1 shows the schematic of our textured substrate based devices. For this study, we used laser interference lithography to pattern photoresist (PR) in a one-dimensional diffraction grating pattern (see appendix for fabrication details). In principle, one can also make a two-dimensional pattern, and use other soft-lithography [23] or self-assembly [24] based approaches to realize a textured substrate. In our devices (Figure 3.1),

light is incident through the substrate and traverses through the photoactive-layer followed by encounter with the inverted Al cathode grating. The Al cathode grating leads to scattering of light along the plane dimension and increases the light travelling path inside the active-layer, providing enhanced absorption. Figure 3.1 is just a representative of the sequence of layers in our devices. Exact topography of active-layer on the PR grating is obviously a strong function of the pitch (period) and height of the grating pattern.

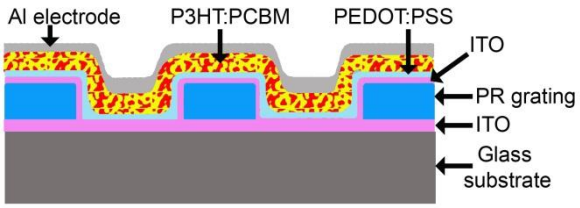

Figure 3.1:Schematic of the textured substrate based P3HT:PCBM solar cell.

To evaluate the feasibility of achieving our proposed conformal layer, we investigated several topographical dimensions for our PR grating. Figure 3.2 shows the fate of spin-coating P3HT:PCBM active-layer on the PR grating of several dimensions. For microscale patterns, where both pitch and height of the PR grating structure are greater than 1 µm, the active-layer was highly non-conformal [Figure 3.2(a-c)]. There was excess polymer in the valleys and less on the crests, including polymer-less regions at the corners that are expected to cause shunts in the final device, similar to previous reports [12,14]. Several air-gaps were also observed within the polymer film inside the valleys. Even after tailoring various spin coating parameters, conformal polymer coating could not be achieved. Intuitively, one can hypothesize that it is microscale height of the PR grating that led to the case of underfill and air-gaps for these samples. Thus, we resorted to PR gratings with sub-micron heights. We chose 300 nm as an exemplary sub-micron dimension for the

height. For pitch, we chose several dimensions – 600 nm, 800 nm, and 1 μm. Figure 3.2(d-f) show the fate of spin coating polymer film on the PR grating of 300 nm height and 600 nm pitch. Quality of the polymer film improved as compared with the case of microscale height and pitch. No shunt points or air-gaps were observed. However, the film was still not conformal to the underlying topography. Valleys had more polymer than the crests, which we call the case of overfill. This excess polymer in the valleys can be expected to lead to recombination losses and poor performance. Similar overfill case was observed for the PR

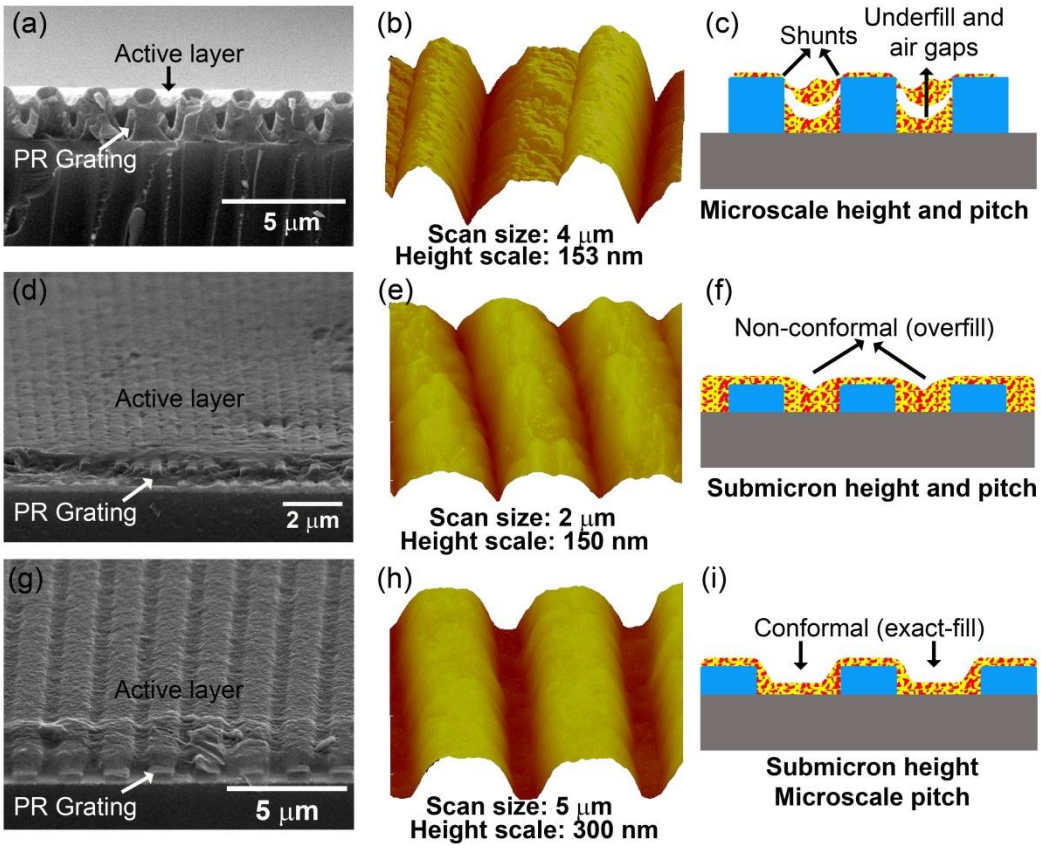

Figure 3.2: SEM (left), AFM (middle), and schematic (right) of P3HT:PCBM active-layer spin-coated on PR grating substrates of: (a-c) 2 μm pitch and 2 μm height; (d-f) 600 nm pitch and 300 nm height; and (g-i) 2 μm pitch and 300 nm height. Indium tin oxide was sputtered and PEDOT:PSS was spin-coated before spin-coating the active-layer.

grating of 800 nm pitch and 1μm pitch (see appendix for SEM and AFM images). However, a clear trend in the morphology was observed as the pitch increased from 600 nm to 1 μm, with amount of overfilling reducing as pitch increased. As a logical next step, we decided to increase the pitch of the PR grating to 2 μm while keeping height at 300 nm. As the SEM, AFM and schematic images of Figure 3.2(g-i) reveal, these dimensions indeed enabled the realization of a uniformly thick P3HT:PCBM film that conformally followed the topography of the substrate. Thickness of the active-layer inside the valleys was identical to the thickness on the crests, as evident by the AFM height scale of 300 nm [Figure 3.2(h)]. Also, no shunt-like defects were observed.

To investigate the effect of texturing on the final devices, we characterized our OPV devices based on the aforementioned textured substrates, along with a flat control. Figure 3.3 shows the current-voltage (I-V) characteristics of our devices. Results of devices fabricated on the microscale topography (2 μm pitch and 2 μm height) are not shown as the device failed to show PV behavior due to large number of shunts discussed above. Figure 3.3 shows that the conformal coating of P3HT:PCBM on the 2 μm pitch and 300 nm height substrate led to 20% increase in short circuit current density (J_{sc}) as compared with the flat control. PCE also increased by 20% since the open circuit voltage (V_{oc}) and fill-factor (FF) were not affected. V_{oc} and FF not being affected is another signature of the conformal nature of active-layer coating, because excess polymer in the grating valleys and/or shunts would have had a direct negative impact on both V_{oc} and FF. On the other hand, the overfill case of smaller pitches discussed above led to greater recombination losses in the active-layer aggregated in the valleys of the grating and the performance of the PV cells degraded

in all respects (J_{sc}, V_{oc} and FF) as compared with the flat control. See appendix for dark I-V characteristics and more discussion on V_{oc}.

In order to elucidate the light trapping behavior of our textured device platform, we did external quantum efficiency (EQE) and reflection measurements on our highest efficiency grating cell (300 nm height and 2 μm pitch) and the reference flat cell. Optical

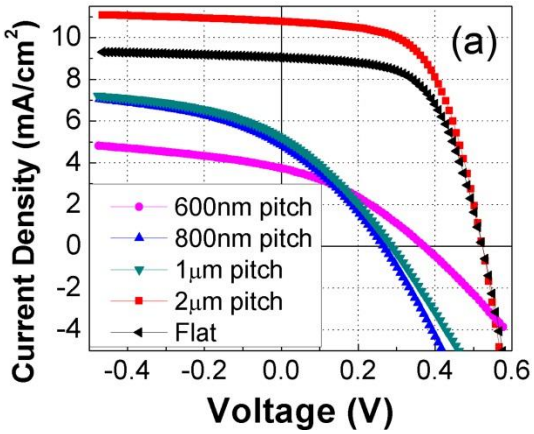

Figure 3.3: Photocurrent dependence on pitch of the 300 nm height grating cells and the reference flat cell.

microscopy image in Figure 3.4(a) depicts a visual signature of light diffraction phenomenon at play in our grating devices. Figure 3.4(b) shows the total (sum of zeroth and higher order) and scattered (higher order excluding zeroth order) reflection measured at normal incidence. Total reflection is greatly suppressed in the case of the grating PV cell. Total reflection measurements also show significant interference oscillations that appear in flat cells, while the grating cells show relatively flat smoother reflection in the range of 400-600 nm. The observed oscillations in the flat cell are basically Fabry-Perot interferences, arising from the incompletely absorbed incident light inside the active-layer interfering with the reflected light from the glass side of the device. The interference oscillations are reduced in the grating cell, suggesting that very little light escapes after

reflection from the Al. This corroborates the light trapping nature of the grating structure. As a result of negligible transmission, the reflection (R) yields an approximation to the absorption (A) using A= 100-R. For wavelengths longer than 550 nm, there is a much stronger absorption in the grating cell as evident from the reduced reflection [Figure 3.4(a)]. Specifically, at λ= 600 nm, the absorption in the grating cell is enhanced by 2.5 times as compared with the planar cell.

Figure 3.4(c) shows the EQE measurement of the grating cell and the flat cell. The grating cell exhibits substantial enhancement in EQE over the flat cell at wavelengths greater than 550 nm. This observation is supported by significant scattered (higher order) reflection from the grating cell for λ > 550 nm [Figure 4(b)]. Due to the periodic structure of the Al cathode, incident light reaching it can be diffracted backward according to the following equation:

$$m\lambda = n_{\text{active}} p(\sin\theta_i + \sin\theta_d) \quad (1)$$

where m is the diffraction order, λ is the wavelength of incident light, n_{active} is the refractive index of the active-layer, p is the period of grating, and θ_i and θ_d are incidence and diffraction angles, respectively. A constant n_{active} was considered as 2 in the spectral wavelength range between 300 and 700 nm for simplification [25]. Then, in the case of normal incidence, for 600 nm<λ<700 nm, m can take values of 0, ±1, ±2, ±3, ±4, ±5and ±6, because sin $\theta_d \leq 1$ and p = 2 μm. Due to the higher order diffractions and their large diffraction angles in the grating cells, the zeroth order reflection intensity was reduced as was the total reflection. Therefore the optical path length is increased considerably and absorption in enhanced. For the short wavelength region (below 500 nm) where the extinction coefficient of P3HT:PCBM is high, all the light loss can be attributed to light

reflection since its absorption length (~200 nm) is greater than the active-layer thickness of ~ 150 nm. Therefore, the enhancement of EQE [Figure 3.4(c)] at short wavelengths (420-500 nm) is imputed by the reduced reflection of the grating cell in this wavelength range. The lowering of reflection is the result of path length increment of the back-scattered light from Al cathode inside the photoactive-layer. The above argument is supported by a distinct peak in the reflection ratio curve for wavelengths range 400-500 nm [Figure 3.4(d)].

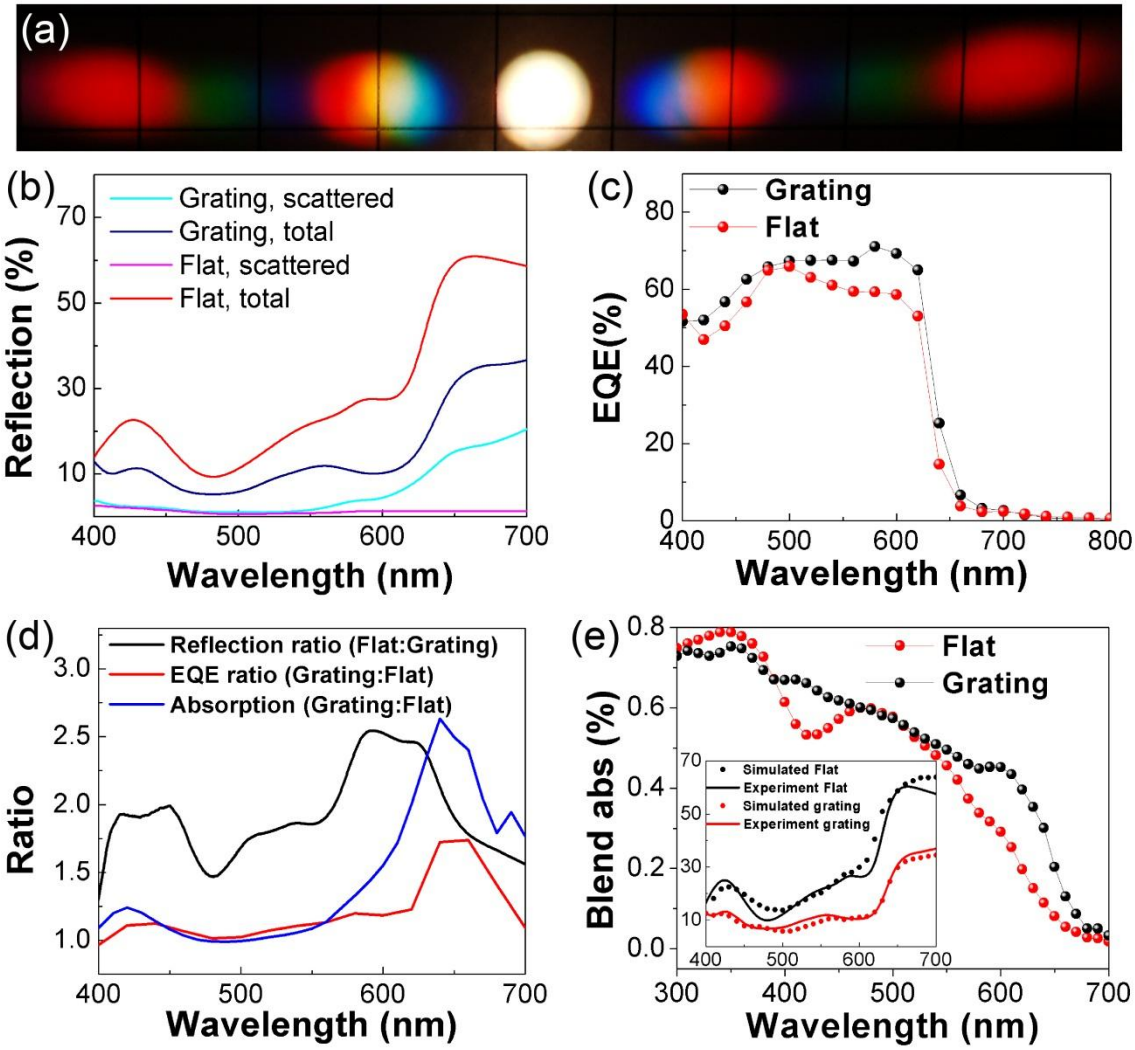

Figure 3.4: (a) Optical micrograph showing the spots of different diffraction modes when incident white light on the grating cell is reflected and diffracted back from the Al cathode. (b-e) For the 2

μm pitch - 300 nm height grating cell and the planar cell: (b) Total and scattered reflection measured at normal incidence; (c) EQE; (d) Reflection, simulated absorption and EQE ratios versus wavelength; and (e) Simulated active-layer absorption averaged over TE and TM polarizations. Inset shows polarization averaged experimental and simulated total reflection for the planar and the 300 nm height and 2 μm pitch grating cells.

To further reconcile this effect, more precise determination of the absorption is required. The aforementioned approximation of A=100-R is a measure of total absorption where losses in all internal layers are included. Relative to the planar cell, the optical absorption in each internal layer is altered by the grating due to its corrugated structure. This will also cause changes in the electromagnetic field in layers that absorb light but do not produce photocurrent, such as ITO and PEDOT:PSS. Hence, only a first approximation to the photoactive absorption is achieved by comparing reflection. Therefore, optical absorption was individually quantified in all the layers by solving electromagnetic wave equations on the entire defined geometry. For the planar cells, simulations can be performed using optical models based on 1D-transfer matrix formalism for normal light incidence. This approach however is not suitable for the optical modeling of the grating cells, since the grating pitch is of the order of wavelength of light, leading to complex diffraction and interference effects that have to be included in the model. Finite element model inbuilt in COMSOL MULTIPHYSICS was used to perform the simulations, accounting for the two-dimensional geometry and wavelength dependence of dielectric functions for materials. The physical dimensions of the grating cell used for simulations were obtained from measured SEM values. A good fit between the measured and the simulated total reflection at normal incidence is obtained forthe 300 nm height and 2 μm pitch grating cells and planar cells, as shown in inset of Figure 3.4(e). The model is used to calculate absorption in the P3HT:PCBM active-layer. Polarization averaged active-layer

absorption is plotted for both the grating and the planar cells in Figure 3.4(e). In the visible range, the polarization averaged absorption in the active-layerfor the grating and the planar case is similar, except in the 400 nm to 450 nm regime, where the grating geometry shows higher absorption. However, the most significant absorption improvement using the grating geometry is obtained in the wavelength range of 600-700 nm. P3HT has a band edge at ~600 nm and the absorption coefficient rapidly drops for light wavelengths above 600 nm. Specifically, a 2.6-fold absorption enhancement is achieved at λ= 640 nm for the 300 nm height and 2 μm pitch grating cell, relative to the planar one. This conduces to an average 100% increase in absorption near the band edge ($600 \leq \lambda \leq 700$ nm). These data suggest that textured geometry of grating cells can significantly enhance light trapping, even for the absorption of photons below the band gap. Figure 3.4(d) further confirms the argument that improvement in EQE and absorption is owing to light trapping effect, as it shows that the wavelengths at which the reflection from the grating is suppressed as compared to the flat (i.e. peaks in the reflectance ratio) correspond to the peaks of the EQE enhancement ratio. Furthermore, simulated blend absorption ratio follows the same trend as EQE ratio vs. wavelength [Figure 3.4(d)], confirming that the increment in EQE is pertaining to optical effects rather than increased area or other electrical enhancements (such as excitonic dissociation, electric field between electrodes, charge transport etc.).

For solar cells in a practical environment where sunlight can be quite diffused, it is also important to evaluate the absorption over a wide range of incident angles [26]. The grating based devices also showed advantage over the flat devices at higher incident angles of light (see appendix).

3.5 Conclusions

In conclusions, we show that for submicron height topographies, it is possible to coat a conformal polymer film from solution if the pitch of the topography is few times higher, that is, larger than a micron. Realizing polymer PV cells on such topographies provides an efficient way to achieve light-trapping without compromising with electrical characteristics. Such P3HT:PCBM cells fabricated on our study showed 20% improvement in PCE relative to the flat control, owing to broadband light-trapping, especially at the band-edge where 100% average absorption increase was observed. Although we used spin-coating for the deposition of PV active-layer, but amenable topographical dimensions discovered in this study should also be relevant for implementing this light-management scheme using roll-to-roll coating techniques like gravure coating, upon some adaptation. An example of adaptation can be lateral acceleration and/or inversion of substrate upon the application of polymer solution. This can provide an external stimulus similar to what centrifugal force provides in the spin-coating process to enable the flow of solution over textured topographies and realization of conformal coatings.

3.6 Acknowledgements

KS and SC thank Iowa Power Fund and Ames Laboratory seed funding for financial support. JMP and KMH thank Director for Energy Research, Office of Basic Energy Sciences. The Ames Laboratory is operated for the US Department of Energy by Iowa State University under contract no. DE-AC02-07CH11358.

3.7 Appendix

(a) Optimization of sputtered ITO thickness

ITO was sputtered on top of PR gratings to provide path for hole collection and extraction, from the active-layer to the bottom ITO electrode. Figure 3.5(a) shows photocurrent vs. voltage curves of grating based solar cell with 600 nm pitch and 200 nm height having different sputtered ITO (S-ITO) thicknesses. Device without sputtered ITO exhibited least short circuit current density due to poor charge collection as a result of longer charge transport path way, contributing to recombination losses. On sputtering 120 nm S-ITO, the device series resistance decreased due to the formation of continuous conductive pathway of S-ITO, for better hole transport from active-layer to the underlying ITO anode, thus mitigating electrical losses. However on depositing 200 nm S-ITO, optical absorption increased in the S-ITO layer and hence the photon flux reaching the active-layer is significantly reduced, imparting lower short current density to the device as compared to the device with 120 nm S-ITO. The above observation is also suggested by lowering of

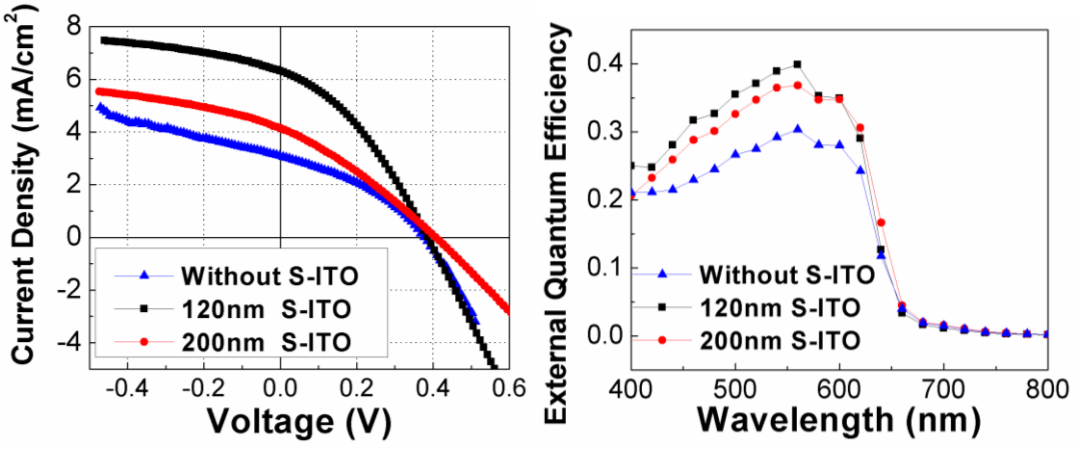

(a) (b)

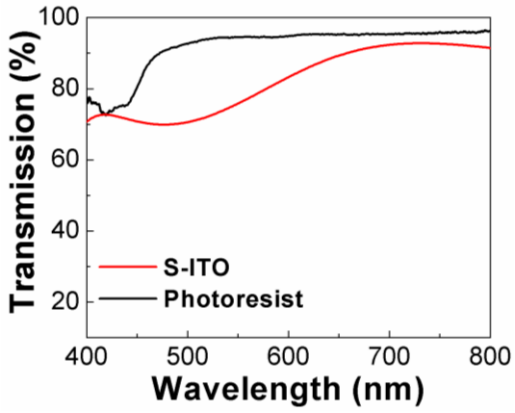

(c)

Figure 3.5: ITO thickness optimization. (a) Current density vs. voltage plots and (b) External quantum efficiency vs. wavelength of 600 nm pitch - 300 nm height PR solar cell devices, on varying S-ITO thickness. (c) Transmission spectra of 200 nm thick S-ITO and 300 nm thick PR film.

device's EQE on increasing the S-ITO thickness from 120 to 200 nm, in the range 400-600 nm [Figure 3.5(b)], where S-ITO is more absorbing [Figure 3.5(c)]. Therefore 120 nm thick S-ITO was found to be electrically as well as optically optimal for the PR gratings.

(b) SEM and AFM images of P3HT:PCBM active-layer on PR grating substrate of 1 µm and 800 nm pitch with 300 nm height.

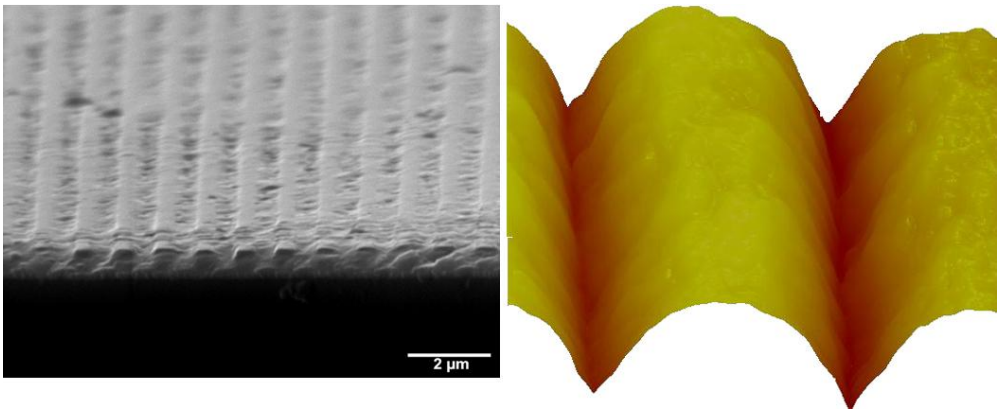

(a) (b)

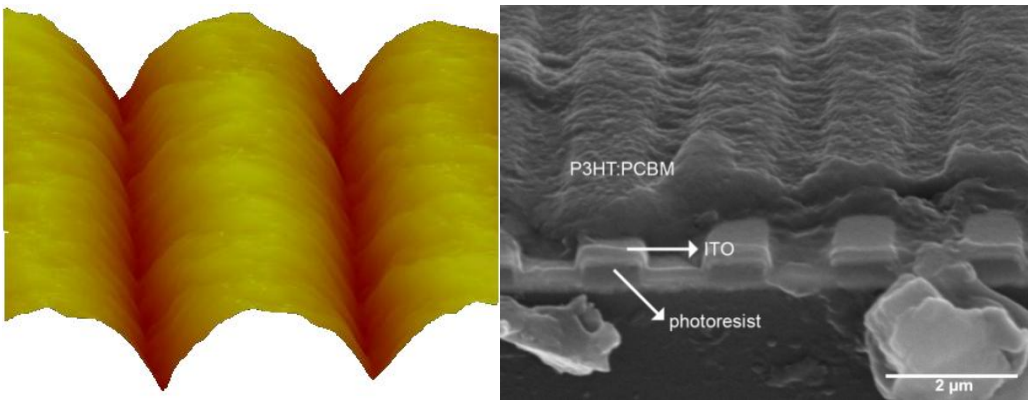

(c) (d)

Figure 3.6: (a) SEM image of 300 nm height and 1 µm pitch grating substrate coated with P3HT:PCBM layer. AFM images of (b) 1 µm and (c) 800 nm pitch grating substrate (300 nm height) coated with active layer. Scan size of AFM image is 2 µm and height scale is 150 nm. As the height scale of AFM image quantitatively indicates, case of overfill was observed for 800 nm and 1 µm pitch substrates similar to the case of 600 nm pitch substrate discussed in the main body of this paper. (d) High resolution cross-sectional SEM image of 300 nm height and 2 µm pitch cell showing conformal ITO layer between P3HT:PCBM layer and photoresist grating. PEDOT:PSS layer could not be clearly identified.

(c) Dark I-V characteristics of textured PV cells

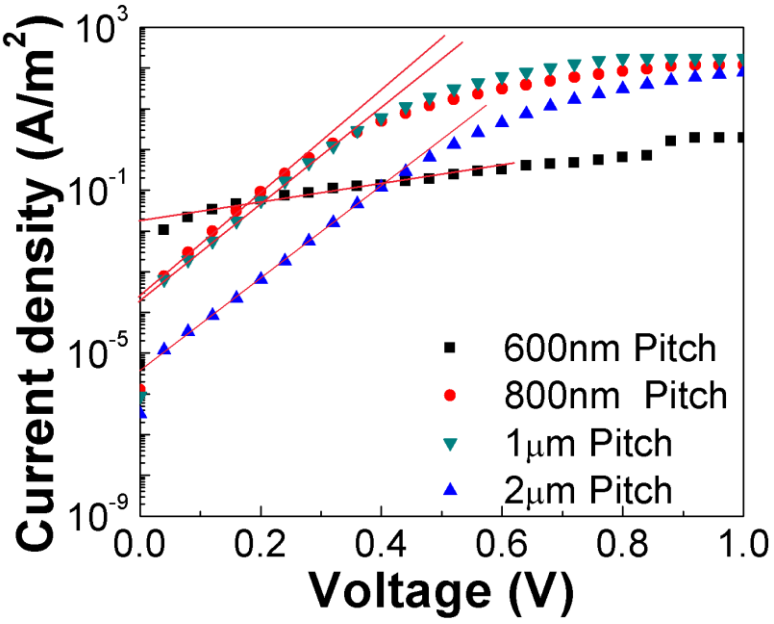

Figure 3.7: Effect of pitch size on the dark current of 300 nm height grating-based cells at positive bias. The red line represents exponential fits, allowing the determination of reverse saturation

current (J_s). V_{oc} is given by $V_{oc} = \frac{nkT}{q}\ln\left(\frac{J_{sc}}{J_s}+1\right)$, where n is diode ideality factor, k is Boltzmann constant, T is temperature, q is electronic charge, J_{sc} is short circuit current, and J_s is reverse saturation current. Least reverse saturation current of 2 µm pitch cell corresponds to its highest V_{oc} among all grating cells. Among the other three pitches, the trend in J_s does not match the trend in V_{oc} due to a higher n of the 600 nm pitch device as visible from the current-voltage characteristics under illumination. The reason for higher n of 600 nm pitch device is not yet clear.

(d) Angular dependence of reflection 2 µm pitch - 300 nm height grating cell and the flat cell

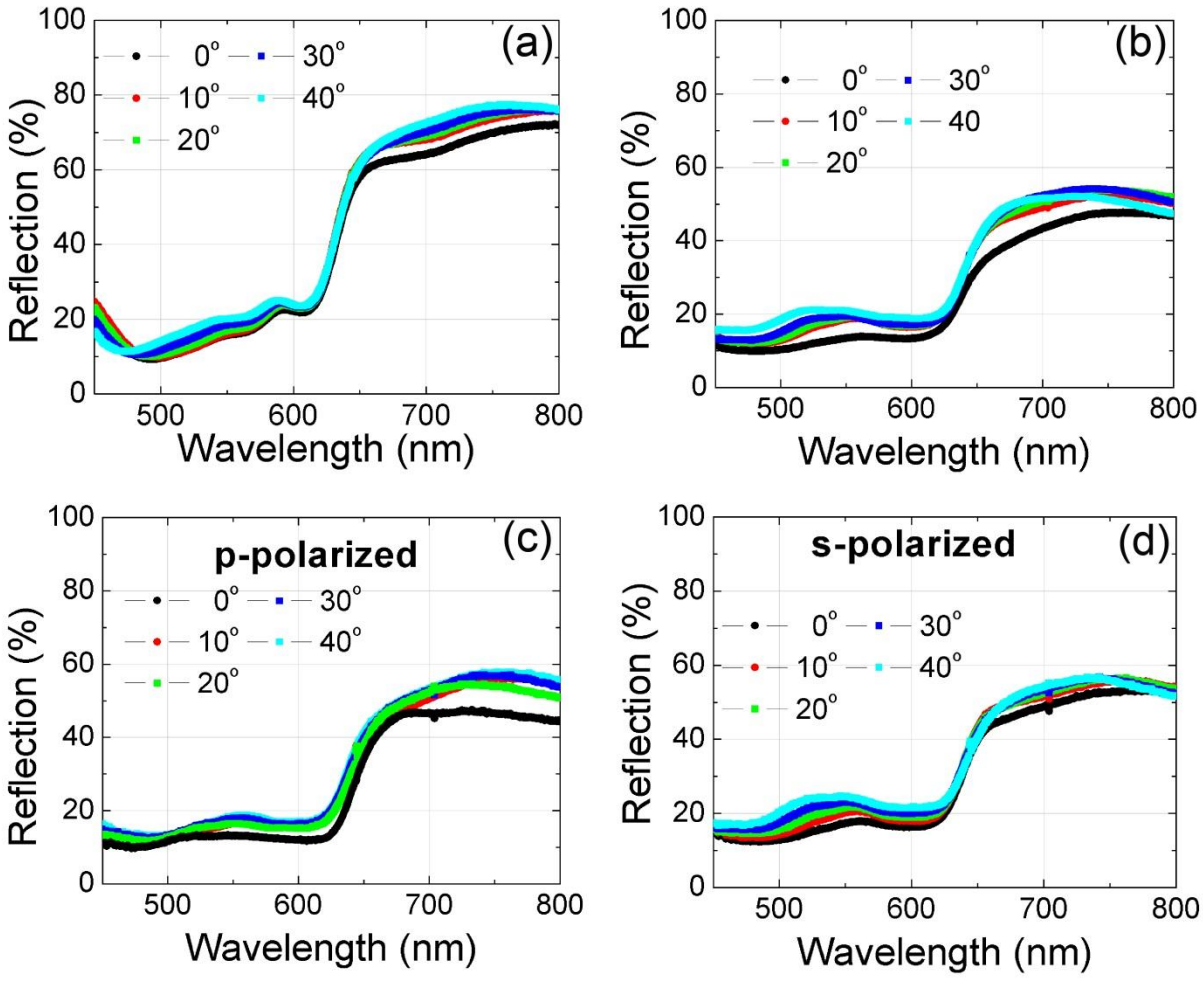

Figure 3.8: Angle dependent unpolarized total (sum of zeroth and higher order) reflection for the (a) flat and (b) 2 µm pitch - 300 nm height grating cells. Variation of (c) p-polarized (parallel to

grating) and (d) s-polarized (perpendicular to grating) total reflection with incident angle for the 2 μm pitch - 300 nm height grating cell.

Figures 3.8 reveals that 2 μm pitch - 300 nm height grating cell has an advantage over flat cell in terms of absorbed light, even at higher incident angles. On increasing the incident angle, the total reflection from the grating cell only slightly increased in the wavelength regime of 500-600 nm [Figure 3.8(b)] and this contribution came primarily from the s-polarized reflection [Figure 3.8(d)]. P-polarized reflection [Figure 3.8(c)] did not vary significantly with the incident angle in the 400-600 nm absorption range of P3HT:PCBM blend.

3.8 References

[1] Li, G.; Shrotriya, V.; Huang, J. S.; Yao, Y.; Moriarty, T.; Emery, K.; Yang, Y. *Nature Materials***2005**, *4*, 864.

[2] Peet, J.; Kim, J. Y.; Coates, N. E.; Ma, W. L.; Moses, D.; Heeger, A. J.; Bazan, G. C. *Nature Materials***2007**, *6*, 497.

[3] Ma, W. L.; Yang, C. Y.; Gong, X.; Lee, K.; Heeger, A. J. *Advanced Functional Materials***2005**, *15*, S1617.

[4] Yongye, L.; Zheng, X.; Jiangbin, X.; Szu-Ting, T.; Yue, W.; Gang, L.; Claire, R.; Luping, Y. *Advanced Materials***2010**, *22*, E135.

[5] Chen, H. Y.; Hou, J. H.; Zhang, S. Q.; Liang, Y. Y.; Yang, G. W.; Yang, Y.; Yu, L. P.; Wu, Y.; Li, G. *Nature Photonics***2009**, *3*, 649.

[6] Park, S. H.; Roy, A.; Beaupre, S.; Cho, S.; Coates, N.; Moon, J. S.; Moses, D.; Leclerc, M.; Lee, K.; Heeger, A. J. *Nature Photonics***2009**, *3*, 297.

[7] Halls, J. J. M.; Walsh, C. A.; Greenham, N. C.; Marseglia, E. A.; Friend, R. H.; Moratti, S. C.; Holmes, A. B. *Nature***1995**, *376*, 498.

[8] Yu, G.; Gao, J.; Hummelen, J. C.; Wudl, F.; Heeger, A. J. *Science***1995**, *270*, 1789.

[9] Kim, J. Y.; Kim, S. H.; Lee, H. H.; Lee, K.; Ma, W. L.; Gong, X.; Heeger, A. J. *Advanced Materials***2006**, *18*, 572.

[10] Shah, H.; Mohite, A.; Bansal, T.; Alphenaar, B. In *The American Physical Society March Meeting 2010* Portland, Oregon; Vol. 55.

[11] Peumans, P.; Bulovic, V.; Forrest, S. R. *Appl Phys Lett***2000**, *76*, 2650.

[12] Niggemann, M.; Glatthaar, M.; Lewer, P.; Muller, C.; Wagner, J.; Gombert, A. *Thin Solid Films***2006**, *511*, 628.

[13] Rim, S. B.; Zhao, S.; Scully, S. R.; McGehee, M. D.; Peumans, P. *Appl Phys Lett***2007**, *91*.

[14] Niggemann, M.; Glatthaar, M.; Gombert, A.; Hinsch, A.; Wittwer, V. *Thin Solid Films***2004**, *451-52*, 619.

[15] Cocoyer, C.; Rocha, L.; Fiorini-Debuisschert, C.; Sicot, L.; Vaufrey, D.; Sentein, C.; Geffroy, B.; Raimond, P. *Thin Solid Films***2006**, *511*, 517.

[16] Roman, L. S.; Inganas, O.; Granlund, T.; Nyberg, T.; Svensson, M.; Andersson, M. R.; Hummelen, J. C. *Advanced Materials***2000**, *12*, 189.

[17] Na, S. I.; Kim, S. S.; Jo, J.; Oh, S. H.; Kim, J.; Kim, D. Y. *Advanced Functional Materials***2008**, *18*, 3956.

[18] Ko, D. H.; Tumbleston, J. R.; Zhang, L.; Williams, S.; DeSimone, J. M.; Lopez, R.; Samulski, E. T. *Nano Letters***2009**, *9*, 2742.

[19] Garcia-Belmonte, G.; Munar, A.; Barea, E. M.; Bisquert, J.; Ugarte, I.; Pacios, R. *Organic Electronics***2008**, *9*, 847.

[20] Zhu, J.; Hsu, C. M.; Yu, Z. F.; Fan, S. H.; Cui, Y. *Nano Letters***2010**, *10*, 1979.

[21] Cocoyer, C.; Rocha, L.; Sicot, L.; Geffroy, B.; de Bettignies, R.; Sentein, C.; Fiorini-Debuisschert, C.; Raimond, P. *Appl Phys Lett***2006**, *88*, 133108.

[22] Niggemann, M.; Riede, M.; Gombert, A.; Leo, K. *Physica Status Solidi a-Applications and Materials Science***2008**, *205*, 2862.

[23] Lee, J. H.; Kim, C. H.; Ho, K. M.; Constant, K. *Advanced Materials***2005**, *17*, 2481.

[24] Koo, W. H.; Jeong, S. M.; Araoka, F.; Ishikawa, K.; Nishimura, S.; Toyooka, T.; Takezoe, H. *Nature Photonics***2010**, *4*, 222.

[25] Monestier, F.; Simon, J. J.; Torchio, P.; Escoubas, L.; Florya, F.; Bailly, S.; de Bettignies, R.; Guillerez, S.; Defranoux, C. *Solar Energy Materials and Solar Cells***2007**, *91*, 405.

[26] Nalwa, K. S.; Chaudhary, S. *Optics Express***2010**, *18*, 5168.

CHAPTER 4. Polythiophene-fullerene based photodetectors: Tuning of spectral response and application in photoluminescence based (bio)chemical sensors[1]

Modified from a paper published in *Advanced Materials*

Kanwar S. Nalwa[2,3], Yuankun Cai[4], Aaron L. Thoeming[2], Joseph Shinar[5], Ruth Shinar[6,7], and Sumit Chaudhary[7,8]

4.1 Abstract

We report for the first time, a photoluminescence (PL) based oxygen sensor utilizing inorganic or organic light emitting diode as the light source, and a poly(3-hexylthiophene):fullerene bulk-heterojunction type devices as the photodetectors, for both intensity and decay-time based detection of the sensing element's PL. The sensing element is based on the oxygen-sensitive dye Pt-octaethylporphyrin (PL peak ~ 640 nm) embedded in a polystyrene matrix. The PL of the dye is quenched by the presence of oxygen and the PL decay time is reduced. The active-layer of the photodetectors was processed for higher thicknesses and crystallinity under solvent annealing atmosphere - such that the external quantum efficiency in the red region exceeds that of the green region, and is as high as 50% at 640 nm, which is the peak of the dye's PL. Our study paves the way for the realization of compact, flexible and structurally integrated all-organic chemical sensors.

---

[1] K. S. Nalwa, Y. Cai, A. L. Thoeming, J. Shinar, R. Shinar, and S. Chaudhary, "Polythiophene-fullerene based photodetectors: tuning of spectral response and application in photoluminescence based bio(chemical) sensors", *Advanced Materials*, **22**, 4157-4161, 2010.

[2] Graduate student, Department of Electrical and Computer Engineering, Iowa State University.

[3] Primary researcher and author.

[4] Graduate Student, Department of Physics and Astronomy, Iowa State University.

[5] Professor, Ames Laboratory-USDOE & Department of Physics and Astronomy, Iowa State University.

[6] Adjunct Professor, Department of Electrical and Computer Engineering, Iowa State University.

[7] Author for correspondence

[8] Assistant Professor, Department of Electrical and Computer Engineering, Iowa State University.

4.2 Introduction

Organic electronics is attracting extensive interest in the development of low-cost and flexible devices, such as solar cells [1], light-emitting diodes (LEDs) [2], and photodetectors [3]. Recently, the use of organic electronics has been broadened toward novel devices, including photoluminescence (PL)-based (bio)chemical sensors using organic LEDs (OLEDs) as excitation sources [4]. The viability of a (bio)chemical sensing platform increases when the fabrication of all its components is simple, and they are compact and easily integratable. In this direction, an integrated platform based on OLED pixels excitation, a luminescing sensing medium, and PL-detecting organic photodetectors (OPDs) is a promising approach. This communication describes steps toward the development of such a compact sensing platform. In particular, a bulk-heterojunction OPD based on poly(3-hexylthiophene) and fullerene derivatives was engineered to be sensitive to the sensing film's PL, with a fast response time formonitoring analytes in both the PL intensity and PL decay time detection modes.

The need for (bio)chemical sensing systems is burgeoning for various analytical problems in fields such as medicine,the environment, defense and food. Optical sensing techniques – most notably luminescence based – are sometimes the only ones that provide adequate sensitivity [5]. In general, luminescence-based (bio)chemical sensors require three components (excluding the electronics and readout): a fluorescing or phosphorescing sensing element, a light source that excites the PL of that sensing element, and a photodetector. Traditional light sources are lasers or LEDs that cannot be easily integrated with the other components due to size, geometrical, or operational constraints [6]. Traditional photodetection elements include charge coupled device cameras,

photomultiplier tubes, and inorganic photodiodes, which are also hampered by integrability issues. In the past few years, Shinar et al. have demonstrated the efficacy of the OLED-based platform for PL-based sensing of various analytes [7-13]. We believe that integration of organic photodetectors (OPDs) with this - hence an all-organic sensing platform - has the potential to truly enable the development of flexible, thin, miniature sensor arrays via a facile and low-cost fabrication route. There have been only a few reports on the use of OPDs in PL-based sensors. Kraker et al. [14] recently reported a solid-state OLED/dye/OPD sensing system for PLintensity-based detection, requiring polarization filters to prevent the OLED's electroluminescence (EL) from reaching the OPD. Such EL blocking is crucial for the intensity-based detection methodology. Hofmann et al. [5] reported the use of an OPD to monitor a chemiluminescent reaction in a microfluidic system. Here, we report for the first time, the exploration of an OLED/dye/OPD-based sensing system in both PL intensity (I) and decay time (τ) detection modes. The τ mode is preferable as it eliminates the need for (i) frequent sensor calibration, since τ is insensitive to changes in I, minor film degradation, or background light [9,15,16] and (ii) optical filters, as τ is monitored during the off period of the pulsed excitation.

We explored poly(3-hexylthiophene): [6,6]-phenyl-C61-butyric acid methyl ester (P3HT:PCBM)-based bulk-heterojunction type devices as our OPDs due to their solution processibility and superior performance in the area of photovoltaics [17,18]. For quantitation of our OPD's response, oxygen and glucose were chosen as the analytes. The sensing element usually containsan oxygen-sensitive dye, such as Pt or Pd octaethylporphyrin (PtOEP or PdOEP, respectively) [7-13]. The collisions of the dye molecules with O_2 decrease I and τ [9,15,16]. Ideally, in a homogeneous matrix, the O_2

concentration can be determined by monitoring τ or the steady-state I using the Stern–Volmer (SV) equation [19]

$$I_o/I = \tau_o/\tau = 1 + K_{SV}[O_2] \quad (1)$$

Where I_o and τ_o are the unquenched values and K_{SV} is a constant. We used PtOEP in our experiments. It was embedded in a TiO_2 nanoparticle-doped polystyrene film. TiO_2 improves EL absorption by PtOEP by increasing scattering within the polystyrene matrix [11]. Both inorganic LEDs and small-molecule OLEDs were utilized as green excitation sources (emission peak ~ 525 nm). The LEDs were operated in a pulsed mode (100 µs pulse width at 50 Hz). The PL of the sensing film is in the red region (~640 nm). Hence, as a first step, the processing of the P3HT:PCBM active layer was tailored to improve the photoresponse of these OPDs in the red, which otherwise peaks in the green and is weak in the red [17,18].

4.3 Experimental Details

OPD fabrication and characterization: For OPD fabrication, a conducting film of poly(3,4-ethylenedioxythiophene) doped with poly(styrenesulfonate) (PEDOT:PSS, Clevios P) was spin coated at 3000 rpm after UV-Ozone plasma exposure of cleaned ITO-coated slides, followed by annealing at 120˚C for 5 minutes. The P3HT:PCBM blend solution (17mg/ml in dichlorobenzene) was spin coated at different speeds. An Al (100 nm) electrode was deposited by thermal evaporation on top of the active layer. The absorption spectra were measured by a Varian Cary 5000 UV-Vis-NIR spectrophotometer. EQE measurements were done using ELH Quartzline lamp (120V-300W from GE) and a monochromator with a lock-in amplifier to eliminate background noise. The reference was

a calibrated Si photodiode with known EQE spectra. The P3HT:PCBM layer thicknesses were obtained by forming a 100 μm wide scratch on the films using a fine blade. AFM (Veeco Nanoscope III) tip in tapping mode was scanned across the scratch to find the thickness of the P3HT:PCBM films. Raman spectra were recorded on a Renishawin Via Raman microscope equipped with a low noise and high sensitivity RenCam CCD detector, and a 488 nm, 0.3 mW laser. The reflected Raman signal was collected using a 50X objective with a numerical aperture of 0.7. The signal collection time was 10 s and the scan was averaged twice. To mimic the device fabrication conditions, all the films for absorption and Raman spectra measurement were spun cast on PEDOT:PSS-covered ITO-coated glass substrates.

OLED Fabrication: 20 Ω/□ ITO/glasswas obtained from Colorado Concept Coatings. Copper phthalocyanine (CuPc) and LiF were obtained from Sigma-Aldrich. N,N'-diphenyl-N,N'-bis(1-naphthyl phenyl)-1,1'-biphenyl-4,4'-diamine (NPD), 2,3,6,7-Tetrahydro-1,1,7,7,-tetramethyl- 1H,5H,11H-10-(2- benzothiazolyl) quinolizino-[9,9a,1gh] coumarin (C545T), and tris(8-hydroxyquinoline) Al(Alq_3) were obtained from H.W. Sands. Green emitting (peaking at ~525 nm) OLED pixels were fabricated by thermally evaporating organic materials on top of ~150 nm thick cleaned and UV ozone-treated ITO-coated glass. The organic layers, in sequence, are the hole injection layer ~5 nm CuPC, hole transport layer ~50 nm NPD, doped emitting layer ~20 nm C545T:Alq_3 (1% w/w), and electron transport layer ~30 nm Alq_3, which is followed by an electron injection layer ~1 nm LiF and the ~100 nm Al cathode. OLED pixels were generated by etching the ITO into two 2 mm wide strips; the OLED pixels are defined by the overlapping regions of mutually

perpendicular ITO and Al strips. Two OLED pixels (2 mm × 2 mm) were used as the excitation source for the PL measurements.

Sensing Experiment: PS:PtOEP sensor films were prepared by drop casting 50 µL of a toluene solution with 1mg/mL PtOEP, 1mg/mL TiO_2 and 40mg/mL polystyrene. The films were dried in the dark at ambient temperature. GOx from *Aspergillusniger*was obtained from Sigma-Aldrich. GOx and glucose (Fisher Scientific) were dissolved in phosphate buffer (PH 7.4), at the desired concentrations. The sensor components - an LED, PS:PtOEP sensing film, long-pass filter, and P3HT:PCBM OPD - were assembled in a front detection mode, where the sensing film is sandwiched between the OPD and LED. For O_2 sensing experiments, the sensor film was enclosed in a flow cell through which different volumetric ratios of Ar/O_2 mixture gas were passed. The inorganic LEDs were operated in a pulsed mode at a bias of 3.7 V, pulse width of 100 µs,and a repetition rate of 50 Hz. The photocurrent signal from the OPD at zero bias was amplified using a gain of 10^6 V/A at 200 kHz bandwidth, and monitored on an oscilloscope. The PL lifetimes were obtained by monitoring the OPD response following the application of the LED pulse. For glucose sensing, a glass tube was glued on top of the sensor film, forming a reaction well (200 µL in volume), enclosing the dye-coated film at the bottom. 100 µL of glucose and GO_x were sequentially added into the reaction well, followed by hermetic sealing using a cover glass. The PL signal was collected by the OPD after 1 minute of adding the solutions. The concentration of GO_x (300 units/mL) was sufficient to catalyze glucose oxidation in the range of 0~0.3 mM, deplete the DO in 20 sec.

4.4 Results and discussion

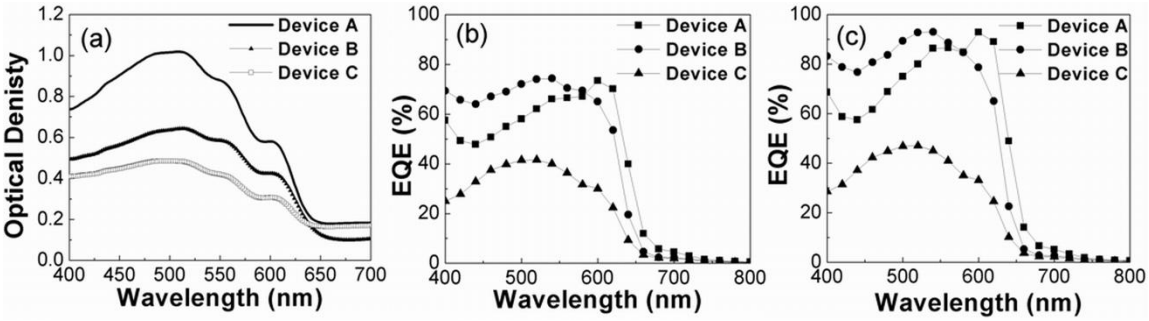

Figure 4.1: Effect of active layer growth conditions. (a) UV-Vis absorption spectra for films of P3HT/PCBM (1:1 wt/wt ratio), spin coated at 400 rpm for 30 seconds - Device A, 600 rpm for 60 seconds - Device B, and 1000 rpm for 60 second - Device C. (b) EQE spectra of devices A, B, and C at short circuit; and (c) at 0.5 V reverse bias.

In an effort to red-shift the EQE spectrum, three types of OPDs (A, B, and C) with different active layer thicknesses were obtained by spin-coating at 400, 600 and 1000 rpm for 30, 60, and 60 seconds, respectively (see appendix for device schematic). The absorption spectra of these P3HT:PCBM layers are shown in Figure 4.1(a). Device A, because its active layer is thicker (~350 nm) than those of devices B (~220 nm) and C (~140 nm), demonstrates the highest absorption at all wavelengths. The three absorption shoulders are more pronounced in device A, indicating a higher degree of self- organization of P3HT chains arising from the slowest drying rate, due to the lower spin speed and duration [17]. This self-organization leads to high crystalline order involving an enhanced conjugation length of P3HT chains [17,20]. The EQE spectra for the three devices were measured in short-circuit condition [Figure 4.1(b)], and at 0.5 V reverse bias [Figure 4.1(c)]. The EQE at short circuit condition for device A shows a maximum of ~70% at 600 nm, while the peak is at 540 nm (EQE ~70%) for device B, and 520 nm (EQE ~40%) for device C. The thinner films' thickness (devices B and C) is less than the penetration depth of the strongly absorbed green light, so that the green photons can create a uniform

distribution of photogenerated carriers throughout the thickness. But for the thicker film (device A), green photons, having a high absorption coefficient, are absorbed closer to the anode. This makes the electrons more susceptible to recombination, as they have to travel the entire active layer thickness to reach the Al electrode. In contrast, the red photons can penetrate greater thickness to generate a more uniform carrier distribution. Hence, for device A, the collection efficiency of charge carriers created by red photons is higher than that created by green photons, which explains the 600 nm EQE peak. The EQE dependence on wavelength does not change with 0.5 V reverse bias. However, collection at every wavelength improves, enhancing the overall EQE. At PtOEP's emission peak of 640 nm, device A showed the highest EQE of ~40% at 0 V and ~50% at -0.5 V. In general, photodetectors can be operated at either zero or reverse bias. Operation at zero bias is however advantageous in one aspect, that is, lower dark current which assures a high dynamic range. For device A, the dark current was less than 1 nA/cm^2, leading to a dynamic range exceeding 10^7 (see appendix).

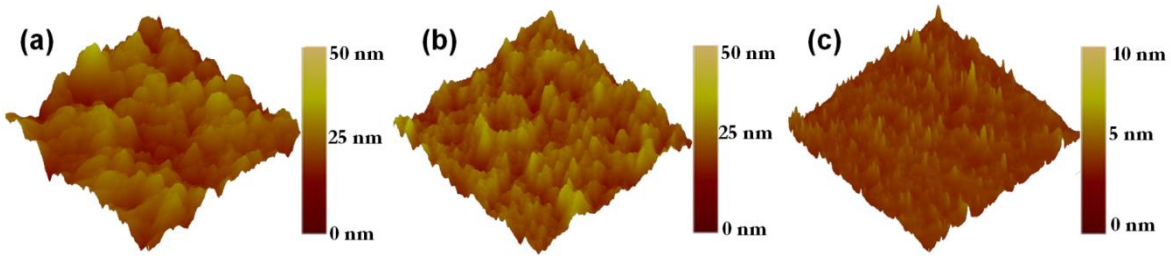

Figure 4.2: AFM height images of the P3HT/PCBM composite films (PCBM concentration = 50 wt%) showing the active layer of (a) device A (b) device B and (c) device C. Scan area is 5 μm×5 μm in all cases. Note that the color scale for films A and B is 0–50 nm, whereas for film C it is 0–10 nm.

To elucidate the structural properties of the P3HT:PCBM films, atomic force microscopy (AFM) was employed. Height AFM images (Figure 4.2) show that the surface

r.m.s. roughness values, σ, for films A and B are 10.7 nm and 7.2 nm, respectively. For film C, the smoothest surface, with σ ~1.05 nm, is observed. The high surface roughness of slowly spin-coated films A and B is another signature of polymer (blend) self-organization, and can be correlated to formation of nanocrystallites due to ordering and stacking of P3HT supermolecules [17]. Raman spectra also show narrowing of the peak related to –C=C– symmetric stretching in the active layer of device A, which indicates higher P3HT crystallinity (see appendix) [21-24]. Higher P3HT crystallinity involves enhanced conjugation length, which leads to enhanced absorption in the red. This, in addition to greater film thickness, can also be partially responsible for enhanced red EQE in device A.

Due to enhanced EQE in the red, device A was chosen as the OPD for our sensors. The OPD, assembled with the sensing film and a 600 nm long-pass filter, was first tested for O_2 sensing using the inorganic LED with peak emission at ~525 nm. In another experiment, an OLED was used. As a first step towards structural integration, the LED, PS:PtOEP sensing film, long pass filter, and P3HT:PCBM OPD were assembled in the front detection geometry (see supporting information for schematic). The filter was placed between the OPD and the sensing film to prevent the green EL from reaching the OPD. Note that the filter is required only for the *I* detection mode. The τ mode does not require it, since measurements are done following the excitation pulse, i.e. in the (O)LED's off state.

Figure 4.3 shows the OPD response to the sensor'sPL following the LED excitation pulse and exposure to different concentrations of O_2 in Argon. As expected, *I* and τ decrease with increasing O_2 concentration due to collisional quenching, to which the OPD responds with a reduced photocurrent and its faster decay. This PL quenching of PtOEP by O_2 is due to the paramagnetic triplet nature of ground state O_2 and singlet nature of excited

O_2 [16], which is unique among common gases. Figure 4.3(b) shows I_o/I ($I_o$is the intensity in 100% Ar) versus the gas-phase O_2 concentration. The dependence was found to be linear with O_2 concentration up to 40 % O_2, with signal ratio S ≡ I_o/I (40% O_2) ~ 10, which can be further improved by using a 630 nm long-pass filter. The SV curve for the τ mode shows that τ_o/τ for 20% oxygen is 2.5, which is lower than the I mode ratio. However, other advantages associated with the τ mode, as discussed earlier, make it more viable for practical applications. The deviation of the τ mode SV plot from linearity probably arises from inhomogeneity in the dye's environment, i.e. the dye molecules occupy quencher-easy accessible and quencher-difficult accessible sites [25], which leads to different contributions to PL quenching. However, the exact mechanism is not clear at this point.

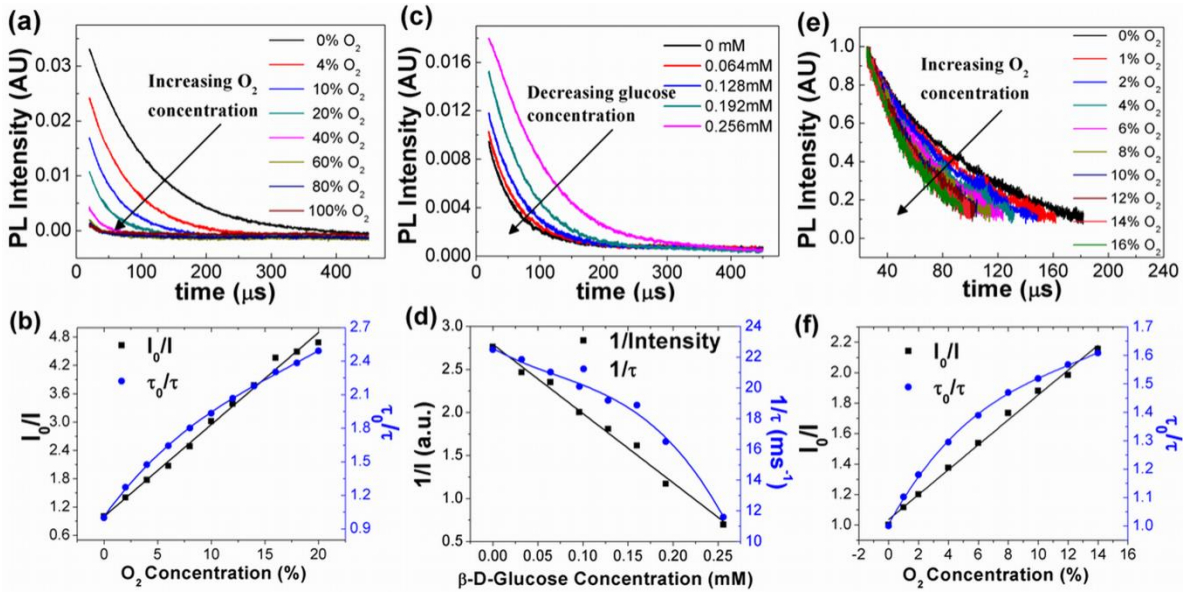

Figure 4.3: The effect of concentration of gas-phase O_2 (a) and glucose (c) on the OPD's temporal photocurrent response. Excitation source was an LED. (b) and (d) are I and τ-based SV calibration curves corresponding to (a) and (c), respectively. For OLED excited O_2 sensor, (e) and (f) show the effect of O_2 concentration on the OPD temporal response and corresponding SV calibration curves, respectively.

Glucose sensing using the LED/PS:PtOEP sensing element/P3HT:PCBM OPD configuration relied on the enzymatic oxidation of glucose by glucose oxidase (GO_x) and

oxygen. In the presence of glucose and GO_x, the PL quenching of the dye molecules is reduced due to consumption of dissolved oxygen (DO). The DO's initial concentration ($[DO]_{initial}$) in water is ~0.26 mM at room temperature. For a concentration of the active isomer of glucose ($[\beta\text{-D-glucose}]_{initial}$)< $[DO]_{initial}$, at the completion of the oxidation reaction, $[\beta\text{-D-glucose}]_{initial}$ equals the difference between the initial and final DO levels. With increased $[\beta\text{-D-glucose}]_{initial}$, the residual DO decreases, hence the I and τ of PtOEP increase [Figure 4.3 (c), (d)]. Integration under the PL τ curve, corresponding to each $[\beta\text{-D-glucose}]_{initial}$,was used to represent the I. It can be seen that $1/I$ is linear with $[\beta\text{-D-glucose}]_{initial}$, which is expected from a modified SV equation [12]. The τ mode curves slightly deviate from linearity similar to the case of the gas-phase O_2.

Finally, following the demonstration of the suitability of the OPD for O_2 and glucose sensing, including inthe τ mode, the inorganic LED was replaced by an OLED to demonstrate the viability of an all-organic sensor platform. In this experiment, I and τ clearly decrease as the O_2 concentration is increased, as expected [Figure 4.3(e),(f)]. The observed higher noise in the photocurrent decay curves is due to instabilities in the EL and lower brightness than the inorganic LED. $I_o/I$is linear with O_2 concentration and the ratio I_o/I for 15% oxygen is 2.1. Although this ratio should be the same whether using an LED or OLED, it has previously been shown that weaker excitation by the OLED generally results in a lower ratio [10,13]. The results with the OLEDs can therefore be improved by utilizing brighter (and encapsulated) OLEDs. The ratio τ_o/τ for 15% oxygen is 1.6 and is comparable to the value observed when using the inorganic LED, since performance in the τ mode is independent of the intensity of excitation source.

4.5 Conclusions

In summary, a structurally integrated all organic sensing platform - OLED pixels exciting a luminescent dye; the dye's PL intensity and decay-time depending on an analyte's concentration; and these PL changes of the dye being detected by OPDs - is a promising approach to achieve low-cost, flexible and compact sensor arrays. This communication presented steps towards realizing this paradigm in one the several possible embodiments - a front detection geometry, wherein, the (O)LED, the dye embedded film, and the OPD were spatially assembled in the same order. We engineered the P3HT:PCBM OPDs to tailor their photoresponse towards the red emitting dye (PtOEP) based O_2 and glucose sensors. Devices realized from a thicker and slower-grown P3HT:PCBM layer showed the highest EQE of 40% without bias at 640 nm, which is the peak emission of the sensing dye. Oxygen and glucose were monitored using the optimized OPD via detection of the dye's I or τ. The latter eliminates the need for frequent sensor calibration or optical filters. The response of the OPDs was sufficiently fast to monitor the O_2 using the τ mode. Finally, after demonstrating the efficacy of OPDs with inorganic LEDs, this report also demonstrated all-organic O_2 sensors, which, in addition to OPDs, used OLEDs as the light source.

4.6 Acknowledgements

SC, KSN and AL thank the Institute of Physical Research and Technology, Iowa State University for Company Assistance grant. SC, RS and JS thank the Iowa Power Fund.

JS and YC thank the Ames Laboratory, which is operated by Iowa State University for the US Department of Energy (USDOE) under Contract No. DE-AC 02-07CH11358. The work was partially supported by the Director for Energy Research, Office of Basic Energy Sciences, USDOE. RS and Integrated Sensor Technologies thank NSF for an SBIR Phase II grant.

4.7 Appendix

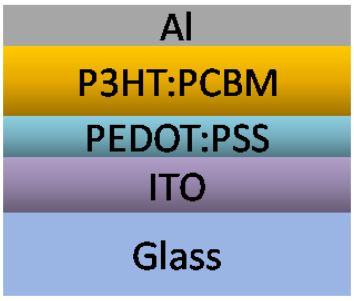

Figure 4.4: Schematic of the photodetecting device.

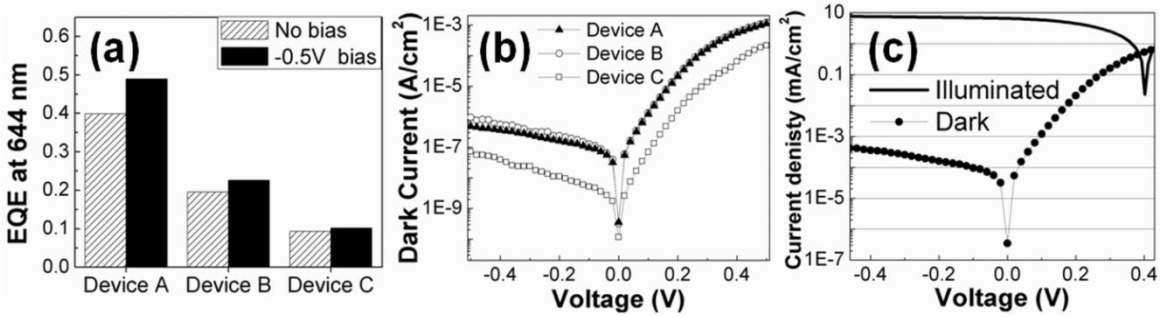

Figure 4.5: (a) Comparison of EQE at 640 nm for devices A, B and C at short-circuit condition and at 0.5 reverse bias. (b) Dark current-voltage characteristics of the three types of devices. (c) Dark and illuminated current-voltage characteristics of the Device A.

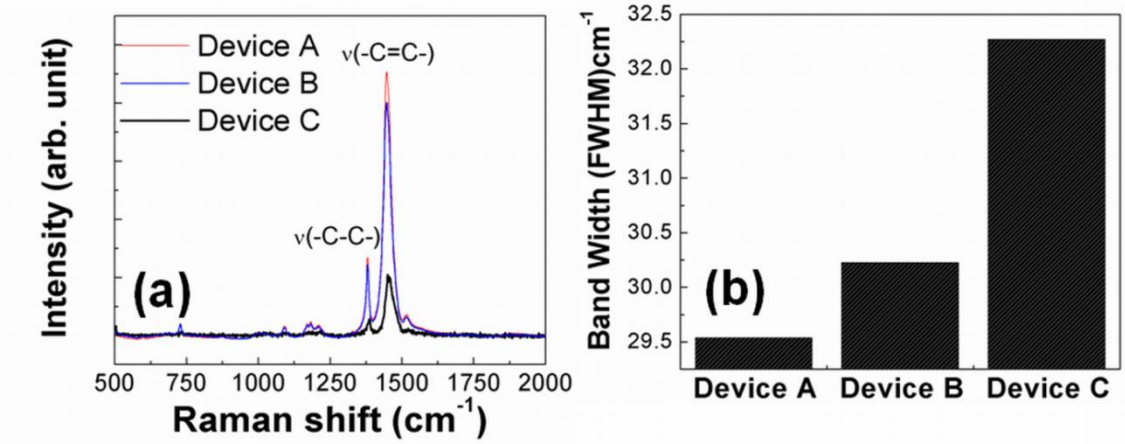

Figure 4.6: (a) Raman spectra and (b) corresponding FWHM of $\nu_{\text{-C=C-}}$ peak (1440-1450 cm^{-1}) for three device types with different spin coating conditions.

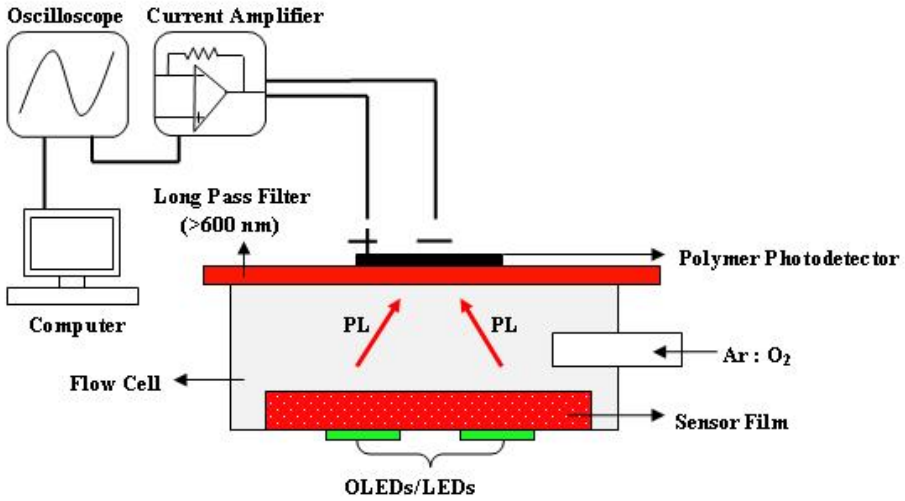

Figure 4.7: Schematic of the sensing set-up: Inorganic or organic LED excitation source, sensing film with PtOEP, and P3HT:PCBM OPD (device A) were assembled in a front detection geometry.

Discussion of Raman spectra: The Raman spectra show peaks at 1440-1450 and 1380 cm^{-1}, that are attributed to the –C=C– symmetric stretching ($\nu_{C=C}$) and the –C–C– skeletal stretching (ν_{C-C}) of the thiophene ring, respectively [ref. 21,22,24 of main text]. When P3HT is more crystalline, the thiophene rings are, on average, more closely stacked. This should lead to narrowing in the $\nu_{C=C}$ [ref. 21-24 of main text]. Thus, the full width at

half maximum (FWHM) of the $\nu_{C=C}$ band can also be correlated with changes in the P3HT conformation, conjugation length, and nanostructure. Minimum value of FWHM was observed for device A, which indicates an increase in the crystallinity of P3HT and the extension of the effective conjugation length along the polymer backbone.

4.8 References

[1] H-Y. Chen, J. Hou, S. Zhang, Y. Liang, G. Yang, Y. Yang, L. Yu, Y. Wu, G. Li, *Nat. Photon.***2009**, *3*, 649.

[2] K. M. Vaeth, *Inform. Display***2003**, *19*, 12.

[3] X. Gong, M. Tong, Y. Xia, W. Cai, J. S. Moon, Y. Cao,G. Yu, C-L.Shieh, B. Nilsson, A. J. Heeger, Science **2009**, *325*, 1665.

[4] J. Shinar, R. Shinar,*J. Phys. D: Appl. Phys.***2008**,*41*, 133001.

[5] O. Hofmann, X. Wang, A. Cornwell, S. Beecher, A.Raja, D. D. C. Bradley, A. J.deMello, J. C.deMello, *Lab Chip***2006**, *6*, 981.

[6] E. J.Cho,F. V. Bright, *Anal. Chem.* **2001**,*73*, 3289.

[7] V.Savvate'ev, Z.Chen-Esterlit, J. W.Aylott,B.Choudhury, C. H. Kim,L.Zou, J. H.Friedl,R. Shinar, J. Shinar, R. Kopelman, *Appl. Phys. Lett.***2002**, *81*, 4652.

[8] B. Choudhury, R. Shinar, J. Shinar, *J. Appl. Phys.***2004**, *96*, 2949.

[9] R. Shinar, Z. Zhou, B. Choudhury, J. Shinar, *Anal. Chim. Acta***2006**, *568*, 190.

[10] R. Shinar, D. Ghosh, B. Choudhury, M.Noack, V. L.Dalal, J. Shinar,*J. Non-Cryst. Solids***2006**, *352*, 1995.

[11] Z. Zhou, R.Shinar, A. J.Allison, J.Shinar, *Adv. Funct. Mater.***2007**, *17*, 3530.

[12] Y. Cai, R. Shinar, Z. Zhou, J. Shinar, *Sensors Actuators B* **2008**, *134*, 727.

[13] D. Ghosh, R. Shinar, V.Dalal, Z. Zhou, J. Shinar, *J. Non Cryst. Solids***2008**, 3*54*, 2606.

[14] E. Kraker, A. Haase, B. Lamprecht, G.Jakopic, *Appl. Phys. Lett.***2008**, *92*, 033302.

[15] O. S. Wolfbeis, (Ed.), Fiber Optic Chemical Sensors and Biosensors, CRC Press, BocaRaton, FL, **1991**.

[16] Y. Amao, *Michrochim. Acta***2003**, *143*, 1.

[17] G. Li, V.Shrotriya, J. Huang, Y. Yao, T. Moriarty, K. Emery, Y. Yang, *Nat. Mater.***2005**, *4*, 864.

[18] J. Y. Kim, S.H. Kim, H. H. Lee, K. Lee, W. Ma, X. Gong, A. J.Heeger, *Adv. Mater.***2006**, *18*, 572.

[19] J. R.Lakowicz, *Principles of Fluorescence Spectroscopy*, Plenum Press, New York **1983**.

[20] M. Sunderberg, O.Inganas, S. Stafstrom,G. Gustafsson, B.Sjogren, *Solid State Commun.***1989**,*71*,435.

[21] J. Casado, R. G. Hicks, V. Hernandez, D. J. T. Myles, M. C. R. Delgado, J. T. L. Navarrete, *J. Chem. Phys.***2003**, *118*, 1912.

[22] Y. W. Goh, Y. F. Lu, Z. M. Rem, T. C. Chong, *Appl. Phys. A: Mater. Sci. Process.***2003**, *77*, 433.

[23] P. S. O. Patrico, H. D. R.Calado, F. A. C. de Oliveira, A.Righi, B. R. A. Neves, G. G. Silva, L. A. Cury, *J. Phys.: Condens. Matter***2006**, *18*, 7529.

[24] E. Klimov, W. Li, X. Yang, G. G. Hoffmann, J. Loos, *Macromolecules***2006**, *39*, 4493.

CHAPTER 5. Growth rate dependent trap density in polythiophene-fullerene solar cells and its implications[1]

Modified from a paper published in *Applied Physics Letters*

Kanwar S. Nalwa[2,3], Rakesh C. Mahadevapuram[4], and Sumit Chaudhary[2,5]

5.1 Abstract

To understand the effect of processing conditions such as spin-coating speed and drying rate on the density of defects; poly(3-hexylthiophene) (P3HT):fullerene-derivative (PCBM) solar cells A, B and C were fabricated with solvent drying times of ~ 40, 7 and 1 minutes, respectively. We show that slowest grown device A has one order of magnitude less sub-bandgap traps than device C. The open-circuit voltage and its light-intensity dependence was strongly affected by interfacial recombination of carriers at sub-gap defect states. The losses due to trap-assisted recombination can even dominate over bimolecular recombination, depending on the density of defect states.

5.2 Introduction

Organic photovoltaics (OPVs) have gained much attention in the past two decades because they offer the promise of low-cost solar-electric conversion, with advantages including mechanical flexibility, light weight, ease of processing and roll-to-roll production

---

[1] Reprinted with permission from: K. S. Nalwa, R. C. Mahadevapuram, and S. Chaudhary, "Growth rate dependent trap density in polythiophene:fullerene solar cells and its implications", *Applied Physics Letters*,**98**, 093306, 2011. Copyright 2011, American Institute of Physics.

[2] Graduate student and Assistant Professor, respectively, Department of Electrical and Computer Engineering, Iowa State University.

[3] Primary researcher and author.

[4] Graduate Student, Department of Material Science and Engineering, Iowa State University.

[5] Author for correspondence

capability. Significant progress has been made over the last five years through optimization of materials processing parameters [1-3], and the emergence of new conjugated polymers with tailored energy levels [4-6]. Power conversion efficiency > 7% has recently been achieved [5]. Yet, the field of OPVs seems to be progressing almost more by trial and error than by conception, ascribing to the lack of fundamental understanding about several aspects, e.g. defects. In order to further improve OPV performance, it is crucial to extract information about defect states and their role as trapping or recombination centers.

Defects often have a controlling influence on the properties of inorganic semiconductors [7], yet their role in OPVs remains mostly overlooked, let alone the factors that give rise to these defects. Semiconductor properties such as charge carrier mobility, exciton diffusion length and photostability of conjugated polymers have been shown to be strongly influenced by mid gap states arising from defects [8,9]. Defects within the band-gap alter the electric field profile and might reduce the drift driving force for the charge transport, and consequently diminish carrier collection at the contacts [10]. Depending upon the amount of defects and their recombination strength, the losses due to trap-assisted recombination can lower the fill factor and short-circuit current. This was shown for the case of trap-limited electron transport in BHJ OPV cells with cyano-PPV derivatives as electron acceptors [11,12]. When defect states are present in the electron donor, the dissociation of bound pairs at the interface leads to free carriers, but now part of the holes can be trapped. For the holes trapped close to the interface, there is a probability of recombination with the free electrons in acceptor, leading to loss of both carriers. This trap-assisted recombination process adds to the Langevin (bimolecular) recombination, contributing to loss mechanisms in a BHJ OPV. Therefore, it becomes imperative to

understand the processing-related factors that produce these defects to be able to defect-engineer the OPVs for achieving higher performance.

Processing factors such as thermal annealing and slow growth have been shown to increase hole mobility, polymer crystallization, photon absorption and hence the efficiency of the OPVs [6,7]. But the effect of growth conditions on the defect density is not quantitatively known. This paper investigates the effect of growth rate on the defects in poly(3-hexylthiophene): [6,6]-phenyl-C61-butyric acid methyl ester (P3HT:PCBM) based BHJ PV cells and their influence on the electrical properties of the OPV cells. Energy distributions [density-of-states (DOS)] of defects in the effective band gap of P3HT:PCBM bulk heterojunctions are determined by analyzing capacitance dependence on both bias voltage $C(V)$ and frequency $C(f)$ of complete cells [13], as well as sub-band gap quantum efficiency measurement. This study reveals that slower growth rate leads to reduction of total defect density by an order of magnitude.

5.3 Experimental Details

For device fabrication, a conducting film of poly(3,4-ethylenedioxythiophene) doped with poly(styrenesulfonate) was spin coated on cleaned ITO glass substrate. Subsequently, P3HT:PCBM (1:1 ratio, total 17 mg/ml in dichlorobenzene) active layers (A, B, and C) were spin coated (under an argon atmosphere) at 400, 600 and 1000 rpm for 30, 60, and 60 seconds, obtaining solvent evaporation time of ~ 40, 7 and 1 minutes and thicknesses of 350, 220 and 140 nm respectively. The solvent evaporation time after spin coating was measured by visually inspecting the change in film color when it solidifies from the liquid phase. Al (100 nm) electrode was deposited by thermal evaporation on top

of the active layer. The laser wavelength and power used for acquiring Raman spectra was 488 nm and 0.23 mW respectively. To measure photocurrent versus voltage, devices were illuminated using ELH Quartzline lamp operating at 1 sun intensity i.e. 100 mW/cm^2 (calibrated using crystalline Si photodiode with a KG-5 filter). Intensity dependence of the open circuit voltage (V_{oc}) was measured using a set of neutral density filters. Sub-gap external quantum efficiency (EQE) measurements were done using ELH Quartzline lamp and a monochromator with a lock-in amplifier to eliminate background noise. For hole mobility measurements, Pd was used as the top electrode to ensure hole only transport, and electric field dependence of hole mobility was taken into account. Zero field hole mobilities were calculated by fitting thelinear region (at high voltage) of $\log(J/V^2)$ versus $V^{1/2}$ (where J is current density) plots obtained in dark. At high electric fields, the space charge limited current becomes predominant, such that the effects of traps on the charge transport can be neglected because all the traps are filled [14]. The capacitance measurements were performed with a PARSTAT-2273 equipped with a frequency analyzer module. AC oscillating amplitude was as low as 10 mV (rms) to maintain the linearity of response. Measurements were performed at zero bias for $C(f)$, and at 100 Hz for $C(V)$ analysis, always in dark conditions and at room temperature.

5.4 Results and discussion

In Figure 5.1(a), the Raman spectra show peaks at 1440-1450 and 1380 cm^{-1}, that are attributed to the –C=C– symmetric stretching ($\nu_{C=C}$) and the –C–C– skeletal stretching (ν_{C-C}) of the thiophene ring, respectively [15-17]. When P3HT is more crystalline, the

thiophene rings are, on average, more closely stacked. This should lead to narrowing in the $\nu_{C=C}$ [15-18]. The values of full width at half maximum for this peak were 29.5 cm^{-1}, 30.25 cm^{-1}, and 32.25 cm^{-1} for device A, B and C, respectively. The minimum value for device A is another signature of polymer self-organization contributing to increased crystallinity of P3HT. Hence, slow growth (high solvent evaporation time) is observed to impart more crystallinity to the P3HT phase in device A as compared with the fast-grown device C.

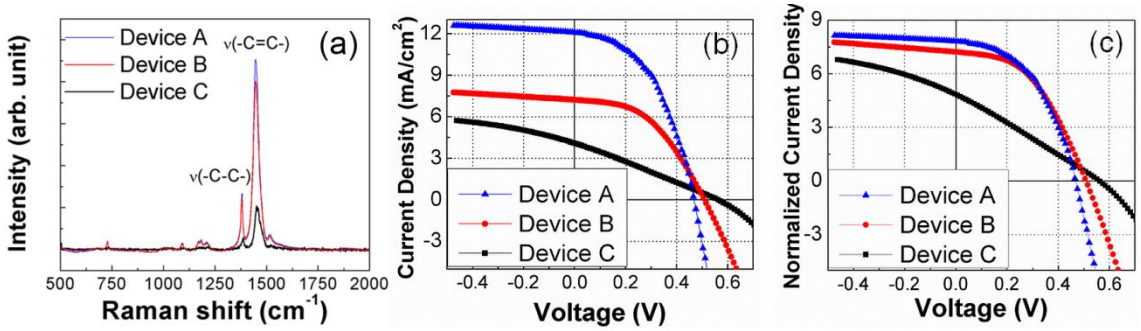

Figure 5.1: (a) Raman spectra of the active-layer, and (b) Photocurrent J_L-V characteristics under illumination for three device types with different spin coating conditions. (c) Photocurrents, J_L of devices A and C have been normalized, such that the devices have optical absorption equivalent to device B, thus eliminating the optical absorption variations due to different thicknesses.

As shown in Figure 5.1(b), slow-grown device A exhibits short-circuit current density of 12 mA/cm^2 which is one of the highest values reported in literature for this system [1,2] and is ascribed to thicker film (more photons absorbed) as well as more crystalline nature of P3HT (high hole mobility ~ 8×10^{-4} $cm^2\ V^{-1}\ s^{-1}$). Fast growth clearly increases the V_{oc} of the device C due to increase in the energy of interfacial charge-transfer state as a result of amorphous nature of P3HT [19]. This is accompanied by a decrease in fill factor, from ~ 50% for device A to 27 % for device C. Figure 5.1(c) illustrates similar information as Figure 5.1(b), but the variation in photocurrents due to different thicknesses (different optical absorption) has been eliminated, thus revealing only the effect of charge transport on photovoltaic performance. Low fill factor in fast grown film has been earlier attributed to a decrease in

hole mobility (~2.0×10^{-6} cm^2 V^{-1} s^{-1}) and unbalanced charge transport leading to space charge-limited photocurrent [1]. However the effect of P3HT morphology and resulting defects remains yet to be identified.

In Figure 5.2(a), the sub band gap DOS as a function of energy with respect to the P3HT highest occupied molecular orbital (HOMO) level, E-E_{HOMO} for devices A, B and C is plotted. The plot was generated from $C(V)$ and $C(f)$ measurements, using method detailed by Boix et al. [13]. The energy density of defect states, $g_t(E_\omega)$ can be analyzed by regarding a Gaussian shape [20] centered at the maximum of the distribution E_0

$$g_t(E_\omega) = \frac{n_t}{\sqrt{2\pi\sigma}} \exp\left[-\frac{(E_0 - E_\omega)^2}{2\sigma^2} \right] \quad (1)$$

Where E_ω is the demarcation energy and σ is the disorder parameter. n_t, the total density of traps is found to be 3.3×10^{15} cm^{-3}, 5.2×10^{15} cm^{-3} and 2.1×10^{16} cm^{-3} for devices A, B and C respectively. The investigated defect states shown in Figure 5.2(a) have been shown to only belong to P3HT, as such behavior was not exhibited at all by devices containing only PCBM molecules [13]. The defect density follows the same trend as that of non-crystallinity (disorder) of P3HT in films i.e. increasing on increasing the growth rate. These states could be a consequence of conformational defects accompanying the ordering of the aromatic chain backbone. Several types of structural defects such as twisting-tilting of one monomer unit out of the conjugation plan and loss of p-p stacking either through tilting or lateral displacement of adjacent polymer chains have been known to create defect states in the P3HT HOMO-lowest unoccupied molecular orbital (LUMO) gap [21,22]. The extent of such structural distortions is related to the crystallinity of the film, since disorder (twisting and coiling of P3HT chains) increases with increase in amorphous nature [1]. Therefore

slow growth can be directly linked to higher crystallinity and lower sub-gap defect density of P3HT in film A. Normalized (at 2.0 eV) EQE spectra of OPVs in the sub gap region is shown in Figure 5.2(b). Lower sub-band gap absorption in device A further corroborates the aforementioned finding that slow growth induced self-organization leads to lower defect density in the P3HT band gap.

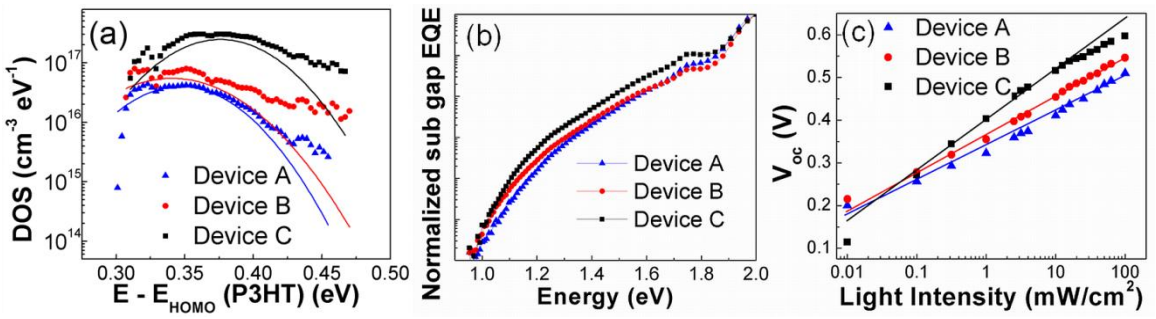

Figure 5.2: (a) Density of defect states as a function of the energy with respect to the P3HT HOMO level (demarcation energy), E-$E_{HOMO,}$ (b) Normalized (at 2.0 eV) EQE spectra measured in the sub gap region, and (c) V_{oc} light intensity dependence of devices A, B and C. The solid lines in (c) are linear fits used to calculate the slope, S.

In case of Langevin (bimolecular) recombination of free carriers being the only loss mechanism, it has been shown that the V_{oc} of the OPVs follow [23]

$$V_{oc} = \frac{E_{gap}}{q} - \frac{kT}{q}\ln\left[\frac{(1-P)\gamma N_c^{\,2}}{PG}\right] \qquad (2)$$

where E_{gap} is the energy difference between the HOMO of the electron donor and the LUMO of the electron acceptor, q is the elementary charge, k the Boltzmann constant, T the temperature, P is the dissociation probability of the electron-hole pairs into free carriers, γ is the recombination constant, N_c is the density of states in the conduction band, and G is the generation rate of electron-hole pairs. Since G is the only term directly proportional with the light intensity (with P and γ not depending on it), this formula contains the dependence of the V_{oc} on the light intensity. Therefore, the slope S=(kT/q) of the V_{oc} versus the natural

logarithm of the light intensity is predicted by the formula and has been found to be in good agreement for MDMO-PPV:PCBM solar cells [23]. A slope of 1.5(kT/q) has been measured for all-polymer solar cells with electron traps contained in the acceptor phase [11,12]. This deviation has been explained by including trap-assisted Schokley-Read Hall (SRH) recombination at the electron donor-acceptor interface in the device model developed for BHJ solar cells [11,12,24]. The trap-assisted interfacial recombination competes with the Langevin one, thereby the slope of V_{oc} versus natural logarithm of the light intensity increases with the strength of the trap-assisted recombination. In Figure 5.2(c), the dependence of V_{oc} on the light intensity is shown for devices A, B and C, with S= 1.1, 1.4 and 1.9 times (kT/q) respectively (calculated from the linear fit). In fast grown film case (device C), with one order of magnitude higher trap density in P3HT than slow grown active layer A, it is expected that the trap-limited recombination is stronger. Consequently, the dependence of V_{oc} on light intensity is more enhanced. The faster decay of V_{oc} for the trap-limited fast grown device C is a direct outcome of the fact that the presence of holes in trap levels above the HOMO of the P3HT raises the hole quasi-Fermi level. This increased amount of trap-assisted recombination in device C also leads to the observed reduction of the fill factor. Furthermore, the additional loss of free carriers due to stronger recombination (along with lower absorption in thinner film) results in reduction of the photocurrent in device C.

5.5 Conclusions

In conclusion, the slow growth assists the formation of self-organized ordered structure in the P3HT/PCBM blend system diminishing morphological defects in P3HT

chains. Fast growth, however results in an order of magnitude higher trap density owing to the structural defects (twists and bends) in P3HT chains. Lowering of hole mobility in fast grown film is expected to promote Langevin recombination, as it increases the hole density due to unbalanced charge transport. On the other hand, trap assisted interfacial recombination is aggravated by the presence of high trap density. The dependence of open circuit voltage on the light intensity reveals that trap-assisted recombination can possibly dominate over the Langevin recombination at 1 sun condition for films with high enough trap density. However, the quantification of recombination rates is required to determine the actual role of trap-assisted recombination at 1 sun condition and is a topic of our immediate research.

5.6 Acknowledgements

The authors thank state of Iowa's Office of Energy Independence for supporting this work through Iowa Power fund.

5.7 References

[1] G. Li, V. Shrotriya, J. S. Huang, Y. Yao, T. Moriarty, K. Emery, and Y. Yang, Nat. Mater. **4,** 864-868 (2005).

[2] W. L. Ma, C. Y. Yang, X. Gong, K. Lee, and A. J. Heeger, Adv. Funct. Mater. **15,** 1617-1622 (2005).

[3] J. Peet, J. Y. Kim, N. E. Coates, W. L. Ma, D. Moses, A. J. Heeger, and G. C. Bazan, Nat. Mater. **6,** 497-500 (2007).

[4] H. Y. Chen, J. H. Hou, S. Q. Zhang, Y. Y. Liang, G. W. Yang, Y. Yang, L. P. Yu, Y. Wu, and G. Li, Nat. Photonics **3,** 649-653 (2009).

[5] Y. Y. Liang, Z. Xu, J. B. Xia, S. T. Tsai, Y. Wu, G. Li, C. Ray, and L. P. Yu, Adv. Mater. **22,** E135-E138 (2010).

[6] S. H. Park, A. Roy, S. Beaupre, S. Cho, N. Coates, J. S. Moon, D. Moses, M. Leclerc, K. Lee, and A. J. Heeger, Nat. Photonics **3,** 297-302 (2009).

[7] P. T. Landsberg, *Recombination in semiconductors* (Cambridge University Press, 1991).

[8] B. A. Gregg, J. Phys. Chem. C **113,** 5899-5901 (2009).

[9] Z. Q. Liang, A. Nardes, D. Wang, J. J. Berry, and B. A. Gregg, Chem. Mater. **21,** 4914-4919 (2009).

[10] J. Nelson, *The physics of solar cells* (Imperial College Press, 2003).

[11] M. M. Mandoc, F. B. Kooistra, J. C. Hummelen, B. d. Boer, and P. W. M. Blom, Appl. Phys. Lett. **91,** 263505 (2007).

[12] M. M. Mandoc, W. Veurman, L. J. A. Koster, B. de Boer, and P. W. M. Blom, Adv. Funct. Mater. **17,** 2167-2173 (2007).

[13] P. P. Boix, G. Garcia-Belmonte, U. Munecas, M. Neophytou, C. Waldauf, and R. Pacios, Appl. Phys. Lett. **95,** 233302 (2009).

[14] M. Giulianini, E. R. Waclawik, J. M. Bell, and N. Motta, Appl. phys. lett. **94,** (2009).

[15] J. Casado, R. G. Hicks, V. Hernandez, D. J. T. Myles, M. C. R. Delgado, and J. T. L. Navarrete, J. Chem. Phys. **118,** 1912-1920 (2003).

[16] P. S. O. Patricio, H. D. R. Calado, F. A. C. de Oliveira, A. Righi, B. R. A. Neves, G. G. Silva, and L. A. Cury, J. Phys. Condens. Matter **18,** 7529-7542 (2006).

[17] E. Klimov, W. Li, X. Yang, G. G. Hoffmann, and J. Loos, Macromolecules **39,** 4493-4496 (2006).

[18] J. J. Yun, J. Peet, N. S. Cho, G. C. Bazan, S. J. Lee, and M. Moskovits, Appl. Phys. Lett. **92,** 251912 (2008).

[19] K. Vandewal, W. D. Oosterbaan, S. Bertho, V. Vrindts, A. Gadisa, L. Lutsen, D. Vanderzande, and J. V. Manca, Appl. phys. lett. **95,** 123303 (2009).

[20] H. Bassler, Phys. Status Solidi B-Basic Research **175,** 15-56 (1993).

[21] D. Q. Feng, A. N. Caruso, Y. B. Losovyj, D. L. Shulz, and P. A. Dowben, Polym. Eng. Sci. **47,** 1359-1364 (2007).

[22] A. N. Caruso, D. Q. Feng, Y. B. Losovyj, D. L. Schulz, S. Balaz, L. G. Rosa, A. Sokolov, B. Doudin, and P. A. Dowben, Phys. Status Solidi B-Basic Solid State Physics **243,** 1321-1330 (2006).

[23] L. J. A. Koster, V. D. Mihailetchi, R. Ramaker, and P. W. M. Blom, Appl. phys. lett. **86,** 123509 (2005).

[24] L. J. A. Koster, E. C. P. Smits, V. D. Mihailetchi, and P. W. M. Blom, Phys. Rev. B **72,** 085205 (2005).

CHAPTER 6. Dominant recombination mechanism in polymer solar cells is bimolecular or interfacial: depends on processing conditions of active layer

Modified from a paper submitted to *Advanced Functional Materials*

Kanwar S. Nalwa[1,2], Hari K. Kodali[3], Baskar Ganapathysubramanian[4,5], and Sumit Chaudhary[5,6]

6.1 Abstract

In order to understand the effect of processing conditions such as spin coating speed and drying rate on the carrier recombination mechanism; three types of poly(3-hexylthiophene) (P3HT):[6,6]-phenyl C61-butyric acid methyl ester (PCBM) bulk heterojunction solar cells (A, B, and C) are fabricated by spin-coating P3HT:PCBM blend at 400, 600 and 1000 rpm for 30, 60, and 60 seconds, obtaining solvent drying time of ~ 40, 7 and 1 minutes respectively. We have shown [1] that higher drying time of the active-layer in device A leads to reduction of sub-bandgap traps by an order of magnitude as compared to fast drying time of the active-layer in device C. Here, we demonstrate that the open circuit voltage and its light intensity dependence are strongly affected by interfacial recombination of carriers at sub-gap defect states. By coupling our experimental results with simulations, we show that at one sun condition, device A has bimolecular recombination as the major loss mechanism which exceeds the interfacial recombination loss by an order of magnitude. However, for the case of device C with high trap density, the

[1] Graduate student, Department of Electrical and Computer Engineering, Iowa State University.
[2] Primary researcher and author.
[3] Graduate student, Department of Mechanical Engineering, Iowa State University.
[4] Assistant Professor, Department of Mechanical Engineering, Iowa State University.
[5] Author for correspondence
[6] Assistant Professor, Department of Electrical and Computer Engineering, Iowa State University.

trap assisted recombination dominates over the intrinsic bimolecular recombination by a factor of 10.

6.2 Introduction

Organic photovoltaics (OPV) have received tremendous attention over the past two decades owing to their promise for low-cost solar-electric conversion, with advantages such as roll-to-roll fabrication on flexible substrates, via solution processing at room-temperature. Photovoltaic active-layers in state-of-the-art devices possess the so called bulk-heterojunction (BHJ) configuration [2], in which the electron donor and acceptor species are intimately mixed with some amount of phase separation at the nanoscale. The phase-separated active-layer blend structure provides a highly nanostructured internal morphology that not only decouples the exciton diffusion length (~10 nm) [3] from the thickness of the active layer, but also increases the heterojunction area available for exciton dissociation. Power conversion efficiencies (PCE) of OPVs have been improving notably over the last six years, owing to the development of new conjugated polymers with tailored energy levels [4-6], and optimizations in materials processing/fabrication conditions [7-11]. Such optimizations include approaches like annealing the active-layer in solvent atmosphere [7,11,12], thermal annealing, post-production thermal annealing after deposition of metal electrode on the active-layer [8], and using high-boiling point solvents as additives [9,10].

Utilizing annealing in solvent-atmosphere (also called solvent-annealing) to control the phase separation, and improve the crystallinity of the donor polymer was one of the cornerstone developments in the field of OPVs – in 2005 – when Li et al. showed that OPV

device performance is strongly dependent on the self-organization in a BHJ blend, which in turn can be varied by controlling the BHJ film growth rate or, in other words, by controlling the time it takes for the wet films to solidify [7]. It was shown that slow growth rate leads to a higher order in the π-conjugated structure of poly(3-hexylthiophene) (P3HT), enhanced optical absorption with more pronounced vibronic shoulders, rougher surface morphology indicative of formation of more ordered structures, and more balanced carrier transport, thus leading to higher PCE than devices based on fast-grown active-layers [7,11]. The enhancement in performance was higher than what could be achieved by thermal-annealing of fast-grown active layer. Using *in situ* photoluminescence and Raman spectroscopy, in conjunction with *ex situ* optical absorption and atomic force microscopy, Miller et al. also showed that solvent annealing leads to de-mixing of phenyl-C61-butyric acid methyl ester (PCBM) and subsequent stacking of P3HT in coplanar conjugated segments [12]. However, the effect of growth-rate on some other crucial device parameters was not revealed. Two such important parameters include defects within the P3HT domains, and carrier recombination rate/mechanism. It is important to elucidate the relationships between growth rate and these parameters for deeper understanding, which can enable systematic defect engineering of OPVs, at levels more sophisticated than the commonplace trial-and-error methodology.

Defects often have a significant influence on the properties of inorganic semiconductors [13], yet their roles in OPVs remain mostly overlooked, let alone the factors that give rise to these defects and methodologies to reduce them. Depending upon the amount of defects and their recombination strength, the losses due to trap-assisted recombination can lower the fill-factor and short-circuit current of OPVs. This was shown

for the case of trap-limited electron transport in BHJ OPV cells with cyano-polyphenylenevinylene derivatives as electron acceptors [14,15]. In a recent publication [1], we have elucidated the dependence between growth-rate and density of sub- band gap defect states in the P3HT phase of P3HT:PCBM devices. Within the set of devices we investigated, we showed that slower growth rate can lead to reduction in the density of sub-band gap defect states by one order of magnitude [1]. We also observed that open circuit voltage (V_{oc}) and its light intensity dependence are strongly affected by interfacial recombination of carriers at sub-gap defect states. In this report, we investigate the effect of growth rates on recombination dynamics in P3HT:PCBM based BHJ OPV cells, and their influence on the device performance. We couple our experimental results and device parameters with a drift-diffusion based device model, and show that at one sun condition, bimolecular recombination is the major loss mechanism for slow-grown films, and exceeds the interfacial trap-assisted recombination loss by an order of magnitude. However, for fast-grown films with high trap density, the trap-assisted recombination dominates over the intrinsic bimolecular recombination by a factor of 10.

6.3 Experimental Details

For device fabrication, a conducting film of poly(3,4-ethylenedioxythiophene) doped with poly(styrenesulfonate) was spin coated on cleaned ITO glass substrate. Subsequently, P3HT:PCBM (17 mg/ml in dichlorobenzene) active layers (A, B, and C) were spin coated (under an argon atmosphere) at 400, 600 and 1000 rpm for 30, 60, and 60 seconds, obtaining solvent evaporation time of ~ 40, 7 and 1 minutes and thicknesses of 350, 220 and 140 nm respectively. The solvent evaporation time after spin coating was

measured by visually inspecting the change in film color when it solidifies from the liquid phase. Al (100 nm) electrode was deposited by thermal evaporation on top of the active layer. To measure photocurrent versus voltage, devices were illuminated using ELH Quartzline lamp operating at 1 sun intensity i.e. 100 mW/cm^2 (calibrated using crystalline Si photodiode). Intensity dependence of the open circuit voltage (V_{oc}) was measured using a set of neutral density filters. Zero field hole mobilities were calculated by fitting the linear region (at high voltage) of $\log(J/V^2)$ versus $V^{1/2}$(where J is current density) plots obtained in dark from completed devices with Pd as top electrode, ensuring hole only transport. At high electric fields, the space charge limited current becomes predominant, such that the effects of traps on the charge transport can be neglected because all the traps are filled (field dependence of mobility was taken into account). The capacitance measurements were performed with a PARSTAT-2273 equipped with a frequency analyzer module. AC oscillating amplitude was as low as 10 mV (rms) to maintain the linearity of response. Measurements were performed at zero bias for $C(f)$, and at 100 Hz for $C(V)$ analysis, always in dark conditions and at room temperature.

6.4 Results and discussion

(a) A Note on Recombination Mechanisms in OPVs

In OPVs with both trap-free electron and hole transport in the acceptor and donor, respectively, the main recombination mechanism for the free charge carriers is bimolecular recombination. The bimolecular recombination rate is given in this case by

$$R_{Bimolecular} = \gamma\left(np - n_i p_i\right) \tag{1}$$

Where $n(p)$ is the free electron (hole) density, $n_i(p_i)$ is the intrinsic electron (hole) density, and γ is the Langevin recombination constant [16]. A wide range of publications have reported that the dominant recombination mechanism in organic solar cells is bimolecular. These studies were based on different techniques in the time and frequency regime [17,18]. The authors of these studies share the opinion that non-geminate bimolecular recombination is a strongly limiting factor in organic solar cells.

However, there exists a contradictory school of thought that suggests recombination at interface states (defects) rather than at charge transfer excitons, is the governing mechanism that determines the shape of the solar cell characteristics for the BHJ solar cell [19]. When defect states are present in the electron donor, the dissociation of bound pairs at the interface leads to free carriers, but now part of the holes can be trapped. For the holes trapped close to the interface, there is a probability of recombination with the free electrons in the acceptor, leading to loss of both carriers. The trap-assisted recombination rate is given by the Shockley-Read-Hall (SRH) equation

$$R_{Trap-assisted} = \frac{C_n C_p N_t \left(pn - p_1 n_1\right)}{\left[C_n \left(n + n_1\right) + Cp\left(p + p_1\right)\right]} \tag{2}$$

Where C_n and C_p are the capture coefficients of electrons and holes, respectively, N_t is the density of hole traps, n and p are the electron density in the conduction band and the hole density in valence band, and $p_1 n_1 = N_c N_v \exp[-(E_c - E_v)/kT] = n_i^2$, with n_i the intrinsic carrier concentration in the sample [14,15]. This trap-assisted recombination process adds to the Langevin (bimolecular) recombination, contributing to loss mechanisms in a BHJ OPV.

(b) Experimental-Numerical Results

To investigate the effect of growth rate on recombination rates/mechanisms, we fabricated three types of P3HT:PCBM BHJ cells – A, B, and C – wherein, the active layers were spin coated at 400, 600 and 1000 rpm for 30, 60 and 60 seconds, obtaining solvent evaporation times of ~ 40, 7, and 1 minutes and thicknesses of 350, 220 and 140 nm respectively (see experimental section for details). The solvent evaporation time after spin coating was measured by visually inspecting the change in film color when it solidifies from the liquid phase. We measured current-voltage characteristics under illumination, dependence of V_{oc} on the light intensity, hole mobilities from hole-only diodes, and electron mobilities from electron-only diodes (see experimental section for details). In order to simulate the photocurrent and correlate it with defect density of the devices we used a model that included drift and diffusion [20,21], the field- and temperature-dependent generation rate *G(E,T)*, the carrier mobilities, and the trap density. The model also included thickness dependence of maximum generation rate G_{max}, which for thicker samples has a lower rate because it represents an average value over the sample thickness. In our recent publication [1], using capacitance-voltage and capacitance-frequency measurements, the total density of traps was found to be $3.3\times10^{21}m^{-3}$, $5.2\times10^{21}\ m^{-3}$ and $2.1\times10^{22}m^{-3}$ for devices A, B and C, respectively. These traps have been shown to only belong to the P3HT phase, as such behavior was not exhibited at all by the devices containing only PCBM [22]. The measured hole mobilities were 6.2×10^{-4},1.34×10^{-4}, and $1.85\times10^{-5}cm^2\ V^{-1}\ s^{-1}$, whereas electron mobilities were 8.2×10^{-4}, 1.0×10^{-4}, and $1.0\times10^{-5}cm^2V^{-1}s^{-1}$ for devices A, B and C, respectively. As a step towards achieving good agreement between experiment and simulation, we also investigated the intensity dependence of V_{oc}. In case of Langevin

(bimolecular) recombination of free carriers being the only loss mechanism, it has been shown that the V_{oc} of the OPVs follow [23]

$$V_{oc} = \frac{E_{gap}}{q} - \frac{kT}{q} \ln\left[\frac{(1-P)\gamma N_c^{\,2}}{PG}\right]$$

where E_{gap} is the energy difference between the HOMO of the electron donor and the LUMO of the electron acceptor, q is the elementary charge, k the Boltzmann constant, T the temperature, P is the dissociation probability of the electron-hole pairs into free carriers, γ is the recombination constant, N_c is the density of states in the conduction band, and G is the generation rate of electron-hole pairs. Since G is the only term directly proportional with the light intensity (with P and γ not depending on it), this formula contains the dependence of the V_{oc} on the light intensity. Therefore, the slope $S = (kT/q)$ of the V_{oc} versus the natural logarithm of the light intensity is predicted by the formula and has been experimentally verified on various PPV:fullerene based devices [23]. However, for devices A, B and C, as shown in Figure 6.1, the experimental data showed a steeper dependence of V_{oc} on the light intensity with S = 1.1, 1.4 and 1.9 times (kT/q), respectively (calculated from the linear fit), whereas the simulated V_{oc} from the numerical device model with the parameters mentioned above had the expected kT/q slope.

Apparently, in our device model there is still a process missing, which leads to discrepancy between measured and calculated V_{oc}. It is known that at $V_{oc,}$ there is no current extraction and all the photogenerated charge carriers recombine [20]. Therefore, the properties of the solar cell at V_{oc} are strongly dependent on the recombination processes. A slope of 1.5(kT/q) has been measured for all-polymer solar cells with electron traps contained in the acceptor phase [15]. This deviation has been explained by including SRH

recombination at the electron donor-acceptor interface in the device model developed for BHJ solar cells [14,15,20]. The trap-assisted interfacial recombination competes with the Langevin one, thereby the slope of V_{oc} versus natural logarithm of the light intensity increases with the strength of the trap-assisted recombination. Consequently, the dependence of V_{oc} on light intensity is more enhanced. Such a trap-assisted recombination path has not been included in the device model so far, because in the earlier studies on P3HT:PCBM OPVs, trap density was considered negligible and Langevin recombination was assumed as dominant mechanism [17,18].

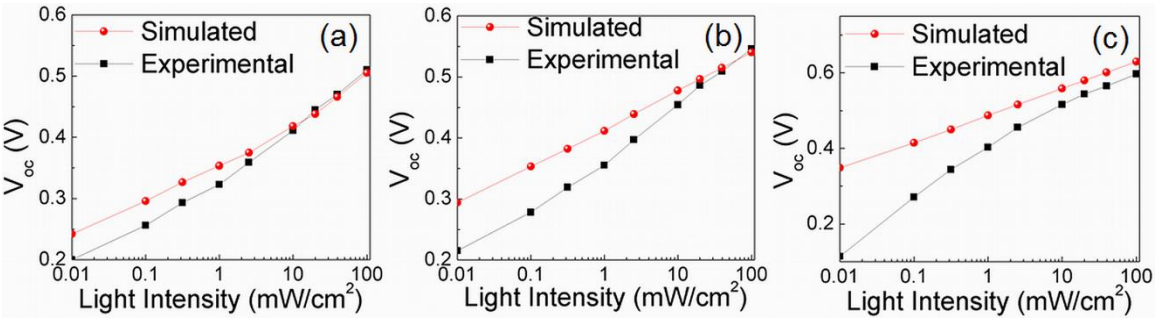

Figure 6.1: Experimental (squares) V_{oc} versus light intensity of P3HT:PCBM devices (a) A, (b) B, and (c) C; and calculation (circles) with parameters used to calculate the *J-V* characteristics in case of Langevin recombination.

Including the trap-assisted recombination in the device model improved the agreement between the simulations and experiments. The calculated light-intensity dependence of the V_{oc} is in agreement with the experiments, as shown in Figure 6.2. To fit calculation with experimental measurement of V_{oc}versus light intensity, capture coefficients C_n=C_p= 6 × 10^{-16} m^3 s^{-1} were used. In this case, both Langevin and SRH recombination mechanisms play a role in P3HT:PCBM cell. In the case of fast-grown active-layer (device C), with one order of magnitude higher trap density in P3HT and steeper V_{oc} dependence on light intensity than slow-grown active-layer (device A), it is expected that the trap-limited

recombination is stronger.The faster decay of V_{oc} for the trap-limited fast-grown device C is a direct outcome of the fact that the presence of holes in trap levels above the HOMO of the P3HT raises the hole quasi-Fermi level.

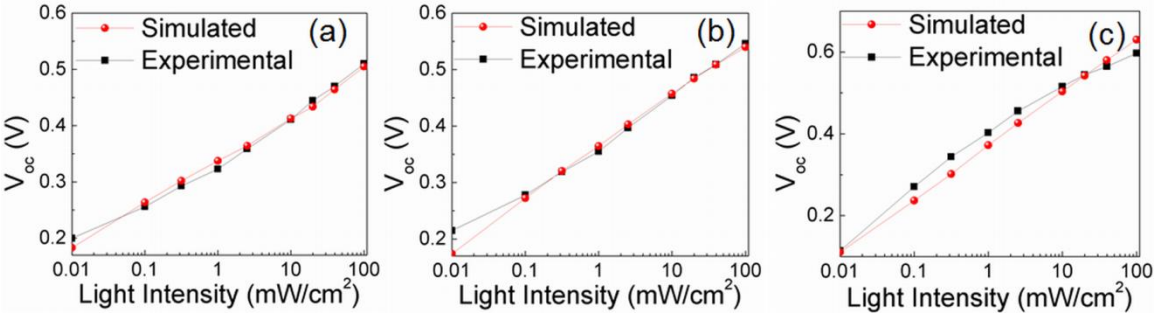

Figure 6.2: V_{oc} versus light intensity of P3HT:PCBM devices (a) A, (b) B, and (c) C; and calculation (circles) using mobility values derived from transport measurements and the capture coefficients for electrons and holes C_n=C_p=6 × 10^{-16} m^3 s^{-1}.

The photocurrent of devices A, B and C were recalculated after incorporating SRH recombination in the device model, as shown in Figure 6.3. The good agreement between measured and simulated photocurrent shows that the same framework [20], after including SRH recombination can describe the trap-limited current-voltage characteristics of P3HT:PCBM OPV devices.

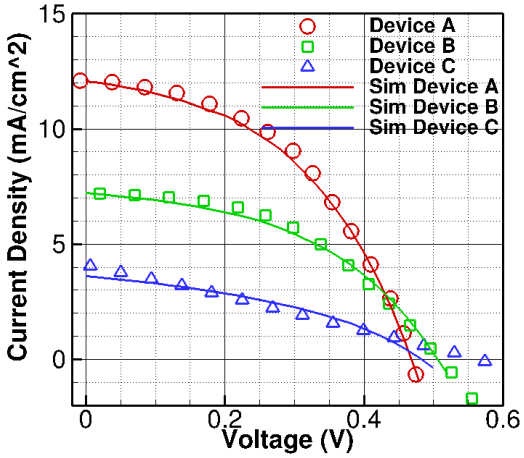

Figure 6.3: Measured (open symbols) current-voltage characteristics of P3HT:PCBM OPV devices A (red), B (green), and C (blue), with different growth conditions. The solid lines are the calculated currents with maximum generation rates G_{max} = 5×10^{28} m^{-3} s^{-1}, 3.5×10^{27} m^{-3} s^{-1}, and 8×10^{26} m^{-3} $s^{-1}$for

deives A, B and C, respectively, an e-h pair distance a= 2 nm, a decay rate k_f = 1.5×10^2 s^{-1}, carrier mobilities derived from transport measurements, the electron trapping parameters N_t=3.3×10^{21} m^{-3}, 5.2×10^{21} m^{-3} and 2.1×10^{22} m^{-3} for devices A, B and C, respectively, and the capture coefficients for electrons and holes C_n= C_p= 6 × 10^{-16} m^3 s^{-1}.

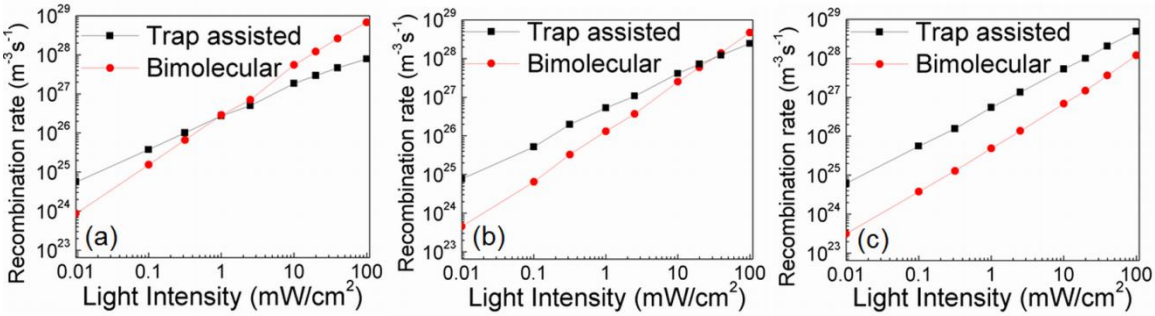

Figure 6.4: Rate of trap-assisted recombination (squares) and of Langevin (bimolecular) recombination (circles) as a function of light intensity, for devices (a) A, (b) B, and (c) C with different growth conditions. The recombination rates were calculated for the parameters used to calculate the current under illumination at 100 mW cm^{-2}, with a field dependent generation rate *G*.

To understand the device operation it is imperative to know which recombination mechanism is responsible for the losses in the solar cell. As shown in Figure 6.4 (a) and (b), in devices A and B the strength of the Langevin recombination is clearly dominant compared to the trap-limited SRH recombination at 100 mW cm^{-2} (one sun condition). This is another reason why the inclusion of SRH recombination was not considered obligatory in earlier models [17,18] of P3HT:PCBM OPVs, and owes to low-enough trap density in slow grown films. At lower light intensities (< 1 and 40 mW cm^{-2} for devices A and B respectively), trap-assisted recombination is more dominant than Langevin recombination. This is because, with increasing light intensity, leading to an enhanced carrier density in devices, the Langevin recombination becomes quadratically stronger (~*np*) and eventually dominates the trap-assisted recombination [~*p*(*n*)]. For fast grown device C, with such a strong dependence of V_{oc} on light intensity and high defect density (2.1×10^{2}m^{-3}), the trap-assisted recombination dominates over the Langevin recombination. As it can be seen in

Figure 6.4(c), this is true at all light intensities measured. This increased amount of trap-assisted recombination in trap-limited device C also leads to the observed reduction of the fill factor as seen in current-voltage characteristics. Furthermore, the additional loss of free carriers due to stronger recombination results in reduction of the photocurrent in device C (Figure 6.3).

6.5 Conclusions

In conclusion, we have shown that solvent-annealing enabled slow-growth of P3HT:PCBM films assists the formation of self-organized ordered structure in the P3HT:PCBM blend system, diminishing morphological defects in P3HT chains. Fast-growth, however, results in an order of magnitude higher trap density owing to the structural defects (twists and bends) in P3HT chains. For slow-grown devices, the traps present in P3HT phase contribute to the SRH recombination losses of system at low light intensities. The trap-assisted recombination dominates the super-linear light-intensity dependence of the V_{oc} observed for these OPVs. The recombination rate calculations reveal that trap-assisted recombination can dominate over the Langevin recombination at one sun condition for films with high enough trap density. The enhanced recombination losses also lower the fill factor and short circuit current. Therefore, it becomes imperative to design materials without traps to defect-engineer the OPVs for achieving higher performance. It remains to be seen whether solvent-annealing has an advantage over thermal annealing in terms of reducing traps and trap-assisted recombination, and is the subject of our immediate research.

6.6 Acknowledgements

KSN and SC thank state of Iowa's Office of Energy Independence for supporting this work through Iowa Power fund.

6.7 References

[1] K. S. Nalwa, R. C. Mahadevapuram, S. Chaudhary, *Applied Physics Letters***2011**, *98*, 093306.

[2] G. Yu, J. Gao, J. C. Hummelen, F. Wudl, A. J. Heeger, *Science***1995**, *270*, 1789.

[3] P. E. Shaw, A. Ruseckas, I. D. W. Samuel, *Advanced Materials***2008**, *20*, 3516.

[4] H. Y. Chen, J. H. Hou, S. Q. Zhang, Y. Y. Liang, G. W. Yang, Y. Yang, L. P. Yu, Y. Wu, G. Li, *Nature Photonics***2009**, *3*, 649.

[5] Y. Y. Liang, Z. Xu, J. B. Xia, S. T. Tsai, Y. Wu, G. Li, C. Ray, L. P. Yu, *Advanced Materials***2010**, *22*, E135.

[6] S. H. Park, A. Roy, S. Beaupre, S. Cho, N. Coates, J. S. Moon, D. Moses, M. Leclerc, K. Lee, A. J. Heeger, *Nature Photonics***2009**, *3*, 297.

[7] G. Li, V. Shrotriya, J. S. Huang, Y. Yao, T. Moriarty, K. Emery, Y. Yang, *Nature Materials***2005**, *4*, 864.

[8] W. L. Ma, C. Y. Yang, X. Gong, K. Lee, A. J. Heeger, *Advanced Functional Materials***2005**, *15*, 1617.

[9] J. Peet, J. Y. Kim, N. E. Coates, W. L. Ma, D. Moses, A. J. Heeger, G. C. Bazan, *Nature Materials***2007**, *6*, 497.

[10] Y. Yao, J. H. Hou, Z. Xu, G. Li, Y. Yang, *Advanced Functional Materials***2008**, *18*, 1783.

[11] G. Li, Y. Yao, H. Yang, V. Shrotriya, G. Yang, Y. Yang, *Advanced Functional Materials***2007**, *17*, 1636.

[12] S. Miller, G. Fanchini, Y. Y. Lin, C. Li, C. W. Chen, W. F. Su, M. Chhowalla, *Journal of Materials Chemistry***2008**, *18*, 306.

[13] P. T. Landsberg, *Nature***1978**, *275*, 270.

[14] M. M. Mandoc, F. B. Kooistra, J. C. Hummelen, B. d. Boer, P. W. M. Blom, *Applied Physics Letters***2007**, *91*, 263505.

[15] M. M. Mandoc, W. Veurman, L. J. A. Koster, B. de Boer, P. W. M. Blom, *Advanced Functional Materials***2007**, *17*, 2167.

[16] P. Langevin, *Annales De ChimieEt De Physique***1903**, *28*, 433.

[17] A. Foertig, A. Baumann, D. Rauh, V. Dyakonov, C. Deibel, *Applied Physics Letters***2009**, *95*.

[18] A. Pivrikas, G. Juska, A. J. Mozer, M. Scharber, K. Arlauskas, N. S. Sariciftci, H. Stubb, R. Osterbacka, *Physical Review Letters***2005**, *94*.

[19] R. A. Street, M. Schoendorf, *Physical Review B***2010**, *81*.

[20] L. J. A. Koster, E. C. P. Smits, V. D. Mihailetchi, P. W. M. Blom, *Physical Review B***2005**, *72*.

[21] H. K. Kodali, Ganapathysubramanian, *Journal of Computational Physics***(submitted)**.

[22] P. P. Boix, G. Garcia-Belmonte, U. Munecas, M. Neophytou, C. Waldauf, R. Pacios, *Applied Physics Letters***2009**, *95*.

[23] L. J. A. Koster, V. D. Mihailetchi, R. Ramaker, P. W. M. Blom, *Applied Physics Letters***2005**, *86*.

CHAPTER 7. A facile route towards realization of higher efficiency organic solar cells by addition of ferroelectric polymer

Modified from a paper submitted to *Nature Materials*

Kanwar S. Nalwa[1,2], John Carr[1], Rakesh C. Mahadevapuram[3], and Sumit Chaudhary[4,5]

7.1 Abstract

It has been estimated that non-radiative recombination accounts nearly 50% of efficiency loss in modern OPVs. Generally, an external bias is required to collect all the photogenerated charges and thus prevent their recombination. The motivation is to induce additional electric field in otherwise low mobility conjugated polymer based active layer by incorporating ferroelectric dipoles. This is expected to facilitate singlet exciton dissociation in polymer matrix and impede charge transfer exciton (CTE) recombination at polymer:fullerene interface. For the first time, it is shown that the addition of ferroelectric dipoles to modern bulk heterojunction (BHJ) can significantly improve exciton dissociation, resulting in a ~33% enhancement of overall solar cell efficiency. It is found, upon the addition of poly(vinylidenefluoride-co-trifluoroethylene) (PVDF-TrFE), internal quantum efficiency approached 100% for some wavelengths. This result is indicative of complete exciton harvesting at these photon energies and implies that nearly every singlet exciton as well as nearly every charge transfer exciton are able to break their Columbic bond and separate. The devices also exhibit the unique ferroelectric-photovoltaic effect with polarization-controlled power conversion efficiency.

---

[1] Graduate student, Department of Electrical and Computer Engineering, Iowa State University.
[2] Primary researcher and author.
[3] Graduate student, Department of Materials Science and Engineering, Iowa State University
[4] Author for correspondence
[5] Assistant Professor, Department of Electrical and Computer Engineering, Iowa State University

7.2 Introduction

In the search for sustainable, high-performing green-energy, organic photovoltaics (OPVs) have become prime contenders within the last decade. OPVs have gained much attention as they offer the realization of low-cost solar energy conversion, with advantages that include mechanical flexibility, light weights, ease of processing and the ability for large area roll-to-roll production. A revolutionary development in organic photovoltaics came in the mid-1990s with the introduction of a dispersed bulk heterojunction (BHJ) device, where an electron accepting and an electron donating material are blended together at a phase separation similar to the exciton diffusion length. Although these blend devices have a Shockley-Queisser theoretical efficiency of $\eta_{SQ}\approx21\%$ [1], single-junction OPVs have achieved the highest power conversion efficiencies to date; exceeding 7%. Device efficiency has been tripled during the last six years, owing to the development of new conjugated polymers with tailored energy levels [2-4] and optimizations in materials processing and fabrication conditions [5-10]. Such optimizations include approaches like annealing the active-layer in solvent atmosphere [5,6,10], post-production thermal annealing after deposition of metal electrode on the active-layer [7] and using high-boiling point solvents as additives [8,9]. However, in their current state, these devices still require further improvement for most (if not all) practical application.

Although many facets of OPVs would benefit from further development, the recovery of the following four significant energy losses could make 10%+ efficient OPVs realizable in near future. (i) Meager light absorption: in contrast to their inorganic counterparts, most organic absorption fails to increase monotonically and typically decreases at higher energies. Plagued further by insufficient trapping schemes, parasitic

losses from absorption within a non-active material and finite film thicknesses, optical losses may account for up to ~38% of the efficiency reduction [1]. (ii) Poor carrier mobilities: with mobilities orders of magnitude smaller than inorganic materials, film thickness must be carefully controlled to ensure complete photogenerated-carrier collection. Thus, a balancing act between absorption and carrier drift length must be played to lower the probability for charge recombination. Increasing drift length of the carriers can reduce efficiency losses by up to ~17% [1]. (iii) Singlet exciton (SE) recombination: when a film is excited from the absorption of a photon, the Coulombic binding between the highest occupied molecular orbital (HOMO) residing electron and the lowest occupied molecular orbital (LUMO) residing hole gives rise to a quasi-particle called an exciton (typically these quasi-particles reside in the singlet quantum state) [11]. Due to the relatively low permittivity of organic materials, the thermal energy available at room temperature is not sufficient to break the excitonic binding. Therefore, the SE must reach a donor/acceptor quenching interface within its ~10nm diffusion length in order to separate. Radiative SE recombination during this diffusion process accounts for nearly 12% of efficiency loss in modern OPVs [1]. (iv) Deficient charge transfer exciton (CTE) quenching: if the said SE reaches a quenching interface, it decays to form a geminate electron-hole pair (the CTE) directly after the photoinduced electron transfer. This CTE must then be dissociated to form free carriers which can then (and only then) contribute to photocurrent. Geminate recombination of CTEs aggravates this process when the dissociation-driving electric field is small, leading to a fundamental efficiency loss. Further, even if the geminate CTE ionizes with high probably, the loss of free carriers induced by non-geminate recombination further reduces the output power of the OPV. It has been estimated that an efficiency reduction

exceeding 32% can be attributed to non-radiative recombination (including both geminate and non-geminate recombination) [1].

In this work, it is hypothesized that if a ferroelectric (FE) copolymer is embedded into the photoactive layer of OPV devices, it would be possible to alleviate one or more of the above-mentioned limitations. Two driving forces seed these enhancements. First, the mismatch of host material's refractive index and the embedded FE's refractive index generates scattering sites; advantageous for light trapping and absorption [12]. Absorption is a function of path length, where the amount of absorption increases with the overall distance traversed by a light wave within a material. Thus, by introducing scattering sites, the path length, and thereby the absorption, is enlarged within the active layer; especially important for films thinned to induce better charge collection.

Second, the permanent electrical polarization of the embedded FE dipoles generates a localized improvement to the internal electric field in the active layer; beneficial for both carrier drift and exciton dissociation. The carrier drift length is a product of mobility, lifetime and electric field. Thus, an enlargement of drift length can be made by a localized FE field; an important enhancement to low mobility materials [13,14] and/or films thickened to induce better absorption. Further, the modified Braun model [15] (Eq. (1)) quantitatively shows that, for an exciton in the presence of an electric field ($<10^5$ V/cm), the probability of ionization is a strong function of field strength (E) and binding energy (E_B).

$$\varphi(E) = \frac{1}{1+\frac{\omega_0}{\mathrm{F}(E)}e^{E_B/kT}} \tag{1}$$

Where $\mathrm{F}(E)$ is a function of $e^3E/8\pi\varepsilon_0\varepsilon\, k^2T^2$. It has been estimated that the binding energies of the SE state and the intermediate CTE state are in the range of 0.4-0.7eV and

0.2-0.3 eV respectively [11,16]. Both energies are an order of magnitude higher than kT at room temperature (~0.026 eV), making the exponential term ($e^{E_B/kT}$) in Eq. (1) very large. This shows that an increase of the F(*E*) term (by incrementing the electric field) is needed for a higher probability of ionization. This model is supported by previous studies which have shown that, for polymer based BHJ OPVs, photocurrent saturation takes place only under a large external biasing (>10 V reverse bias) [17,18]. This implies that an internal field of ~50-70 V/μm is needed for complete exciton fission and shows that the field generated by the difference in electrode work-function (typically 1-10 V/μm) is grossly insufficient. Thus, the amplification of OPV devices' internal field (e.g. by the incorporation of FE dipoles) may be a crucial tool for realizing 10%+ efficient organic solar cells.

Although there are a variety of inorganic and organic ferroelectric materials, the ferroelectric co-polymer poly(vinylidenefluoride-co-trifluoroethylene) (PVDF-TrFE) is utilized for our investigation, owing to its solution processability and its existence in an all-trans β phase at room temperature (β phase that exhibits a net dipole moment [19]). Current literature shows the PVDF-TrFE co-polymer exhibits a high dielectric of ~11, which when mixed with low dielectric organic materials (n≈2) would generate numerous optical scattering sites, resulting in an improved absorption within the active layer. Further, using the classical dipole-field model presented in Eq. (2) [20],

$$E = \frac{4\pi}{\varepsilon}\sigma f \tag{2}$$

where ϵ is the relative permittivity of FE co-polymer, σ is the pyroinduced surface charge density (~6 μC/cm^2 for PVDF-TrFE) and f is the volume fraction occupied by the dipoles,

we have estimated a theoretical enhancement to the device's internal field in the range of ~$8*10^3*f$ V/μm. Thus, even for a small addition of PVDF-TrFE insulator, a large increase to the internal field can be achieved without significantly affecting the conductivity of the photoactive layer. We anticipate a volume fraction of ~.03 (corresponding to an electric field of ~ 240 V/μm) to be sufficient for complete exciton dissociation (SE as well as CTE).

We have used two different OPV structures (BHJ and bilayer) based on a poly(3-hexylthiophene): [6,6]-phenyl-C61-butyric acid methyl ester (P3HT:PCBM) material system to assess the performance of the co-polymer additive. We used this material system as it is very well studied, has produced some of the most efficient OPVs to date and serves as a good standard for performance comparison. In this work, it is shown that the addition of ferroelectric dipoles to the bulk of modern BHJ and bilayer organic photovoltaic devices can significantly improve performance, resulting in a ~48% (BHJ device over device) to ~62% (bilayer device over device) enhancement of overall solar cell efficiency.

7.3 Experimental Details

(a) OPV fabrication

Anode Preparation: Indium-doped tin oxide (ITO; Delta Technologies) slides were then treated by consecutive 5 minute sonications in four solutions: (i) isopropyl and acetone (50:50 v/v), (ii) detergent, (iii) ethanol and methanol (50:50 v/v), and (iv) deionized water. The ITO substrates were then blown dry with nitrogen and treated with air plasma (Harrick Scientifc) for 5 min. A poly(ethylenedioxythiophene):poly(styrenesulfonic acid)

(PEDOT:PSS; H C Stark) film was spin-coated (3,000 RPM for 60 sec) onto the treated substrates and the casted films were annealed on a digital hot plate at 120 ºC for 10 min.

Fabrication of BHJ OPVs: Three solutions were made of PVDF-TrFE copolymer (70:30 mol%) in Tetrahydrofuran (THF) with concentrations 2 mg/ml, 4 mg/ml and 8 mg/ml. The donor-acceptor blend with 1:1 weight ratio and 13.33 mg/ml concentration of P3HT in ortho-Dichlorobenzene (ODCB) was used. 0.25 ml of pure THF and 3 PVDF solutions (2, 4 and 8 mg/ml) in THF were mixed with 0.75 ml of blend solution to get 4 solutions with 0, 5, 10 and 20% PVDF by weight of P3HT. This allowed to have final concentration of P3HT:PCBM same (10 mg/ml) in all the 4 solutions, with each solution having same ratio of THF and ODCB solvents (1:3) to ensure appropriate comparison. The mixing of solvents had to be done because PVDF does not dissolve in ODCB and hence was dissolved in THF and then mixed with the blend solution in 3 different concentrations. The solutions were magnetically stirred for several hours at 45ºC. The solutions were then spin coated at 600 rpm for 40 s over PEDOT:PSS layer and dried at room temperature under a petri dish. Finally, Al (100 nm) cathode was formed by thermal evaporation on top of the active layer, and devices were annealed at 150^{o}C for 2 minutes to improve the crystallinity of P3HT and PVDF phases.

Fabrication of Bilayer OPVs: First, two P3HT solutions (PS1 and PS2) were prepared (for subsequent use in making the film solutions) in an argon atmosphere: PS1 consisted of P3HT in ODCB at a concentration of 26.67 mg/mL and PS2 comprised PVDF in THF at a concentration of 8 mg/mL. Next, four film solutions (FS1, FS2, FS3 and FS4) were made (for subsequent use in the casting of device films). FS1 consisted 0.75 mL of PS1 mixed with 0.25 mL of PS2 to give a P3HT(ODCB):PVDF(THF) ratio of 20:2. FS2

comprised of 0.75 mL of PS1 mixed with 0.25 mL THF to give 20 mg/mL P3HT:(ODCB+THF). FS3 contained PCBM in Dicholoromethane at a concentration of 10 mg/mL. FS4 included PVDF in Dimethylformamide (DMF) at a concentration of 2 mg/mL. FS1/FS2, FS3 and FS4 were heated to 45ºC, 0ºC and 65ºC respectively and magnetically stirred for several hours. After being cooled to room temperature, the P3HT solutions (FS1 and FS2) were then filtered and spin-cast at 1000 RPM for 90 sec onto the dried PEDOT:PSS films, producing a film thickness of ~115 nm. For the three devices presented here, (i) the control device, (ii) the mixture device and (iii) the interface device, FS2, FS1 and FS2 solutions were cast respectively. The films were then covered with a petri dish and allowed to dry for ≥ 10 min. FS4 was then filtered and spun at 4,000 RPM for 60 sec onto the P3HT:(ODCB+THF) layer of the interface device, producing an interfacial film thickness of <10 nm. This film was then annealed at 150 ºC for 1 min. The device was again covered and the interface film was allowed to cool. FS3 was then filtered and spin-cast (4,000 RPM for 10 sec) to a thickness of ~34 nm onto all three devices and was immediately annealed at 150 ºC for 1 min. After allowing the PCBM film to dry, a ~100 nm thick Al cathode was evaporated onto all devices at a rate < 5 Å/s.

(b) Photovoltaic characterization

I-V characterization was done using ELH Quartzline halogen lamp, the intensity of which was calibrated using a crystalline Si cell with a KG-5 filter. EQE measurements were also done using this lamp and a monochromator with a lock-in amplifier to eliminate background noise. The reference was a calibrated Si photodiode with known EQE spectra. To calculate internal quantum efficiency of the devices BHJ devices, all the films for

absorption measurement were spun cast on glass substrates. The absorption spectra were measured by a Varian Cary 5000 UV-Vis-NIR spectrophotometer.

(c) Time Resolved Experiments

Excited-state PL-lifetime measurements were performed using the TCSPC set-up described elsewhere. Briefly, a homebuilt mode-locked Ti:sapphire oscillator pumped by a Nd:VO_4 laser (Millennia, Spectra Physics) producing femtosecond pulses tunable from 780 to 900 nm with a repetition rate of 82 MHz was used as the laser source. The fundamental wavelength at 814 nm from the Ti:sapphire oscillator was modulated by a Pockels cell (Model 350-160, Conoptics Inc.) to reduce the repetition rate to approximately 8.8 MHz and was subsequently frequency-doubled by using a harmonic generator (Model TP-2000B, U-Oplaz Technologies). The resulting blue light, which had a central wavelength of 407 nm, provided the excitation source, and emission ($\lambda >$ 505 nm) was collected in front face geometry from solid films using appropriate filters to eliminate possible interference from scattered light. The full width at half-maximum (FWHM) of the instrument response function was ~35 ps. All of the measurements were made in a 3.33 ns time window with a total of 1024 channels. A total of 65530 counts were collected at the peak channel for all of the lifetime measurements.

7.4 Results and discussion

We first investigated the effects of adding the ferroelectric PVDF-TrFE to the active layer of a P3HT:PCBM-based BHJ system. Four P3HT:PCBM devices were fabricated, each with different ratio of the PVDF-TrFE additive (0%, 5%, 10%, and 20% PVDF-TrFE

by weight of P3HT). The final concentration of P3HT:PCBM was equivalent (10 mg/ml) in all four solutions, with each solution having same ratio of THF and ODCB solvents (1:3) for appropriate comparisons. On completing the devices, a short post-production anneal at 150^{o}C was done to improve the crystallinity of the P3HT and PVDF-TrFE phases. Figure 7.1(a) and Table 7.1 summarize the J-V characteristics the tri-blend (P3HT:PCBM:PVDF-TrFE) devices. Analysis indicates that short circuit current (J_{sc}), open circuit voltage (V_{oc}) and fill factor (FF) increase upon the addition of PVDF-TrFE, up to mass ratios as high as 10%. We believe this improvement in performance to be a consequence of enhancements to one or more of the afore-discussed PV-effect-governing processes – namely: light absorption, exciton dissociation and/or charge transport. In the subsequent discussion, further characterization is presentedto pinpoint the origins of these improvements and rule out unlikely processes.

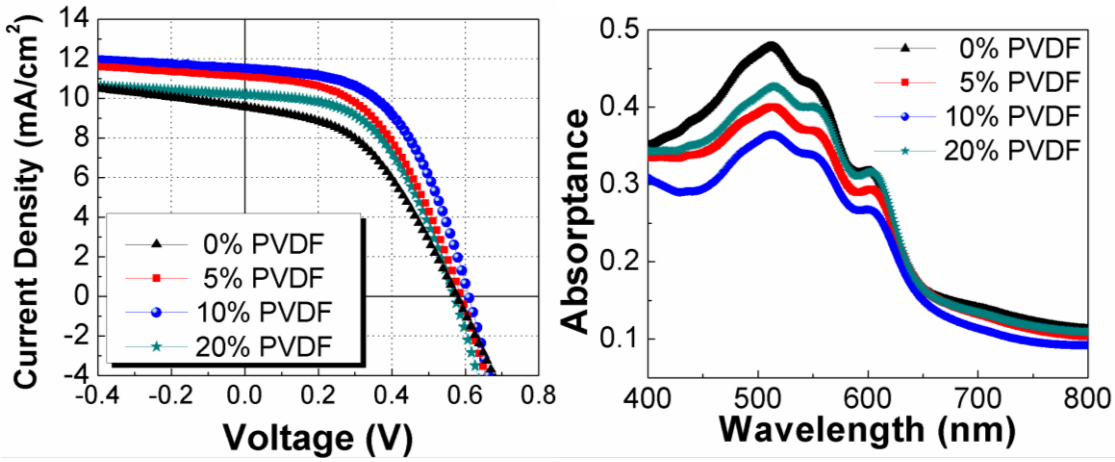

Figure 7.1: Effect of PVDF-TrFE concentration on the performance of the OPVs in terms of (a) photocurrent density vs voltage curves and (b) absorption of the photoactive blend layer.

Using the subsequent arguments, we claim that PV enhancements (over the control device) observed in the 5 and 10% tri-blend devices are not related to optical effects, but are more likely a result of enhanced charge transport processes and/or improved exciton

dissociation. As shown in Figure 7.1(a), there seems to be an optimal PVDF-TrFE concentration for achieving maximum PV enhancements. Specifically, although the 5% tri-blend showed improvement over the control (0% PVDF-TrFE) and the 10% tri-blend showed improvement over the 5% device, the 20% tri-blend failed to push the improvements further. The 20% tri-blend did exhibit improvements over the control device; however, J_{sc}, V_{oc} and FF were slightly decreased when compared to the 10% mixture. At the 20 wt% concentration we suspect an aggregation effect of the nanodipoles begins to dominate. The inter-dipole interaction energy increases with concentration leading to a clustering effect in which the electrostatic field enhancements brought on by the ferroelectric are shielded (further details will be presented in the subsequent discussion), causing lower device performance of 20% relative to 10% tri-blend device. This aggregation effect of the 20% tri-blend device can also be seen as increased absorption (compared to the 10% device) in Figure 7.1(b). This increase can be ascribed to the scattering of light in the active layer due to refractive index (n) mismatch between the PVDF-TrFE agglomerates ($n \approx 10$ and size ~100-200 nm: refer to appendix Figure 7.9) and surrounding P3HT:PCBM blend ($n \approx 2$). The scattering increases the path length of light in the active blend, thereby increasing absorption. As shown in Figure 7.1(b), the 5% and 10% tri-blend films presented lower visible light absorption as compared to the control and 20% tri-blend films. These concentrations have some fraction of their active layer occupied by the wide band gap PVDF-TrFE dipoles, which do not absorb visible light and thereby decrease overall absorption. Further, due to lower concentrations (5 and 10 wt%) of the ferroelectric additive, aggregation is minimal and scattering effects are unappreciable.

Table 7.1: Effect of PVDF-TrFE concentration on the photovoltaic performance of the OPVs.

	$J_{sc}(mA/cm^2)$	$V_{oc}(V)$	FF	Efficiency
0% PVDF	9.61	0.58	45.59	2.54%
5% PVDF	11.10	0.59	49.66	3.25%
10% PVDF	11.58	0.61	53.30	3.77%
20% PVDF	10.26	0.57	51.91	3.04%

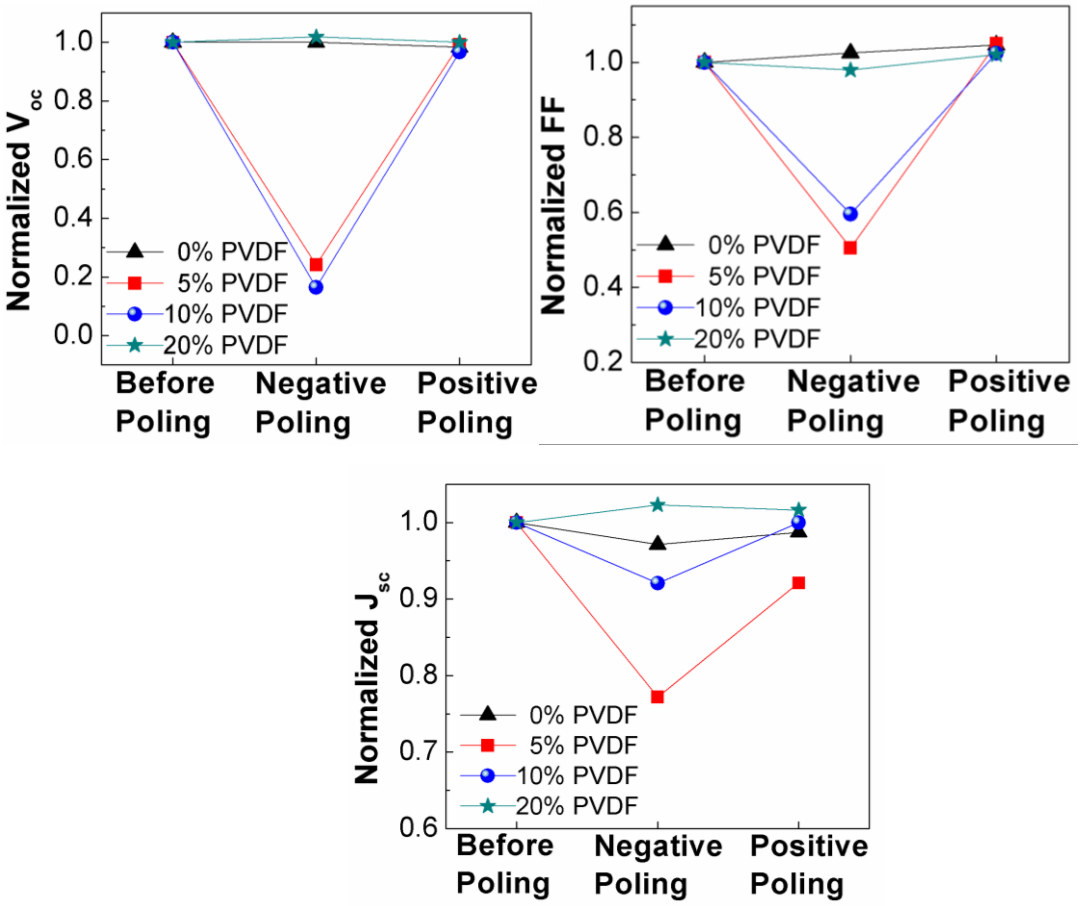

Figure 7.2: Effect of poling on (a) open circuit voltage, (b) short circuit current, and (c) fill factor of tri-blend OPV devices.

Using the model presented in Eq (2), we estimate internal field increments to be in the range of ~150 V/μm, ~300 V/μm and ~600 V/μm for the 5%, 10% and 20% tri-blend

devices respectively. In order to investigate possible dipole-field-induced enhancements to the active layer charge transport, J-V characteristics were measured after electrically poling the OPV devices (Figure 7.2). A 20 V pulse of 10 ms duration was applied on the ITO electrode with both positive and negative polarities and performance characteristics were subsequently measured. The applied field (~ ±110 MV/m) correlates well with the PVDF-TrFE polarization vs. electric field data available in current literature, where a coercive field of ~50MV/m and a saturation field (i.e 100% polarization) of ~100MV/m are generally reported [21,22]. No changes were observed in the OPVs without PVDF-TrFE after applying a pulse of either polarity. In contrast, the V_{oc} and FF in both the 5% and 10% tri-blend devices could be readily altered by electrical poling. A negative 20 V pulse significantly reduced V_{oc} and FF, while a subsequent positive poling was able to recover the original performance. It is expected that -20V pulse induces strong dipole alignment from the Aluminum (Al) to the ITO layer of the device, which produces an internal dipole field that opposes the built-in field (generated by difference of work-function of electrodes) and limits drift transport. A lower drift field in the device induces loss of carriers by CTE recombination, which in turn reduces the quasi-fermi level difference between electrons and holes, resulting in lower V_{oc} of negatively-poled 5% and 10%tri-blend devices [23]. The non-radiative CTE recombination of free carriers in negatively poled 5% and 10% tri-blend devices, of course, reduces the photocurrent, lowering the performance even further. As shown in Figure 7.2, after the application of a positive 20 V pulse, the performance of 5% and 10% tri-blend devices was restored as the dipoles were rotated to face the Al cathode. Although the internal dipole field then supports the built-in field, no enhancement to V_{oc} over the unpoled devices was noted. Previous reports [24] have shown that the maximum

attainable V_{oc} is limited by the difference in work-function of the electrodes and we suspect V_{oc} is being pinned at this value. Positive poling was also unable to improve FF or photocurrent, which is indicative that the devices' built-in field (i.e. without the ferroelectric additive) is already sufficient to collect all free charge carriers, owing to the moderately high mobility of P3HT. Since positively poled and unpoled devices show nearly the same improvements over the control device, it can be inferred that the dominant enhancement mechanism is present in both cases.This mechanism could be exciton (CTE and SE) dissociation as the local electric field around the dipoles is expected to enhance electron-hole separation even in an unpoled device with randomly-oriented dipoles. As previously indicated, field assisted exciton (both SE and CTE) dissociation process increases the photocurrent generation in 5% and 10% tri-blend devices (over the control OPV) by reducing the recombination. In the meantime, promoted CTE dissociation preserves the high quasi-Fermi energy of electrons, which then contributes to increasing the V_{oc} of 5% and 10% tri-blend devices (over the control OPV). Using these arguments, it is then appropriate to claim that PV enhancements observed in the 5 and 10% tri-blend devices (over control) are not related to an augmented charge transport processes but more likely a result of enriched SE and CTE dissociation. Moreover, the additional field induced by positive poling (supporting built-in field) might be especially important for improving the photogenerated-carrier transport and collection in blends of semiconducting polymers with poor carrier mobility [13,14,25]. We note that this effect of PV switching by poling the PVDF-TrFE dipoles was not demonstrated by the 20% PVDF-TrFE sample. We attribute this to aggregation of the nanodipoles; hence, the applied electric field during poling is

shielded within each cluster leaving a majority of dipoles un-poled and randomly oriented [20].

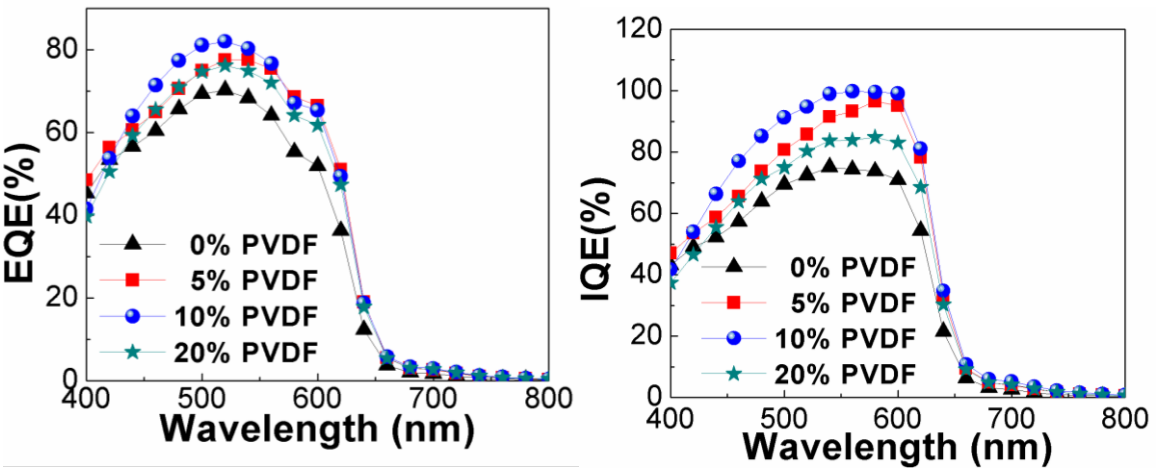

Figure 7.3: (a) External quantum efficiency (EQE) and (b) internal quantum efficiency (IQE) of P3HT:PCBM solar cells with various amounts of PVDF-TrFE additive.

In order to observe spectral enhancement as a result of enriched exciton scission, external quantum efficiency (EQE) of the devices was measured. Figure 7.3 shows EQE as a function of wavelength. These measurements show similar enhancement as observed in photocurrent measurements, with all three tri-blend devices (5, 10 and 20 wt% PVDF-TrFE) exhibiting EQE improvements over the entire spectra i.e. between the wavelengths of 400nm and 650nm. However, since the films exhibit significant variation in optical absorption, EQE cannot be considered representative for enhanced exciton dissociation process. Hence, internal quantum efficiency (IQE) was calculated (using the method detailed by Burkhard et.al [26]). The spectral shape of the IQE curve can provide information about the efficiency of harvesting excitons in the cell. We observed that the IQE spectrum is not flat because of differences in the efficiencies at which P3HT and PCBM excitons are harvested [Figure 7.3 (b)]. Lower IQE of high energy photons is a result of incomplete exciton harvesting from PCBM which is the dominant absorbing

species at lower wavelengths [27]. The 10 % tri-blend device exhibited an IQE approaching 100%, implying that almost all of the CTE excitons created are contributing to photocurrent, i.e. the internal field enhancement brought on by incorporation of dipoles into the active layer leads to a CTE dissociation process that is ~100% efficient. Moreover, this result provides evidence of complete harvesting of SEs formed in the P3HT domain. This indicates that SEs which are not able diffuse to the P3HT:PCBM interface, undergo dissociation by dipole-field to form free charge carriers. To further elucidate the effect of PVDF-TrFE addition on SE dynamics, we performed time-resolved photoluminescence (PL) on all four devices.

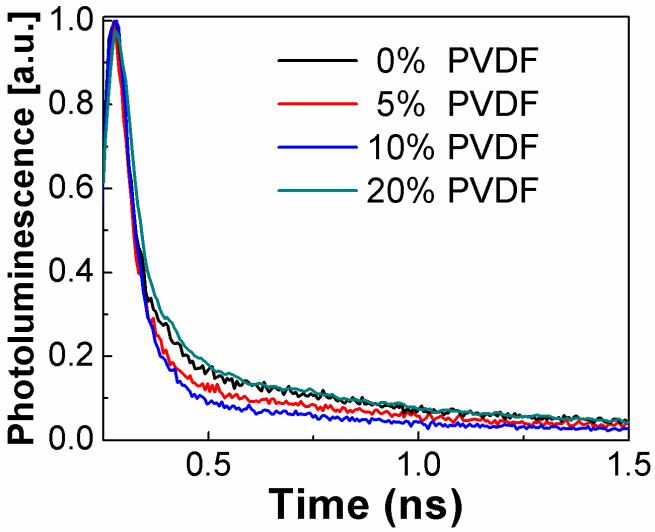

Figure 7.4: Normalized transient PL lifetimes for the PVDF-TrFE tri-blend OPVs

Transient PL was conducted by optically exciting the devices at 407 nm and measuring the exponential decay of PL (500-800nm) as the excitons relax to ground state. Here, radiative-recombination of SEs generated in the P3HT domain contributes to photoluminescence. The decay component is defined as a measure of SE lifetime and can be used to infer the degree of SE quenching. Time resolved Pl intensity is proportional to

SE concentration in P3HT, so a faster decay component indicates more efficient quenching of SEs [28]. SE quenching can be by field-assisted dissociation or by electron transfer to PCBM or to CT states. Additionally, due to the fact that the dynamics of the PL is also monitoring exciton diffusion, it can also provide information on the effect of the PVDF-TrFE addition on the morphology of the BHJ [29].

As shown in Figure 7.4, the PL lifetimes were found to be 100 ps, 95 ps, 73 ps and 122 ps for the 0, 5, 10 and 20 wt% tri-blends respectively. Clearly, the dipole rich 5 and 10 % PVDF-TrFE devices exhibit shortened Pl lifetimes, which is indicative of greater SE quenching. Interestingly, the 20% PVDF-TrFE device exhibited an increase in PL lifetime in spite of highest dipole concentration. As seen in the AFM phase image (refer to appendix), the blend domain size is significantly bigger in 20% device as compared to control sample. Thus, it can be deduced that adding 20 wt% PVDF affects the P3HT:PCBM BHJ morphology by coarsening the blend domains. Therefore in the 20% device, excitons have to diffuse through larger P3HT domains to reach aquenching interface, which increases the PL lifetime. The shortened PL lifetime in 5 and 10% tri-blend films can be a result of localized enhancements in electric field by PVDF-TrFE addition, contributing favorably towards direct SE dissociation. However, due to the observed domain-coarsening in the 20% tri-blend, Pl lifetime dependence on morphology in the 5 and 10% devices cannot be ruled out. Meaning, the higher PL quenching observed in the 5 and 10% devices could also imply a smaller size of polymer domains as compared to control. Although, the domain sizes in 5% and 10% tri-blend devices are not distinctly different from the control film (refer to appendix), morphology induced enhancements cannot be completely ruled out. Hence, there still exists a question associated with the PV enhancement observed in the

5 and 10% tri-blends. How is PVDF-TrFE addition augmenting the exciton dissociation: (i) by enhancing the internal electric field or (ii) by decreasing the domain size leading to a finer phase separation?

Although P3HT:PCBM based BHJ devices have produced the most efficient OPVs to date, recent reports have reappraised the importance of the bilayer structure [30]. Bilayer cells have the advantage of removing the complexity associated with the nanoscale morphology of BHJs, generating a simpler OPV cell in which the underlying operational physics can be better studied. Here, we have incorporated the PVDF-TrFE copolymer into P3HT:PCBM based bilayer devices to eliminate the possible effects of morphology changes upon PVDF addition and to elucidate the PVDF-field-induced effects. The bilayer structure can also allow us to further pinpoint where the FE dipoles (in the P3HT bulk or at the P3HT:PCBM interfaces) play the most beneficial role in the performance of BHJ devices. We have examined three types of bilayer P3HT:PCBM OPV devices (Figure 7.5): (i) control, (ii) mixture and (iii) interfacial. The control device was used as a reference and comprises a typical bilayer (P3HT:PCBM) structure with no ferroelectric dipoles added. The mixture device was also a typical bilayer structure but incorporated a 10 wt% additive of PVDF-TrFE into the P3HT layer. The interface device, technically a tri-layer device, included a PVDF-TrFE interlayer sandwiched between the P3HT and PCBM layers.

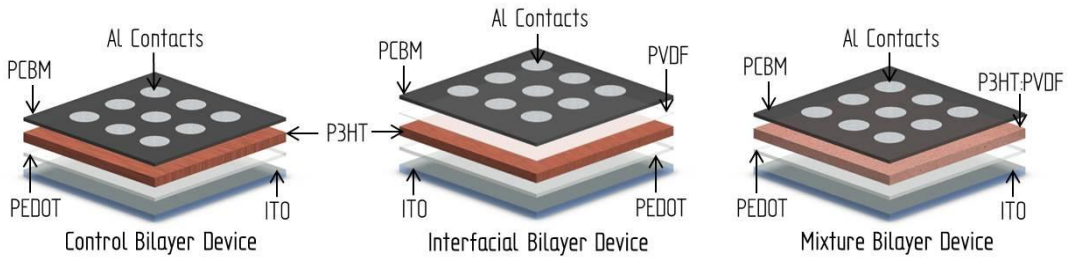

Figure 7.5: PVDF-TrFE bilayer structures

The bilayer PV performance characteristics are presented in Figure 7.6. The J-V curves show a distinct difference in the three OPV devices. The solar cells' short circuit current (J_{sc}), open circuit voltage (V_{oc}), fill factor (FF) and efficiency are summarized in Table 7.2.

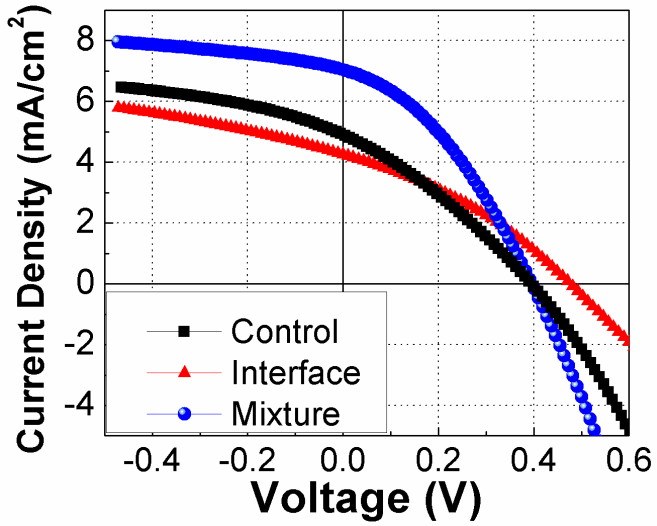

Figure 7.6: J-V characteristics of the bilayer devices

Table 7.2: Summary of bilayer solar cell performance parameters

	J_{sc}(mA/cm^2)	V_{oc}(V)	FF	Efficiency
Control bilayer	5	0.4	39	0.78%
Mixture bilayer	7.1	0.4	45	1.26%
Interface	4.2	0.5	35	0.73%

As shown, the mixture device exhibited the highest improvements to PV performance. The device displayed a 42% increase in photocurrent accompanied with a 15% increase in fill factor when compared to the control device. The observed enhancements can be field-induced since morphology is similar for the control and mixture bilayer devices. These increments support the results of the afore-detailed tri-blend devices

and give evidence that internal field enhancement (rather than morphology) is the improvement mechanism in the BHJ devices. The interface OPV also exhibited variations from the control device's performance. A 16% decrease in photocurrent coupled with a 25% increase in open circuit voltage was observed. The increase in V_{oc} can be imputed to the presence of high-field FE interfacial layer, which impedes the recombination of charge transfer (CT) excitons at the interface. Reduced interfacial recombination of CTE signifies lower reverse saturation current J_o, which, in accordance with Eq(3), increases V_{oc} [31]. A decrease in photocurrent relative to control device can be readily explained by the interfacial barrier (PVDF-TrFE layer) which impedes charge transfer between the donor and acceptor layers. Hence, placement of dipoles might be more beneficial in the P3HT domains rather than at the P3HT/PCBM interface.

$$V_{oc} = \frac{kT}{q} ln\left(\frac{J_{sc}}{J_0} + 1\right) \tag{3}$$

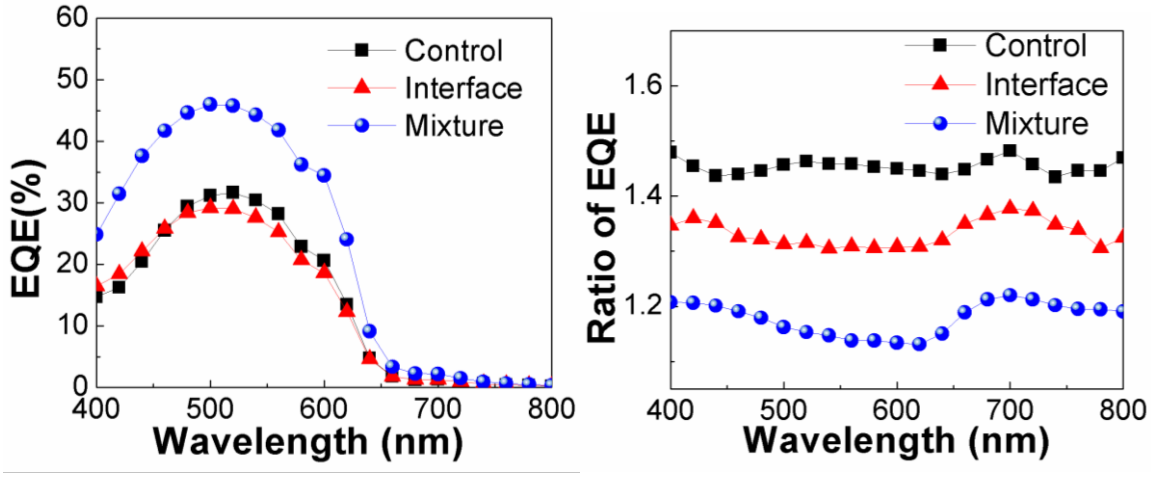

Figure 7.7: (a) EQE as a function of wavelength, and (b) Ratio of EQE at -1 V and 0 V bias for bilayer devices.

We next turned to EQE measurements of the bilayer PVDF-TrFE devices [Figure 7.7(a)] in order to seek evidence of dipole-field ameliorated exciton quenching and to further characterize the improvements noted in the BHJ devices. As shown, the mixture

device displayed an approximate 60-100% increase in EQE when compared to the control device between wavelengths 425 nm and 625 nm. The overall decrease in EQE of Interfacial device can be again attributed to the charge-transport-tunnel barrier between the donor and acceptor. Figure 7.7 (b) shows the EQE ratio of unbiased devices to biased devices (-1 V) for all three bilayer OPVs. For a biased device an increase in EQE is expected. Among other system improvements brought on by the external biasing (e.g. carrier collection), the applied field promotes enhanced exciton dissociation. Thus, by studying the EQE ratio of a biased to unbiased device one can infer the amount of dipole-field-induced dissociation enrichment already present in the unbiased device. As shown, the control device exhibited the highest improvement during a -1 V biasing (nearing 1.5) while the mixture device displayed the lowest (nearing 1.2). This implies the control device exhibits poor SE quenching (due to an insufficient internal field in the P3HT film), while the mixture device already contains some field-induced SE separation enhancements. As previously stated, SE dissociation is limited by a small diffusion length and an insufficient dissociation-driving field, leading to incomplete quenching. Thus, we expect a substantial increment in SE dissociation when high-field FE sites are introduced in P3HT layer of the mixture device. Since most of the singlet excitons are already dissociated in the mixture device, the applied bias (-1V) fails to significantly increase EQE. Therefore, the FE dipoles added to the P3HT layer of a bilayer device can alleviate the dependence of PV performance on exciton diffusion length.

To confirm the expected SE fission enhancement hinted at in the EQE results, transient PL of the three bilayer PVDF-TrFE OPVs was studied. As shown in Figure 7.8, the normalized PL lifetimes were found to be 144 ps, 122 ps, and 66 ps for the control,

mixture, and interface devices respectively. Clearly the dipole rich devices again exhibited shortened PL lifetimes. The mixture device presented a ~15% decrease in PL lifetime when

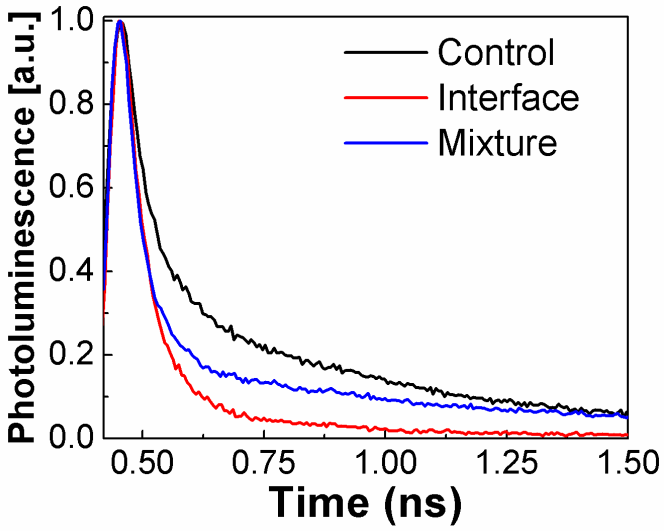

Figure 7.8: Transient PL lifetimes for the bilayer photovoltaic device

compared to the control device, showing less radiative recombination of SEs. Previous reports have shown evidence of field-assisted dissociation of the singlet state in organic films, where fluorescence quenching increased as a function of applied field strength [32]. Using Eq. (2) we estimate an increment as high as 600 V/μm (neglecting any agglomerate shielding effects) in the mixture device. Thus, field-effect enhancements of SE dissociation in this bilayer device are expected. Furthermore, because nanoscale morphology is irrelevant in the bilayer structure and is ruled out as a contributing factor to improvements observed in the bilayer devices, it can be asserted that the decreased PL of the 5 and 10% tri-blend devices is most likely also due to the FE-dipole field enhancements rather than a finer phase separation brought on by the ferroelectric additive. Interestingly, the interface device exhibited a much larger reduction in PL lifetime (~54% over the control device),

probably owing to the nature of its donor-acceptor interface modification (IM). Previous reports have claimed that dipole IM forms electronic states at the interface, which may mediate forward charge transfer and/or FRET, thereby increase PL quenching [33]. Further, similar reports show that dipole interfacial layers tend to shift the local vacuum level and change the band offset at the interface. These interfacial shifts can lead to additional band bending in P3HT layer and generation of a built-in field; thereby decreasing PL lifetime [33-35].

7.5 Conclusions

In conclusion, for the first time it is shown that incorporation of the ferroelectric copolymer PVDF-TrFE into the active blend of P3HT:PCBM-based OPVs can result in a significant improvement in photovoltaic performance. In this study we have embedded FE dipoles into modern bulk heterojuntion devices to achieve an efficiency enhancement of nearly 50%. Using data from absorption and electrical poling experiments, augmented optical effects as well as improved charge transport were ruled out as improvement mechanisms. We found, upon the addition of PVDF-TrFE, internal quantum efficiency approached 100% for some wavelengths. This result is indicative of complete exciton harvesting at these photon energies and implies that nearly every singlet exciton as well as nearly every charge transfer exciton are able to break their Columbic bond and separate. To differentiate between a dipole-induced increment to the internal field and a change in the nanoscale morphology as the dominate enhancement mechanism, bilayer devices, integrated with the ferroelectric copolymer, were subsequently studied. J-V characterization

revealed an efficiency enhancement of nearly 62% for those bilayer OPVs containing PVDF-TrFE in the P3HT layer. We were able to directly link this increment with the much improved internal field made possible by the dipole additive. Thereby ruling out changed morphology as an improvement mechanism in the BHJ devices and showing that bilayer devices incorporating PVDF-TrFE can be alleviated of performance dependence on SE diffusion length.

7.5 Acknowledgements

We thank Iowa Power Fund from the state of Iowa's Office of Energy Independence. We also thank Dr. Sayantan Bose and Dr. Jacob Petrich for photoluminescence measurements.

7.6 Appendix

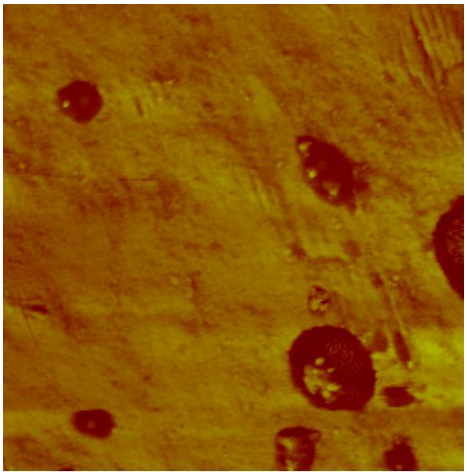

Figure 7.9: AFM phase image (scan size = 2 μm) showing agglomerates of PVDF-TrFE in 20% tri-blend film. Height scale is 40^{o}. The PVDF-TrFE agglomerate formation in 20% tri-blend film is confirmed by the presence of darker phase in the AFM phase image. Agglomerate size varies from 100-200nm.

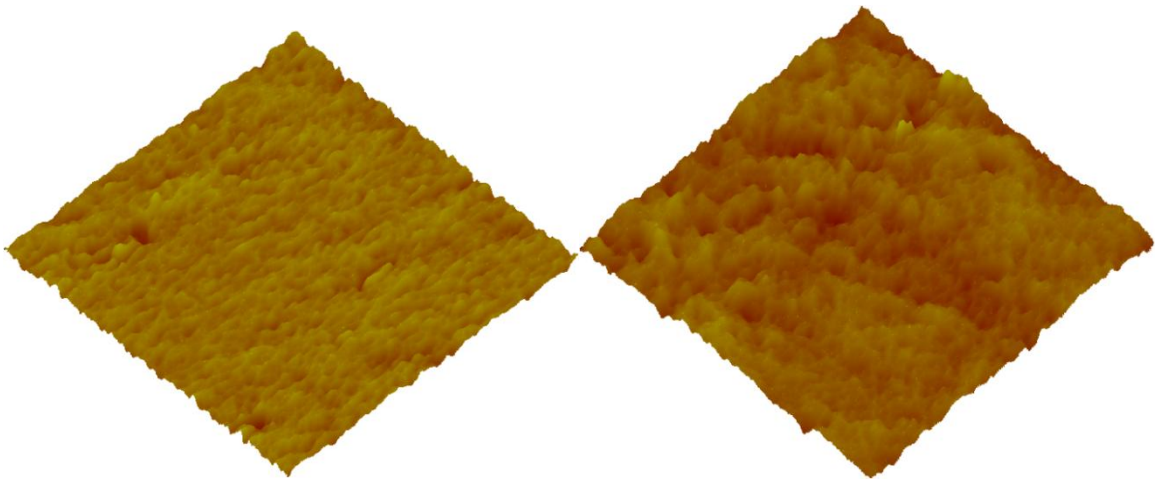

(a) (b)

Figure 7.10: AFM phase image of (a) control (b) 20% tri-blend films. Scan size is 1µm × 1µm. Height scale is 20 degrees. 20% tri-blend film shows coarser blend morphology as compared to the control film. Due to the coarser morphology of 20% tri-blend device, excitons have to diffuse through larger P3HT domains to reach the quenching interface, which increases the PL lifetime.

7.7 References

[1] Kirchartz, T., Taretto, K. & Rau, U. Efficiency Limits of Organic Bulk Heterojunction Solar Cells. *Journal of Physical Chemistry C***113**, 17958-17966 (2009).

[2] Chen, H. Y. *et al.* Polymer solar cells with enhanced open-circuit voltage and efficiency. *Nature Photonics***3**, 649-653 (2009).

[3] Liang, Y. Y. *et al.* For the Bright Future-Bulk Heterojunction Polymer Solar Cells with Power Conversion Efficiency of 7.4%. *Advanced Materials***22**, E135 (2010).

[4] Park, S. H. *et al.* Bulk heterojunction solar cells with internal quantum efficiency approaching 100%. *Nature Photonics***3**, 297 (2009).

[5] Li, G. *et al.* High-efficiency solution processable polymer photovoltaic cells by self-organization of polymer blends. *Nature Materials***4**, 864-868 (2005).

[6] Li, G. *et al.* "Solvent annealing" effect in polymer solar cells based on poly(3-hexylthiophene) and methanofullerenes. *Advanced Functional Materials***17**, 1636-1644 (2007).

[7] Ma, W. L., Yang, C. Y., Gong, X., Lee, K. & Heeger, A. J. Thermally stable, efficient polymer solar cells with nanoscale control of the interpenetrating network morphology. *Advanced Functional Materials***15**, 1617-1622 (2005).

[8] Peet, J. *et al.* Efficiency enhancement in low-bandgap polymer solar cells by processing with alkane dithiols. *Nature Materials***6**, 497-500 (2007).

[9] Yao, Y., Hou, J. H., Xu, Z., Li, G. & Yang, Y. Effect of solvent mixture on the nanoscale phase separation in polymer solar cells. *Advanced Functional Materials***18**, 1783-1789 (2008).

[10] Miller, S. *et al.* Investigation of nanoscale morphological changes in organic photovoltaics during solvent vapor annealing. *Journal of Materials Chemistry***18**, 306-312 (2008).

[11] Zhu, X. Y., Yang, Q. & Muntwiler, M. Charge-Transfer Excitons at Organic Semiconductor Surfaces and Interfaces. *Accounts of Chemical Research***42**, 1779-1787 (2009).

[12] Zhou, Z., Shinar, R., Allison, A. J. & Shinar, J. Enhanced photoluminescence of oxygen sensing films through doping with high dielectric constant particles. *Advanced Functional Materials***17**, 3530-3537 (2007).

[13] Melzer, C., Koop, E. J., Mihailetchi, V. D. & Blom, P. W. M. Hole transport in poly(phenylene vinylene)/methanofullerene bulk-heterojunction solar cells. *Advanced Functional Materials***14**, 865-870 (2004).

[14] Chen, H. Y. *et al.* Silicon Atom Substitution Enhances Interchain Packing in a Thiophene-Based Polymer System. *Advanced Materials***22**, 371 (2010).

[15] Wojcik, M. & Tachiya, M. Accuracies of the empirical theories of the escape probability based on Eigen model and Braun model compared with the exact extension of Onsager theory. *Journal of Chemical Physics***130**, 3082005 (2009).

[16] Deibel, C. *et al.* Energetics of excited states in the conjugated polymer poly(3-hexylthiophene). *Physical Review B***81**, 085202 (2010).

[17] Mihailetchi, V. D., Koster, L. J. A., Hummelen, J. C. & Blom, P. W. M. Photocurrent generation in polymer-fullerene bulk heterojunctions. *Physical Review Letters***93**, 216601 (2004).

[18] Peumans, P., Yakimov, A. & Forrest, S. R. Small molecular weight organic thin-film photodetectors and solar cells. *Journal of Applied Physics***93**, 3693-3723 (2003).

[19] Cheng, Z. Y. & Zhang, Q. M. Field-activated electroactive polymers. *Mrs Bulletin***33**, 183-187 (2008).

[20] Shvydka, D. & Karpov, V. G. Nanodipole photovoltaics. *Applied Physics Letters***92**, 2835972 (2008).

[21] Wegener, M. Polarization-electric field hysteresis of ferroelectric PVDF films: comparison of different measurement regimes. *Rev Sci Instrum***79**, 106103, (2008).

[22] Naber, R., De Boer, B., Blom, P. & De Leeuw, D. Low-voltage polymer field-effect transistors for nonvolatile memories. *Applied Physics Letters***87**, 203509 (2005).

[23] Maurano, A. *et al.* Recombination Dynamics as a Key Determinant of Open Circuit Voltage in Organic Bulk Heterojunction Solar Cells: A Comparison of Four Different Donor Polymers. *Advanced Materials***22**, 4987 (2010).

[24] Uhrich, C. *et al.* Origin of open circuit voltage in planar and bulk heterojunction organic thin-film photovoltaics depending on doped transport layers. *Journal of Applied Physics***104**, 2973199 (2008).

[25] Pivrikas, A. *et al.* Bimolecular recombination coefficient as a sensitive testing parameter for low-mobility solar-cell materials. *Physical Review Letters***94**, 176806 (2005).

[26] Burkhard, G. F., Hoke, E. T. & McGehee, M. D. Accounting for Interference, Scattering, and Electrode Absorption to Make Accurate Internal Quantum Efficiency Measurements in Organic and Other Thin Solar Cells. *Advanced Materials***22**, 3293 (2010).

[27] Burkhard, G. F., Hoke, E. T., Scully, S. R. & McGehee, M. D. Incomplete Exciton Harvesting from Fullerenes in Bulk Heterojunction Solar Cells. *Nano Letters***9**, 4037-4041 (2009).

[28] Ruseckas, A., Shaw, P. E. & Samuel, I. D. W. Probing the nanoscale phase separation in binary photovoltaic blends of poly(3-hexylthiophene) and methanofullerene by energy transfer. *Dalton Transactions*, 10040-10043(2009).

[29] Jarzab, D. *et al.* Charge Transfer Dynamics in Polymer-Fullerene Blends for Efficient Solar Cells. *Journal of Physical Chemistry B***113**, 16513-16517 (2009).

[30] Ayzner, A. L., Tassone, C. J., Tolbert, S. H. & Schwartz, B. J. Reappraising the Need for Bulk Heterojunctions in Polymer-Fullerene Photovoltaics: The Role of Carrier Transport in All-Solution-Processed P3HT/PCBM Bilayer Solar Cells. *Journal of Physical Chemistry C***113**, 20050-20060 (2009).

[31] Vandewal, K., Tvingstedt, K., Gadisa, A., Inganas, O. & Manca, J. V. On the origin of the open-circuit voltage of polymer-fullerene solar cells. *Nature Materials***8**, 904-909 (2009).

[32] Khan, M. I., Bazan, G. C. & Popovic, Z. D. Evidence for electric field-assisted dissociation of the excited singlet state into charge carriers in MEH-PPV. *Chemical physics letters***298**, 309-314 (1998).

[33] Goh, C., Scully, S. R. & McGehee, M. D. Effects of molecular interface modification in hybrid organic-inorganic photovoltaic cells. *Journal of applied physics***101**, 114503 (2007).

[34] Kim, D. Y. *et al.* The effect of molybdenum oxide interlayer on organic photovoltaic cells. *Applied Physics Letters***95**, 093304-093304-093303 (2009).

[35] Liu, Y. *et al.* Dependence of band offset and open-circuit voltage on the interfacial interaction between TiO2 and carboxylated polythiophenes. *The Journal of Physical Chemistry B***110**, 3257-3261 (2006).

CHAPTER 8. Conclusions

In an effort to address the problem of poor absorption in the active layer of organic photovoltaic cells (OPVs), microscale textured OPVs with promising light trapping characteristics were studied. Using the finite element method, the optical behavior of microscale textured OPVs in comparison with the conventional planar geometry was modeled. A maximum of 40% theoretical increase in photonic absorption is observed in active layer (150 nm) for grating-type bottom electrode with 2 μm pitch and 1.5 μm height texture. Results show that if an OPV active layer is conformally deposited on a textured electrode, it is possible to achieve optimal photonic absorption in thinner active layers, which will lead to improved charge transport and higher efficiencies in OPVs. For verifying the afore-mentioned theoretical results and improving the efficiency of OPVs by light trapping, OPVs were fabricated on grating-type textured substrates possessing several submicron and micron scale topographical dimensions. For microscale patterns, where both pitch and height of the grating structure are greater than 1 μm, the spin-casted active-layer was highly non-conformal. This result indicated that it is the microscale height of the grating that led to the non-conformal nature of coating. Thus, we resorted to gratings with sub-micron heights. It is discovered that if the height of the underlying topographical features is reduced to sub-micron regime (e.g. 300 nm) and the pitch is increased to more than a micron (e.g. 2 μm), the textured surface becomes amenable to coating a conformal PV active-layer. Realizing polymer PV cells on such topographies provides an efficient way to achieve light-trapping without compromising with electrical characteristics. Such OPV cells having conformal active layer, showed 20% improvement in power conversion

efficiency relative to the flat control, owing to broadband light-trapping, especially at the band-edge where 100% average absorption increase was observed. The most significant absorption improvement using the grating geometry is obtained at the band-edge of P3HT (~600 nm). Specifically, a 2.6-fold absorption enhancement is achieved at λ= 640 nm for grating cell, relative to the planar one. This conduces to an average 100% increase in absorption near the band edge ($600 \leq \lambda \leq 700$ nm). The EQE followed the same trend as the absorption, confirming that the improvement in device performance is indeed due to light-trapping, rather than increased device area or any electrical effect. The grating based devices also exhibited superior performance over the flat devices at higher incident angles of light.

In order to understand the effect of processing conditions such as spin coating speed and drying rate on the carrier recombination mechanism; poly(3-hexylthiophene) (P3HT):fullerene-derivative (PCBM) solar cells were fabricated with different growth rates (drying time of films). It is shown that the slow growth assists the formation of self-organized ordered structure in the P3HT/PCBM blend system diminishing morphological defects in P3HT chains. Fast growth, however results in an order of magnitude higher sub-band gap trap density owing to the structural defects (twists and bends) in P3HT chains. By coupling our experimental results with simulations, it is demonstrated that at one sun condition, slow grown film has bimolecular recombination as the major loss mechanism which exceeds the interfacial recombination loss by an order of magnitude. However, for the case of fast grown film with high trap density, the trap-assisted interfacial recombination dominates over the intrinsic bimolecular recombination by a factor of 10. The trap-assisted recombination dominates the super-linear light-intensity dependence of

the open circuit voltage observed for these OPVs. The enhanced recombination losses, owing to the presence of excessive traps, also lower the fill factor and short circuit current. Therefore, it becomes imperative to design materials without traps to defect-engineer the OPVs for achieving higher performance.

For the first time it is shown that incorporation of the ferroelectric (FE) copolymer PVDF-TrFE into the active blend of P3HT:PCBM-based OPVs can result in a significant improvement in photovoltaic performance. FE dipoles were embedded into modern bulk heterojuntion (BHJ) devices to achieve an efficiency enhancement of nearly 50%. Using data from absorption and electrical poling experiments, augmented optical effects as well as improved charge transport were ruled out respectively, as improvement mechanisms. It is found, upon the addition of PVDF-TrFE, internal quantum efficiency approached 100% for some wavelengths. This result is indicative of complete exciton harvesting at these photon energies and implies that nearly every singlet exciton as well as nearly every charge transfer exciton are able to break their Columbic bond and separate. To differentiate between a dipole-induced increment to the internal field and a change in the nanoscale morphology as the dominant enhancement mechanism, bilayer devices, integrated with the ferroelectric copolymer, were subsequently studied. J-V characterization revealed an efficiency enhancement of nearly 62% for those bilayer OPVs containing PVDF-TrFE in the P3HT layer. We were able to directly link this increment with the much improved singlet exciton dissociation due to high internal field made possible by the dipole additive. Thereby ruling out changed morphology as an improvement mechanism in the BHJ devices and showing that bilayer devices incorporating PVDF-TrFE can be alleviated of performance dependence on SE diffusion length.

CHAPTER 9. Future Work

For achieving conformal coating of active layer in grating based OPVs, another anticipated problem can be related to one-dimensional (1D) nature of grating structures. This 1D nature does not provide radial symmetry in case of spin-coating. This may lead to irregularities in the film-coating at one point versus another point centimeter distance away, hence investigations on 2D topographies with radial geometry, might prove beneficial for grating based organic solar cells. The 2D topography might lead to additional optoelectronic enhancement due to higher surface area and better light trapping.

The growth rate of active layer has been found to be a critical control parameter for defect density and recombination rate. It remains to be seen whether solvent-annealing has an advantage over thermal annealing in terms of reducing traps and trap-assisted recombination. Recently, several solvent additives (e.g. Alkanethiol) have been reported to improve the performance of OPVs due to longer carrier lifetime with ordered structure in morphology. The improvement has been attributed to lower solubility of fullerene in alkanethiol, which leads to better phase separation during film growth. However, the effect of solvent additives on defect density in polymer and recombination rate remains unclear. Thus, we have instigated the study of solvent addition in polymer:fullerene system, to understand the effect of solubility difference on morphology evolution and trap density.

It is shown that incorporation of the ferroelectric copolymer PVDF-TrFE into the active blend of P3HT:PCBM-based OPVs can result in a significant improvement in photovoltaic performance. The effect of ferroelectric addition in organic light emitting diodes (OLEDs) remains yet to be investigated. Preliminary results show that upon

ferroelectric addition, electroluminescence from the OLEDs decreased significantly, which can be attributed to enhanced singlet exciton dissociation. Moreover, an important study could be nanoscopic morphological characterization of photoactive layer (with PVDF-TrFE addition) to reveal the distribution of dipoles. This could be pursued by utilizing techniques like transmission electron microscopy, piezoelectric force microscopy and X-ray photoelectron spectroscopy. Simulations can also be performed to theoretically predict the increase in probability of exciton dissociation (using Braun's model) by dipole-induced electrostatic field. This effect can be evaluated as a function of volume fraction of PVDF-TrFE in the photoactive blend.